Measurements and Simulations of Impedance Reduction Techniques in Particle Accelerators

A thesis submitted to the University of Manchester for the degree of

Doctor of Philosophy

in the Faculty of Engineering and Physical Sciences

2012

Hugo Alistair Day

School of Physics and Astronomy

Contents

Total word count: 27794

List of Tables

List of Figures

14

15

16

19

21

Abstract

The phenomenon of wakefields and the corresponding frequency-domain property, beam coupling impedance have long been studied in particle accelerators. They are important as a source of beam instabilities due beam-equipment interactions and placing restrictions on the operating parameters of particle accelerators. As accelerators have pushed towards smaller beam emittances and higher beam currents the importance of controlling the beam impedance has become more important. With the latest high power accelerators, even beam-induced heating due to the beam power loss has become a serious limitation on beam operation.

In this thesis a short review of the existing impedance reduction techniques in use in many particle accelerators is given. The limitations and restrictions of these techniques is also considered, focusing heavily on the usage of damping materials to reduce the Q of cavity resonances. In addition to covering a number of methods of measuring (using benchtop and beam-based measurements) or simulating the beam impedance of devices. In particular the use of the coaxial wire technique - a bench top measurement method for measuring the beam impedance of a device - to measure the longitudinal and transverse (dipolar, quadrupolar and constant) impedancess of symmetric and asymmetric structures. These techniques are subsequently applied to two significant sources of beam impedance within the LHC - the injection kicker magnets (LHC-MKIs) and elements of the collimation upgrades for the LHC. A comparison between simulations and measurements of the impedance of the MKI is presented in addition to an evaluation of alternative beam screen designs in regards to the possible beam-induced heating of the structure. Two facets of the LHC collimation upgrade are investigated - the choice of the jaw material of the phase

2 secondary collimators, expected to be a significant contributor to the LHC transverse impedance budget, and the TCTP collimator for which a full structure simulation is carried out to determine the effectiveness of the impedance reduction system in place.

Declaration

No portion of the work referred to in this thesis has been submitted in support of an application for another degree or qualification of this or any other university or other institution of learning.

Hugo Alistair Day

School of Physics and Astronomy

University of Manchester

Oxford Road

Manchester

M13 9PL

November 2006

Copyright

The Author

The author grew up in the south of the UK, leaving King Edward VI Grammar School in 2005 to read physics at the University of Southampton. In 2008 he was lucky enough to be selected for a summer studentship at CERN studying particle behaviour in the spectrometer of the 3MeV test bed for the Linac4 H- source. After graduating from Southampton in 2009 with an MPhys in Physics he went north to study for a PhD in the School of Physics and Astronomy at the University of Manchester. He was able to acquire a Doctoral Studentship from the CERN Doctoral Student Programme and subsequently spent three exceptional years at CERN, Switzerland.

Acknowledgements

Chapter 1

Introduction

1.1 The CERN Accelerator Complex

CERN (Organisation europeene pour la recherche nucleaire) is a particle physics laboratory near Geneva, Switzerland crossing the Franco-Swiss border between the Swiss commune of Meyrin and French town of Saint-Genis Pouilly. It was founded in 1952 with the creation of the Coseil Européen pour la Recherche Nucléaire, which became the Organisation in 1954. It houses an accelerator complex (shown in Fig. 1.1) ranging in energies from hundreds of MeV (extraction energy for Linac2) to energies of 7TeV (for the LHC), delivering proton bunches to various experiments (fixed target, colliding and beam) at all energy levels. These experiments have a variety of aims, varying from neutrino physics[cite CNGS], neutron physics[cite nTOF] antimatter experiments [cite ALPHA, ASACUSA, ATRAP] as well as radio isotope [cite ISOLDE] and hadron therapy [cite ACE] research. The Large Hadron Collider (LHC), the largest accelerator at CERN, is at the forefront of high-energy physics designed to push the energy frontier of knowledge of particle physics.

Figure 1.1: The CERN accelerator complex, showing both the proton and heavy ion (lead) accelerator chains from LINACs 2 and 3 up to the LHC. Different experimental uses are highlighted in the diagram.

1.2   The LHC

The LHC is a proton synchrotron built to collide counter rotating beams of protons at an centre of mass energy of 14TeV. It uses 1,232 superconducting dipole magnets to bend the proton beams on a circular orbit around the beam line, in addition to using 392 quadrupole magnets for focusing in the transverse plane to maintain the bunch cross section and carry out final focusing for the 4 detector experiments in the LHC. Four detector experments are operated at the LHC; two general purpose detectors ATLAS and CMS, used for searches of new physics beyond the current energy frontier [cite design reports]; LHCb, a forward detector specialised in the analysis of B-physics [cite report] and ALICE, a detector specialised in heavy ion collisions with the intent of observing the physics of quark-gluon plasma [cite report. Technical Proposals]. Three further experiments are in place in the LHC, LHCf (an experiment related to the effects of high-energy cosmic rays), TOTEM (measuring the total cross-section of the proton via elastic scattering processes at the collision points) and MoEDAL (an experiment searching for magnetic monopoles and stable massive particles) complete the experiments provided with data by collisions using LHC delivered protons.

1.3   Operational Figure of Merit - Luminosity

One of the key figures of merit for the operation of the LHC (along with the centre of mass energy) is the luminosity at the colliding interaction regions (IRs). This is a figure which denotes the total rate of production of new (in the sense of produced during interactions during collisions between protons) particles in collider experiments. It can be thought of as the factor proportionality between the cross section of a reaction scheme and the number of interactions per second

$$\frac{dR}{dt} = \mathcal{L} \times \sigma_p \tag{1.1}$$

where $\frac{dR}{dt}$ is the interaction rate, $\mathcal{L}$ is the luminosity and σ_p is the production cross

section for a given particle production scheme. For two colliding bunches, each with a gaussian transverse cross-section the luminosity can be given in a simplified form by

$$\mathcal{L} = \frac{N_1 N_2 f n_b}{4\pi \sigma_x \sigma_y} \tag{1.2}$$

where $N_{1/2}$ is the bunch population of beams 1 and 2 respectively, f is the revolution frequency, n_b is the number of colliding bunches in the machine and $\sigma_{x/y}$ are the gaussian bunch sigma in the horizontal and vertical planes respectively. Both the the bunch populations $N_{1/2}$, the revoution frequency f and the number of bunches n_b also contribute towards the DC beam current in the machine $I_b = N_1 f e n_b$ where e is the elementary electron charge. As will be seen in Sec. 2.3.1 the expected power loss due to beam-equipment interactions by the process of power loss is proportional to the I_b^2, thus it can be seen that increasing the luminosity will increase the power loss experienced by in equipment in a linear to quadratic fashion.

1.3.1 Integrated Luminosity

Following from the luminosity, the determinant of the quantity of experimental data is the integrated luminosity of an experiment $\mathcal{L}_{int}$ given by

$$\mathcal{L}_{int} = \int_0^T \mathcal{L}(t)\, dt \tag{1.3}$$

where T is the integrated collision time and $\mathcal{L}(t)$ is the time varying luminosity (typically decaying exponentially over the lifetime of any given fill of the collider[cite]), varying due to changing beam conditions and bunch populaton depletion due to collisions and particle losses. The integrated luminosity is significant as the number of a given particle production schema observed by the experiments n_{event} is given by

$$n_{event} = \mathcal{L}_{int} \times \sigma_p. \tag{1.4}$$

It can thus be seen that in addition to increasing the luminosity, maximising the available time for collisions is important to maximising data collection. This requires a high

Figure 1.2: The representation of the coordinate system of a circular accelerator, and additionally the co-moving reference frame of a circulating particle.

level of availability of the machine, minimising failures of key systems and the down time experienced by the machine. In particular, unavoidable waiting periods between fills are to be avoided at all costs. As is seen in Chapter 8, long cool down times (on the order of hours, similar in magnitude to the length of the average LHC fill) for equipment that requires a specific temperature range to operate correctly are thus unacceptable during ideal operation and should be reduced to a minimum. These and other sources of reduction of the running time and luminosity (due to both beam coupling impedance and other sources of instabilities and interlock trips due to hardware mishaps) must thus be carefully studied and controlled by the technical and operations teams.

1.4   Beam Dynamics

To introduce the terms, dynamics and coordinate systems used in later chapters we shall briefly introduce the basic transverse and longitudinal dynamics present in particle accelerators. First we introduce the coordinate system typically used in the consideration of circular particle accelerators. Typically an ideal orbit is defined for an on momentum particle, denoted by (ρ, θ, z). In addition a reference frame placed upon the orbit of an ideal on-momentum is defined, given by (x, y, z) shown in Fig. 1.4.

The use of charged particles within an accelerator is controlled by the use of both magnetic and electrical elements in the machine, leading to the particles being acted upon by the Lorentz force

$$\mathbf{F} = q\left(\mathbf{E} + \mathbf{v} \times \mathbf{B}\right) \tag{1.5}$$

where q is the charge of the particle, $\mathbf{E}$ is the electric field, $\mathbf{B}$ is the magnetic field and $\mathbf{v}$ is the particles velocity. In high energy particle accelerators the magnetic and electric fields are typically seperated in location, with the magnetic fields only having a transverse component, being of the form

$$\mathbf{B} = \hat{\mathbf{x}}B_x + \hat{\mathbf{y}}B_y \tag{1.6}$$

where $B_{x/y}$ is the magnetic field component in the x- and y-axis respectively. Due to the cross product between the velocity ($\mathbf{v} = \hat{\mathbf{z}}v$), it can be seen that there is no component of the force from the magnetic field in the z-direction. In addition the electric field usually only has a longitudinal component such that $\mathbf{E} = \hat{\mathbf{z}}E_z$. This results in the seperation of transverse and longitudinal motion such that

$$F_{\parallel} = qE \tag{1.7}$$

$$\mathbf{F}_{\perp} = q\left(vB_y\hat{\mathbf{x}} - vB_x\hat{\mathbf{y}}\right). \tag{1.8}$$

Subsequently the transverse and longitudinal motion may both be treated independently of one another.

1.4.1 Linear Transverse Dynamics

If we consider a charged particle of mass m and charge e moving with velocity v along the ideal orbit under the effect of the magnetic field B we can see that the lorentz force ($F_L = qvB$) and the centrifugal force ($F_{cen} = \frac{\gamma m v^2}{\rho}$) are equivalent, leading to the relation

$$\frac{p}{e} = B\rho \tag{1.9}$$

where p is the particles momentum. $B\rho$ is referred to as the beam rigidity, denoting the constant term necessary to keep a particle on the ideal orbit.

If we consider the motion of a particle transversally displaced from the ideal orbit particle with a position (x, y) we must consider the variation of the magnetic field in the transverse directions. If we consider first just the horizontal motion, we can carry out a taylor expansion of the field which gives us

$$B_y\left(x\right) = B_{y0} + \frac{dB_y}{dx}x + \frac{1}{2!}\frac{d^2B_y}{dx^2}x^2 + \frac{1}{3!}\frac{d^3B_y}{dx^3}x^3 + ... \tag{1.10}$$

which is then normalised by p/e

$$\frac{B_y(x)}{p/e} = \frac{B_{y0}}{B_{y0}\rho} + \frac{1}{p/e}\frac{dB_y}{dx}x + \frac{1}{p/e}\frac{1}{2!}\frac{d^2B_y}{dx^2}x^2 + \frac{1}{p/e}\frac{1}{3!}\frac{d^3B_y}{dx^3}x^3 + ... \qquad (1.11)$$

For the time being we shall consider only small displacements in x and y, thus shall consider only the linear terms, giving

$$\frac{B_y(x)}{p/e} = \frac{1}{\rho} + \frac{1}{p/e}\frac{dB_y}{dx}x \qquad (1.12)$$

$$\frac{B_y(x)}{p/e} = \frac{1}{\rho} + kx \qquad (1.13)$$

where $k = \frac{g}{p/e}$, $g = \frac{2\mu_0 nI}{r^2}$ is the gradient of a quadrupole magnet (a magnet which has a magnetic field strength linearly proportional to displacement), with n being the number of turns on the solenoid, I the current and r the solenoid aperture. This indicates that seperation of the function of magnets is valid method of controlling the particles, using dipole and quadrupole fields. Next, to derive the equations of motion we shall consider the equation for radial acceleration a_r for a particle undergoing rotational acceleration in the defined coordinate system

$$a_r = \frac{d^2\rho}{dt^2} - \rho\left(\frac{d\theta}{dt}\right)^2. \qquad (1.14)$$

For the particle on the ideal orbit $\rho = constant$, so $\frac{d\rho}{dt} = 0$, leading to the accelerative force being derived to be

$$F_x = m\rho\left(\frac{d\theta}{dt}\right)^2 = m\rho\omega^2 = \frac{mv^2}{\rho} \qquad (1.15)$$

For a general particle, $\rho \to \rho + x$, leading to

$$F_x = m\frac{d^2}{dt^2}(x+\rho) - \frac{mv^2}{x+\rho} = eB_yv. \qquad (1.16)$$

As $\rho = constant$, $\frac{d^2}{dt^2}(x+\rho)$ becomes $\frac{d^2x}{dt^2}$. In addition we are dealing with displacements of $x \ll \rho$, so we may approximate $\frac{1}{x+\rho} \approx \frac{1}{\rho}(1 - \frac{x}{\rho})$ from the taylor expansion and taking linear terms in x. Thus we acquire the equation

34

$$m\frac{d^2x}{dt^2} - \frac{mv^2}{\rho}\left(1 - \frac{x}{\rho}\right) = eB_y v. \tag{1.17}$$

Subsequently we subsitute the magnetic field $B_y = B_{y0} + \frac{dB_y}{dx}x$ and arrive at

$$m\frac{d^2x}{dt^2} - \frac{mv^2}{\rho}\left(1 - \frac{x}{\rho}\right) = ev\left[B_{y0} + \frac{dB_y}{dx}x\right]. \tag{1.18}$$

By dividing throught by the mass m

$$\frac{d^2x}{dt^2} - \frac{v^2}{\rho}\left(1 - \frac{x}{\rho}\right) = \frac{evB_{y0}}{m} + \frac{ev}{m}\frac{dB_y}{dx}x. \tag{1.19}$$

Next we transform the coordinate from $t \to z$, such that

$$\frac{d^2x}{dt^2} = \frac{d}{dt}\left(\frac{dx}{dz}\frac{dz}{dt}\right) = \frac{d}{dz}\left(\frac{dx}{dz}\frac{dz}{dt}\right)\frac{dz}{dt} = \frac{d^2x}{dz^2}\left(\frac{dz}{dt}\right)^2 + \frac{dx}{dz}\frac{d}{dz}\left(\frac{dz}{dt}\right)\frac{dz}{dt}. \tag{1.20}$$

It can be seen that $\frac{dz}{dt} = v$, which is kept constant in this treatment. Therefor

$$\frac{d^2x}{dt^2} = \frac{d^2x}{dz^2}v^2. \tag{1.21}$$

Thus we arrive at the equation

$$\frac{d^2x}{dz^2}v^2 - \frac{v^2}{\rho}\left(1 - \frac{x}{\rho}\right) = \frac{evB_{y0}}{m} + \frac{ev}{m}\frac{dB_y}{dx}x. \tag{1.22}$$

We then subsequently normalise by momentum and rearrange slightly to acquire

$$\frac{d^2x}{dz^2} - \frac{1}{\rho} + \frac{x}{\rho^2} = \frac{B_{y0}}{p/e} + \frac{1}{p/e}\frac{dB_y}{dx}x. \tag{1.23}$$

We then remember the definition of the beam rigidity (see Eqn. 1.9) and the definition of the quadrupolar field strength arriving at

$$\frac{d^2x}{dz^2} - \frac{1}{\rho} + \frac{x}{\rho^2} = -\frac{1}{\rho} + kx \tag{1.24}$$

$$\frac{d^2x}{dz^2} + \frac{x}{\rho^2} = kx$$

$$\frac{d^2x}{dz^2} + x\left(\frac{1}{\rho^2} - k\right) = 0.$$

For the vertical plane the equation is the same, except that the focusing term is negative and there is no ρ term, giving

$$\frac{d^2y}{dz^2} + ky = 0. \tag{1.25}$$

It is interesting to note that there is a focusing term due to the dipolar magnet term. Historically this is the weak focusing effect, as opposed to the strong focusing regime of using quadrupole magnets. It can be seen this these equations are simply the equations of motion of a harmonic oscillator with spring constants $K_{x/y}$ given by

$$K_x = \frac{1}{\rho^2} - k$$

$$K_y = k$$

leading to a general solution

$$x/y\,(s) = a_1 cos\left(\sqrt{K_{x/y}}s\right) + a_2 sin\left(\sqrt{K_{x/y}}s\right). \tag{1.26}$$

For a modern particle accelerator using focusing and defocusing magnets arranged in a periodic lattice (i.e. so that $k(s)$ becomes a periodic function such that $k(s + L) = k(s)$ where L is the length of the period of the lattice), and applying initial conditions $x(0) = x_0, x'(0) = x_0'$ it is possible to finally arrive at the solution for the motion of a particle through a periodic lattice

$$x\,(s) = \sqrt{\epsilon}\sqrt{\beta\,(s)}cos\left(\psi\,(s) + \phi\right) \tag{1.27}$$

where ϵ and ϕ are integration constants determined by the initial conditions, $\beta(s)$ is a periodic function determined by the focusing properties of the lattice. $\psi(s)$ is the phase advance of the oscillation, again determined by the lattice design parameters. One key important figure acquired from this derivation is the tune (also called the betatron tune) of the accelerator, that is the number of oscillations per turn, given by

$$Q = \frac{1}{2\pi} \oint \frac{ds}{\beta(s)}. \qquad (1.28)$$

Off-Momentum Particles

During the operation of a particle accelerator we often have a spread of particle energies due to dynamics in the longitudinal plane [cite]. This gives rise to a momentum spread $\Delta p / p$ in the particle momentum. When considered in Eqn. **??** this gives rise to an inhomogenous differential equation of the form

$$\frac{d^2 x}{dz^2} + x\left(\frac{1}{\rho^2} - k\right) = \frac{\Delta p}{p}\frac{1}{\rho} \qquad (1.29)$$

which leads to a modified solution of the harmonic oscillator equation characterised by the dispersion of the lattice $D(s)$, written as

$$x(s) = \sqrt{\epsilon}\sqrt{\beta(s)}\cos(\psi(s) + \phi) + \frac{\Delta p}{p}D(s). \qquad (1.30)$$

This can be seen as another closed orbit solution to the machine lattice. One side effect of this is the slight change in the tune due to the off momentum, characterised by a factor known as the chromaticity ζ, related by

$$\frac{\Delta Q}{Q_0} = \zeta\frac{\Delta p}{p} \qquad (1.31)$$

where ΔQ is the tune shift from the lattice tune for an on momentum particle Q_0. The tune working point is an important factor in designing an accelerator as crossing integer or low order tune fractions (half, third or quarter integer) allows the summation of kicks in the machine driving large oscillations which may ultimately lead to particle loss.

Chapter 2

Wakefields and Impedance

2.1 Wakefields

Wakefields are the conventional name given to the phenomenon of induced electromagnetic fields due to charged particles traversing the beam pipe, RF cavities and many other pieces of equipment facing a particle beam in a particle accelerator. They have long been studied as a source of collective instabilities within particle accelerators [cite], through the use of analytical models for different beam pipe geometries[cite] and materials[cite], using computational simulation tools[cite], and both beam-based and bench-top measurement techniques. In this chapter is presented a number of significant properties of wakefields and their frequency domain counterpart, beam coupling impedance, as well an select example of observable effects that wakefields produce.

To aid in the explaination there will first be a short definition of the relative positions and labels of particles used in the following section. We define the source, or inducing particle as a charged particle with charge q_1 moving with velocity $\mathbf{v} = \beta c \tilde{\mathbf{z}}$ at coordinate $(\mathbf{r_1}) = x_1 \hat{\mathbf{x}} + y_1 \hat{\mathbf{y}} + z_1 \hat{\mathbf{z}}$, leading a test, or witness particle, with charge q_2, moving with velocity $\mathbf{v}$ at coordinate $(\mathbf{r_2}) = x_2 \hat{\mathbf{x}} + y_2 \hat{\mathbf{y}} + z_2 \hat{\mathbf{z}}$ at a distance $z_1 - z_2$ behind the source particle. This relationship is visualised in Fig. 2.1.

Figure 2.1: The relative displacements and velocities of the source and test particles.

2.1.1 The Electromagnetic Fields of a Moving Charged Particle in Free Space

If we consider the electromagnetic fields generated by the source particle, it can be shown that the fields at a vector $\mathbf{R} = \mathbf{r_1} - \mathbf{r_2}$ is given by

$$\mathbf{E}\left(\mathbf{R}\right) = \frac{q_1 \mathbf{R}}{\gamma^2 \left|\mathbf{R}\right|^3} \tag{2.1}$$

$$\mathbf{H}\left(\mathbf{R}\right) = \frac{1}{c}\mathbf{v} \times \mathbf{E} \tag{2.2}$$

where $\gamma = \sqrt{1 - v^2/c^2}$ is the relativistic gamma factor. It can be shown that, if we take the ultrarelativistic limit (i.e. $\gamma \to \infty$) we can see that Eqn 2.2 becomes

$$\mathbf{E}\left(\mathbf{R}\right) = \frac{2q_1 \mathbf{r}}{r^3}\delta z - ct\mathbf{H}\left(\mathbf{R}\right) = \hat{\mathbf{z}} \times \mathbf{E} \tag{2.3}$$

where $\mathbf{r} = x\hat{\mathbf{x}} + y\hat{\mathbf{y}}$ is a purely transverse vector.

The following witness particle this experiences the resulting lorentz force

$$\mathbf{F}\left(\mathbf{r_1}, \mathbf{r_2}\right) = q_2 \left[\mathbf{E} + \mathbf{v} \times \mathbf{B}\right]. \tag{2.4}$$

Looking at Eqn. 2.3, it can be seen that the force can be seperated into longitudinal and transverse components

$$F_\parallel\left(\mathbf{r_1}\mathbf{r_2}\right) = q_2 E_\parallel \tag{2.5}$$

$$\mathbf{F}_\perp\left(\mathbf{r_1}, \mathbf{r_2}\right) = q_2 \left[\mathbf{E}_\perp + \mathbf{v} \times \mathbf{B}\right] \tag{2.6}$$

where $E_\parallel = \mathbf{E}.\hat{\mathbf{z}}$ and $\mathbf{E}_\perp = E_x\hat{\mathbf{x}} + E_y\hat{\mathbf{y}}$. $F_\parallel$ has only an electric component as the magnetic flux density $\mathbf{B}$ has magnitude = 0 in the $\hat{\mathbf{z}}$ direction. Considering just the longitudinal force, integrating over all space gives the total energy change of the source particle

$$U_1\left(\mathbf{r_1}\right) = -q_2 \int_{-\infty}^{\infty} d\mathbf{z}.\mathbf{F}\left(\mathbf{r_1}, \mathbf{r_2}\right), \tag{2.7}$$

where $t = z_1/\beta c = z_1/c$ in the ultrarelativistic case. Similarly the energy change in the witness particle can be calculated by

$$U_2\left(\mathbf{r_1}, \mathbf{r_2}, \tau\right) = -q_2 \int_{-\infty}^{\infty} d\mathbf{z}\mathbf{F}\left(\mathbf{r_1}, \mathbf{r_2}\right), \tag{2.8}$$

where $t = z_1/\beta c = z_1/c + \tau$ and $\tau = \left(z_1 - z_2\right)/\beta c$ is the time between the source and witness particle. From these two energy losses two widely used terms can be extracted; the loss factor k, given by

$$k\left(\mathbf{r_1}\right) = \frac{U_1\left(\mathbf{r_1}\right)}{q_1} \tag{2.9}$$

and the longitudinal wake function, given by

$$w_{\parallel}\left(\mathbf{r_1}, \mathbf{r_2}, \tau\right) = \frac{U_2\left(\mathbf{r_1}, \mathbf{r_2}, \tau\right)}{q_1 q_2}, \tag{2.10}$$

denoting the normalised (with respect to source charge, and source and witness charge respectively) energy change of both the source particle (loss factor) and witness particle (wake function).

2.1.2 Wakefields of a Bunch

As colliders are often used to collide bunches of particles as opposed to single particles, it is useful to be able to define the wake function of a bunch distribution. It can be seen that the total source charge of a bunch q_1 is the integral of the longitudinal current distribution $i_b\left(\tau\right)$ integrated over all time

$$q_1 = \int_{-\infty}^{\infty} i_b\left(\tau\right) d\tau. \tag{2.11}$$

The wake function of a bunch distribution at a point at time τ can be calculated by the convolution of the single particle wake function with the bunch distribution. Thus, if the bunch is split into infinitesimally small slices, the change in energy of a witness particle of charge q at time τ due to a slice at time τ' is given by

$$dU\left(\mathbf{r_2}, \tau - \tau'\right) = q i_b\left(\tau'\right) w_{\parallel}\left(r_2, \tau - \tau'\right). \tag{2.12}$$

The longitudinal bunch wake function $W_{\parallel}\left(\mathbf{r_2}\right)$ can then be calculated using Eqn. 2.8

$$W_{\parallel}\left(\mathbf{r_2}, \tau\right) = \frac{U\left(r_2, \tau\right)}{q_1 q_2} = \frac{1}{q_1}\int_{-\infty}^{\infty} i_b\left(\tau'\right) w_{\parallel}\left(r_2, \tau - \tau'\right) d\tau'. \tag{2.13}$$

2.1.3 Transverse Wakefields

Similar to the longitudinal wakefield, we can see that the total tranverse momentum change of the witness particle is given by integrating the transverse force across all space

$$\mathbf{P}\left(\mathbf{r_1}, \mathbf{r_2}, \tau\right) = \int_{-\infty}^{\infty} \mathbf{F}_{\perp}\left(\mathbf{r_1 r_2}\right) dz \tag{2.14}$$

where $t = z_1/c + \tau$ and again τ is the time delay between source and witness particles. And similarly to the longitudinal plane we can define a wake function normalised with regards to the source and witness particle charges

$$\mathbf{w}_{\perp}\left(\mathbf{r_1}, \mathbf{r_2}, \tau\right) = \frac{\mathbf{P}\left(\mathbf{r_1}, \mathbf{r_2}, \tau\right)}{q_1 q_2}. \tag{2.15}$$

And in a similar manner to the longitudinal bunch wake function a form for the transverse bunch wake function can be derived

$$W_{\perp}\left(\mathbf{r_2}, \tau\right) = \frac{U\left(r_2, \tau\right)}{q_1 q_2} = \frac{1}{q_1}\int_{-\infty}^{\infty} i_b\left(\tau'\right) w_{\perp}\left(r_2, \tau - \tau'\right) d\tau'. \tag{2.16}$$

2.1.4 Panowsky-Wenzel Theorem

Considering the force acting on the witness particle it can be seen to simply by the Lorentz force

$$\mathbf{F} = q_2\left[\mathbf{E} + \mathbf{v} \times \mathbf{B}\right] \tag{2.17}$$

Now, considering Faraday's law in integral form ($\mathbf{B} = -\int_{t_1}^{t_2}\left(\nabla \times \mathbf{E}\right) dt$, t_1 being sufficiently in the past that $\nabla \times \mathbf{E} \to 0$), Eqn. 2.17 can be rewritten as

$$\mathbf{F} = q_2 \left[\mathbf{E} - \mathbf{v} \times \left(\int_{t_1}^{t_2} \nabla \times \mathbf{E} dt \right) \right]. \tag{2.18}$$

Now, using the fact that the velocity $\mathbf{v}$ is constant and some vector identities this then becomes

$$\mathbf{F} = q_2 \left[\mathbf{E} - \int_{t_1}^{t_2} \left(\nabla \left(\mathbf{v}.\mathbf{E} \right) - \mathbf{v} \left(\nabla.\mathbf{E} \right) \right) dt \right]. \tag{2.19}$$

If this force is seperated into the longitudinal and transverse components we see that they are the following

$$F_\parallel = q_2 E_z \tag{2.20}$$

$$\mathbf{F}_\perp = q_2 \left[\mathbf{E}_\perp - v \int_{t_1}^{t_2} \left(\nabla_\perp E_z - \frac{\partial \mathbf{E}_\perp}{\partial z} \right) dt \right] \tag{2.21}$$

where $\nabla_\perp$ in the differential operator only in the transverse coordinates. If these are now compared to the identities of the wake function for the longitudinal and transverse wake functions given in Eqns. **??** respectively, it can be seen that

$$w_\parallel \left(\mathbf{r_1}, \mathbf{r_2}, \tau \right) = -\frac{1}{q_1} \int_{-\infty}^{\infty} dz E_z \left(\mathbf{r_1}, \mathbf{r_2} \right) \tag{2.22}$$

$$\mathbf{w}_\perp \left(\mathbf{r_1}, \mathbf{r_2}, \tau \right) = \frac{1}{q_1} \int_{-\infty}^{\infty} dz \left[\mathbf{E}_\perp \left(\mathbf{r_1}, \mathbf{r_2} \right) - v \int_{t_1}^{t_2} \left(\nabla_\perp E_z \left(\mathbf{r_1}, \mathbf{r_2} \right) - \frac{\partial \mathbf{E}_\perp \left(\mathbf{r_1}, \mathbf{r_2} \right)}{\partial z} \right) dt \right]. \tag{2.23}$$

The next stage requires partially differentiating Eqn 2.23 by $s = v\tau = vt - z$. It can be seen from this relationship that $\partial / \partial s = -\partial / \partial z$ and $\partial / \partial s = 1/v \partial / \partial z$. Thus the first term can be replaced by $\partial / \partial s = -\partial / \partial s$, and the term the integral becomes the value of the intergrand at τ.

$$\frac{\partial}{\partial s} \mathbf{w}_\perp \left(\mathbf{r_1}, \mathbf{r_2}, \tau \right) = \frac{1}{q_1} \int_{-\infty}^{\infty} dz \left[\frac{-\partial}{\partial z} \mathbf{E}_\perp - \left(\nabla_\perp E_z + \frac{\partial \mathbf{E}_\perp}{\partial z} \right) dt \right]. \tag{2.24}$$

It can be seen that the first and third integrand cancel. Also, the operator $\nabla_\perp$ may be moved to the front of the operation without changing the equation, thus

$$\frac{\partial}{\partial s}\mathbf{w}_\perp\left(\mathbf{r_1},\mathbf{r_2},\tau\right) = \frac{1}{q_1}\int_{-\infty}^{\infty}dz\nabla_\perp E_z = \nabla_\perp w_\parallel\left(\mathbf{r_1},\mathbf{r_2},\tau\right).\qquad(2.25)$$

2.2   Impedances

In a particle accelerator there are a large number of components that have frequency dependent properties, either due to their geometry (for example resonant cavity structures) or material properties (frequency dependent permetivitty/permeability is devices, for example ferrite in normal conducting kicker magnets). In addition many instability mechanisms are strongly modal in nature, thus a frequency analysis of the possible sources of impedance is incredibly valuable.

2.2.1   Beam Coupling Impedance

The longitudinal beam coupling impedance $Z_\parallel$ and the transverse beam coupling impedance $Z_\perp$ are defined as the fourier transforms of the single particle wake function, given by

$$Z_\parallel\left(\mathbf{r_1},\mathbf{r_2},\omega\right) = \int_0^{\infty}d\tau w_\parallel\left(\mathbf{r_1},\mathbf{r_2},\tau\right)e^{-j\omega\tau}\qquad(2.26)$$

$$Z_\perp\left(\mathbf{r_1},\mathbf{r_2},\omega\right) = j\int_0^{\infty}d\tau w_\perp\left(\mathbf{r_1},\mathbf{r_2},\tau\right)e^{-j\omega\tau}\qquad(2.27)$$

where $\omega = 2\pi/\tau$. In a similar way the bunch wake function can be related to the longitudinal and transverse beam coupling impedance by considering the fourier transform of the time dependent bunch current $\lambda\left(\omega\right) = \int_{-\infty}^{\infty}d\tau i_b\left(\tau\right)e^{-j\omega\tau}$, which allows it to be shown that

$$W_\parallel\left(\mathbf{r_2},\tau\right) = \int_{-\infty}^{\infty}d\omega Z_\parallel\left(\mathbf{r_1},\mathbf{r_2},\omega\right)\lambda\left(\omega\right)e^{-j\omega\tau}\qquad(2.28)$$

$$W_\perp\left(\mathbf{r_2},\tau\right) = \int_{-\infty}^{\infty}d\omega Z_\perp\left(\mathbf{r_1},\mathbf{r_2},\omega\right)\lambda\left(\omega\right)e^{-j\omega\tau}.\qquad(2.29)$$

Figure 2.2: The relative displacements of the source and witness particle in the horizontal and vertical planes that identify the dipolar/driving and quadrupolar/detuning impedances.

2.2.2 Transverse Impedances

As can be seen in Eqn. 2.27, the transverse impedance is dependent on the displacement of both the source and witness particles. For reasons of simplifying beam dynamics evaluation, it is useful to distinguish the components dependent only on the transverse displacement of the source particle and that of the witness particle in the vertical and horizontal planes of the beam. This involves seperating the impedance firstly into horizontal and vertical components, and subsequently into components dependent only on the displacement of the source and of the witness particle. These are called the dipolar, or driving impedance and the quadrupolar, or detuning impedance respectively. In addition it can be shown that constant transverse terms exist which must also be taken into account. These are given by

$$Z_{\perp}\left(\mathbf{r_1}, \mathbf{r_2}, \omega\right) = Z_{\perp,x}\left(x_1, x_2, \omega\right) + Z_{\perp,y}\left(y_1, y_2, \omega\right) \tag{2.30}$$

$$Z_{\perp,x}\left(x_1, x_2, \omega\right) = Z_{dip,x}\left(x_1, \omega\right) + Z_{quad,x}\left(x_2, \omega\right) + Z_{const,x}\left(\omega\right) \tag{2.31}$$

$$Z_{\perp,y}\left(y_1, y_2, \omega\right) = Z_{dip,y}\left(y_1, \omega\right) + Z_{quad,y}\left(y_2, \omega\right) + Z_{const,y}\left(\omega\right). \tag{2.32}$$

The relative displacements of the source and witness particle are shown in Fig. 2.2 for clarity.

2.2.3 Geometric Impedance

Geometric impedances are characterised by resonant fields at a resonant frequency, typically characterised by some characteristic dimension of the structure. This is typically a characteristic length of a structure (cavity size, antenna length), which may be part of a vacuum tank, or an internal structure to the device exhibiting the resonance.

As a simple example, consider a cylindrical pillbox cavity of radius r_{cav} and length L connected to a beam pipe of radius r_{pipe} located at the centre of the cavity, as shown in

44

Figure 2.3: Cross section of a cylindrical pillbox cavity with an attached beam pipe

Fig. 2.3. For simplicity we shall assume that the cavity is made from a perfectly conducting materials. It shall be assumed that the fields do not propogate along the attached beam pipe (i.e. for frequencies below cutoff). In this example we shall consider a particle travelling on the axis of the beam pipe, and only the longitudinal wakefunction/impedance will be investigated to simplify matters. Further details can be found in [cite Andy Wolzski, E Jensen, Stupakov]. It can be shown that there are two families of resonant modes in in a pillbox cavity, TM-type modes and TE-type modes. The TE-type modes have no longitudinal electrical field by definition, and therefore do not contribute to the longitudinal wakefunction for an on axis particle. In a cylindrical coordinate system using coordinates (r, θ, z), the longitudinal electrical field of the n-th order TM-type modes can be shown to be

$$E_{z,n} = E_0 J_n \left(k_r r \right) cos \left(n\theta \right) cos \left(k_z z \right) e^{-j\omega t} \tag{2.33}$$

where E_0 is the magnitude of the electric field, J_n is n-th order Bessel function, $k_z = n\pi/L$, and n is an interger. A wakefunction for each mode subsequently be defined as $w_{\parallel,n} \left(\tau \right)$, where the total wakefunction is thus defined as

$$w_\parallel \left(\mathbf{r}_1, \mathbf{r}_2, \tau \right) = \sum_{n=0}^{\infty} w_{\parallel,n} \left(\tau \right) = \sum_{n=0}^{\infty} \int_{-\infty}^{\infty} dz E_{z,n} \left(r, \theta, z \right) \tag{2.34}$$

To evaluate the problem in the frequency domain we shall introduce the RLC parallel circuit model to simplif the frequency doman representation.

RLC Circuit Model

We can define any given resonance by an equivalent RLC circuit, which is driven by a current, shown in Fig. 2.4. The symbols represent the equivalent resistor (R), inductance (L) and capcitance (C). From this circuit a number of defining parameters are now deduced, and the physical equivalents in the physical cavity are described.

Figure 2.4: The equivalent RLC parallel circuit for a cavity resonance, driven by a current i_b, in this cas the beam current

The first parameter to be derived is the resonant frequency of the cavity mode itself ω_0. This can be shown (by solving the time varying voltage build up of the circuit in Fig. 2.4) to be given by

$$\omega_0 = \frac{1}{LC}. \tag{2.35}$$

Next we define the quality factor of the cavity mode, Q_n. This factor describes the damping of the wakefunction in the cavity for a given mode, larger values indicating a longer damping time. In terms of the cavity it is given by

$$Q_n = \frac{\omega_0 W}{P_{loss}} = \omega_0 RC \tag{2.36}$$

where $W = \int_V \epsilon/2 \, |\mathbf{E}|^2 \, dV$ is the stored electromagnetic energy in the cavity due to the mode, and P_{loss} is the total losses in the cavity. Commonly the later is dominated by conductive losses on the cavity walls, but as will be seen in later sections, also includes losses due to other mechanisms. The final figures of merit are the $R_{s,n}/Q_n$ of the cavity mode, and the shunt impedance $R_{s,n}$ of the mode. $R_{s,n}/Q_n$ is given by

$$\frac{R_{s,n}}{Q_n} = \frac{|V_{acc}|^2}{2\omega_0 W} \tag{2.37}$$

where $V_{acc} = \int_{-\infty}^{\infty} E_{z,n} e^{-j\omega_0 z/\beta c} dz$ is the effective voltage that a traversing particle sees due to the cavity mode. It can thus be seen that the $R_{s,n}/Q_n$ of a cavity mode gives some ratio of the acceleration of a traversing particle to the stored energy. The shunt impedance $R_{s,n}$ is then given by

$$R_{s,n} = \left(\frac{R_{s,n}}{Q)n}\right) Q_n = \frac{|V_{acc}|^2}{2P_{loss}} \tag{2.38}$$

or an equivalent ratio for power loss in the cavity to acceleration of the particle. From these quality factors is defined a broadband description of the beam coupling impedance at all frequencies due to all modes, given by

46

Figure 2.5: The geometry of the classical thick wall formula.

$$Z_\parallel (\omega) = \sum_{n=0}^{\infty} Z_{\parallel,n} (\omega) = \sum_{n=0}^{\infty} \frac{R_{s,n}}{1 - iQ \left(\frac{\omega}{\omega_0} - \frac{\omega_0}{\omega} \right)}.$$ (2.39)

And number of examples of this type of impedance are shown in Sec. 2.3.1

2.2.4   Resistive Wall Impedance

The resistive wall impedance is an impedance generated due to the finite conductivity of the material of the beam pipe wall. This can have a number of regimes dependent on whether the skin depth of the material $\delta (\omega) = \sqrt{\frac{2}{\mu_0 \sigma \omega}}$ is much smaller than the thickness of the beam pipe wall [ref classical thick wall formalism], comparable to the thickness of the beam pipe wall [ref redistribution effect] or much larger than the thickness of the beam pipe wall [ref dielectric or ferrite impedances]. In this instance, σ is the conductivity of wall material. It can also be shown that the shape of the beam pipe cross section also plays a significant role in defining the impedance [ref mounet axisymmetric/parallel plate].

Here we shall not attempt a comprehensive summary of the various resistive wall impedance models, but simply give an introduction to the classic thick wall formalism to give a sense of how changing the wall conductivity affects the resistive wall impedance. A considerably more detailed overview of this derivation can be found in [cite Chao]. Consider a circular beam pipe of radius a containing a source particle of charge q_1 moving with velocity $\mathbf{v} = \beta c \hat{\mathbf{z}}$, as shown in Fig. 2.5. In this case it shall be assumed that $\beta = 1$.

It can be shown that the beam coupling impedance per unit length L of this structure, assuming $\delta \ll b$ is given by [cite Chao]

$$\frac{Z_\parallel^0 (\omega)}{L} = \frac{1 - sgn(\omega) i}{2\pi a \delta \sigma}$$ (2.40)

$$\frac{Z_\perp^1 (\omega)}{L} = \frac{c}{\omega} \frac{1 - sgn(\omega) i}{2\pi a^3 \delta \sigma}$$ (2.41)

where sgn is a function that returns the sign (positive or negative) of the value. The 0 and 1 indicate these modes represent the zeroeth and first azimuthal modes of the source

(a)(b)

Figure 2.6: Examples of the longitudinal 2.6(a) and transverse 2.6(b) resistive wall impedance of a beam pipe of radius $a = 2cm$ made of both copper ($\sigma = 1 \times 10^7 Sm^{-1}$) and graphite ($\sigma = 7 \times 10^4 Sm^{-1}$.

current. It can be easily seen is that the impedance is proportional to $1/\sqrt{\sigma}$, thereby indicating that materials with a higher conductivity generally give lower beam coupling impedance in the thick wall regime (See Fig. 2.6 for a comparison between two sample materials).

- Return to simple axisymmetric geometry concerning a finite conductivity of the wall

- Derive in frequency domain - then have impedance. Give an example wakefield of a good conductor (copper), bad conductor (graphite), non-conductor (ferrite)

2.3 Example of the Effects of Wakefields

To give context to the effects that wakefields have on the both the beam and equipment with a particle accelerator, two types of wakefield/impedance driven phenomena are discussed here. The first, beam-induced heating, is an example of beam induced wakefields having an effect on the machine itself contributing to heat loads due to the energy lost by the beam and subsequently dissipated within the surrounding equipment. The second, beam instabilities, covers a number of examples of instability mechanisms that may be driven by wakefields, in particular due to the harmonic nature of particle and beam behaviour in a circular accelerator.

2.3.1 Beam Induced Heating

Defining and Deriving Power Loss in Circular Accelerators

When a charged particle interacts with an impedance it losses energy to generate the resulting wakefield. This is called the parasitic loss, and is generally defined as[ref

Chao/Ng]

$$\Delta E = -2\pi e^2 N_b \int_{-\infty}^{\infty} d\omega \, |\lambda(\omega)|^2 \, Z_{\parallel}(\omega) \tag{2.42}$$

where ΔE is the energy loss per pass per particle, e is the charge per particle, N_b, ω the frequency, λ the line density of the bunch and $Z_{\parallel}$ the longitudinal impedance of the object being traversed.

Due to the decay of the wakefields induced by this energy loss, this energy must eventually be lost to the device causing the impedance (valid below the cutoff frequency of the machine beam pipe). Therefore we can assume that the energy loss from the particles is absorbed by the surrounding structure. Summing over all particles in a bunch we can therefore obtain a sum of the energy loss;

$$\Delta E_{bunch} = 2\pi \, (eN_b)^2 \int_{-\infty}^{\infty} d\omega \, |\lambda(\omega)|^2 \, Z_{\parallel}(\omega) \tag{2.43}$$

As often we must deal with machines storing multiple bunches, for these we simply multiply the energy loss per bunch by the number of stored bunches to acquire the total energy loss per passage;

$$\Delta E_{bunches} = 2\pi \, (eN_b)^2 \, n_{bunch} \int_{-\infty}^{\infty} d\omega \, |\lambda(\omega)|^2 \, Z_{\parallel}(\omega) \tag{2.44}$$

where n_{bunch} is the number of bunches in the machine. If we assume a revolution frequency f_{rev} we thus get a power loss of;

$$
\begin{aligned}
P_{loss} &= \Delta E_{bunches} f_{rev} \\
&= 2\pi f_{rev} \, (eN_b)^2 \, n_{bunch} \int_{-\infty}^{\infty} d\omega \, |\lambda(\omega)|^2 \, Z_{\parallel}(\omega) \\
&= 2\pi f_{rev} \, (eN_b)^2 \, n_{bunch} \int_{-\infty}^{\infty} d\omega \, |\lambda(\omega)|^2 \, Z_{\parallel}(\omega) \\
&= 2\pi f_{rev} \, (eN_b)^2 \, n_{bunch} \int_{-\infty}^{\infty} d\omega \, |\lambda(\omega)|^2 \left(\Re e \left(Z_{\parallel}(\omega) + \Im m Z_{\parallel}(\omega) \right) \right).
\end{aligned}
\tag{2.45}
$$

As $\Re e \left(Z_{\parallel}(\omega) \right)$ is an even function and $\Im m \left(Z_{\parallel}(\omega) \right)$ is an odd function, we see that

$$P_{loss} = \omega_{rev} \left(eN_b\right)^2 n_{bunch} \int_0^\infty 2d\omega \left|\lambda\left(\omega\right)\right|^2 \Re e\left(Z_\parallel\left(\omega\right)\right). \tag{2.46}$$

Next we make a change of the variable of integration $\omega = n_{bunch}\omega_{rev}$;

$$P_{loss} = \omega_{rev} \left(eN_b\right)^2 n_{bunch}^2 \int_0^\infty 2d\omega_{rev} \left|\lambda\left(\omega_{rev}n_{bunch}\right)\right|^2 \Re e\left(Z_\parallel\left(\omega_{rev}n_{bunch}\right)\right). \tag{2.47}$$

We can subsequently change to a sum formalism to obtain

$$P_{loss} = \left(\omega_{rev}eN_bn_{bunch}\right)^2 \sum_{p=0}^\infty \left(2\left|\lambda\left(p\omega_{rev}n_{bunch}\right)\right|^2 \Re e\left(Z_\parallel\left(p\omega_{rev}n_{bunch}\right)\right)\right) \tag{2.48}$$

where $\omega_0 = 2\pi f_0$, $f_0 = \frac{1}{\tau_b}$ and τ_b is the bunch spacing.

Longitudinal Beam Profiles

As shown by the derivations in Section 2.3.1, asides from the longitudinal impedance of the device under consideration the longitudinal profile of the circulating bunches also contributes to the power loss in the machine. In past works it has generally been assumed that bunches in accelerators have a Gaussian profile [ref Sacherer/Grudiev/Laclare](seen in Eqn. 2.49, where $4\sigma_z = t_b$, t_b is the bunch length) when approaching the analytical treatment of beam instabilities, both single-bunch and multi-bunch. Recent measurements of the power spectrum of particle beams, especially in the LHC [ref theo/phillipe] have shown characteristics that the Gaussian profile does not predict, for example the high frequency secondary peak as seen in Fig. 2.7. To make more realistic predictions of heat loss due to beam impedance in the machine it is thus necessary to find bunch profiles which reproduce this behaviour.

$$\lambda\left(t\right) = e^{\frac{-t^2}{2\sigma^2}} \tag{2.49}$$

A number of different longitudinal bunch profiles have been investigated in the past. Here we shall look at 3 other bunch profiles; a parabolic line density (see Eqn. 2.50), $\cos^2$ (see Eqn. 2.51), water-bag (see Eqn. 2.52).
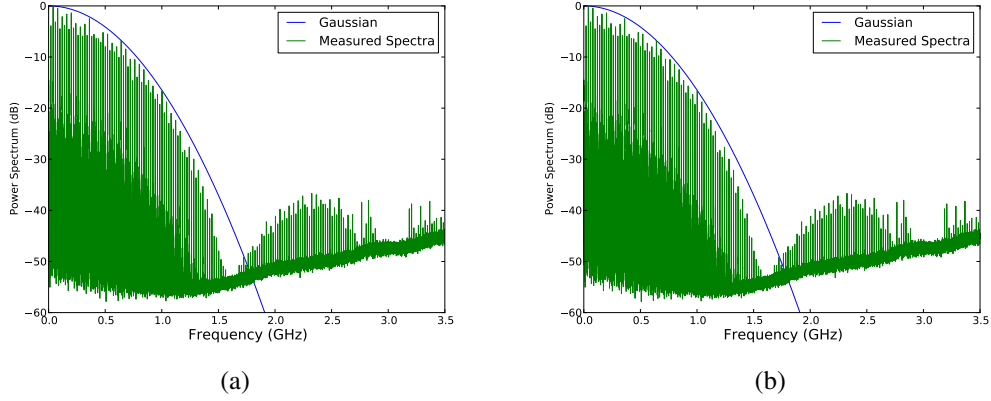
Figure 2.7: A comparison of 2.7(a) a measured beam power spectrum and a gaussian bunch of the same bunch length in the frequency domain and 2.7(b) the resulting time domain beam profile. The gaussian has a bunch length ($4\sigma_z = 1.2$ns)

$$A\left(t\right) = \int_{-\infty}^{\infty} \lambda\left(\omega\right) e^{j\omega t} d\omega = \begin{cases} 1 - \left(\frac{2t}{t_b}\right)^2 & \text{if } |t/2| \leq t_b \\ 0 & \text{if } |t/2| > t_b \end{cases} \tag{2.50}$$

$$A\left(t\right) = \int_{-\infty}^{\infty} \lambda\left(\omega\right) e^{j\omega t} d\omega = \begin{cases} cos^2\left(\frac{\pi t}{t_b}\right) & \text{if } |t/2| \leq t_b \\ 0 & \text{if } |t/2| > t_b \end{cases} \tag{2.51}$$

$$A\left(t\right) = \int_{-\infty}^{\infty} \lambda\left(\omega\right) e^{j\omega t} d\omega = \begin{cases} \sqrt{1 - \left(\frac{2t}{t_b}\right)^2} & \text{if } |t/2| \leq t_b \\ 0 & \text{if } |t/2| > t_b \end{cases} \tag{2.52}$$

The comparison of these bunch profiles in the time domain are shown in Fig. 2.3.1. Note all bunch currents are normalised to their peak value. The corresponding current and power spectrums are shown in Fig. 2.3.1. There are several things to note about these spectra; firstly that the non-infinite distribution of the non-gaussian bunch profiles gives rise to a number of high frequency lobes in the power spectrum, and secondly the interval of these nodes depends heavily on the bunch profile.

To illustrate more clearly the effect of changing the bunch length on the power spectrum, a number of bunch profiles and the corresponding power spectra with different bunch lengths are shown below. Firstly, consider a gaussian bunch profile. It can be seen in Fig. 2.10 that by increasing the bunch length that the magnitude at high frequencies is
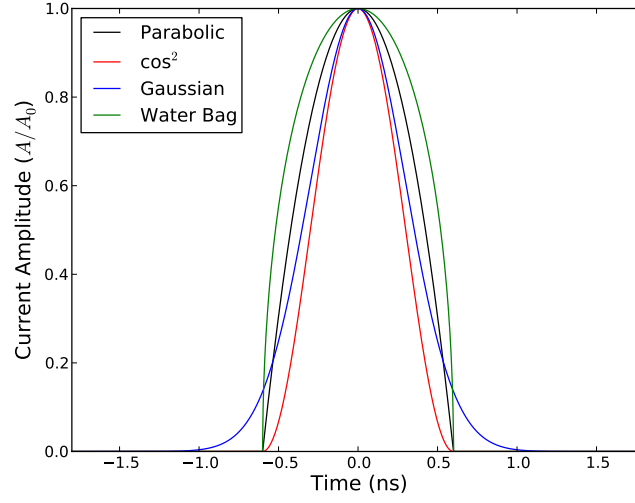
Figure 2.8: The longitudinal bunch profile of a number of bunch distributions. Note that all of them are normalised to have a peak bunch current of 1. For the gaussian distribution the bunch length is the 4σ value. The bunch length $\tau_b = 1.2ns$

| (a) | (b) |
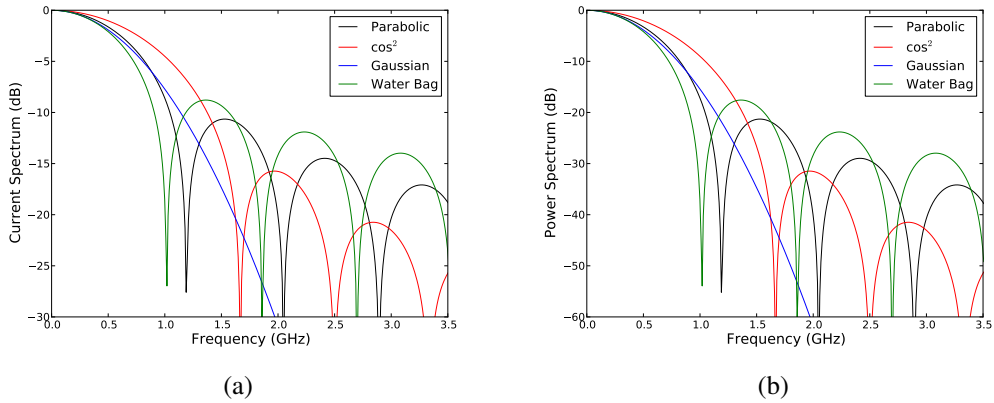
Figure 2.9: The frequency domain 2.9(a) current spectrum and 2.9(b) power spectrum for a number of different bunch profiles with a bunch length $\tau_b = 1.2ns$.

52
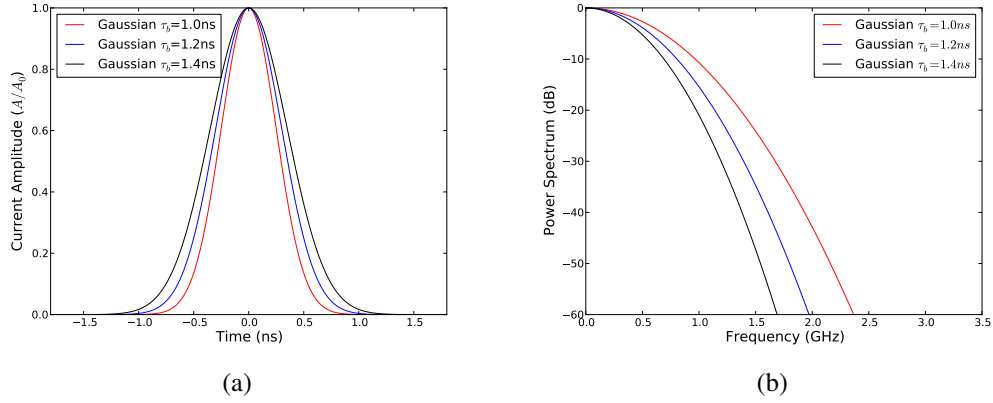
Figure 2.10: 2.10(a) The longitudinal profile and the 2.10(b) associated bunch power spectrum for a number of bunch lengths assuming a gaussian bunch profile.
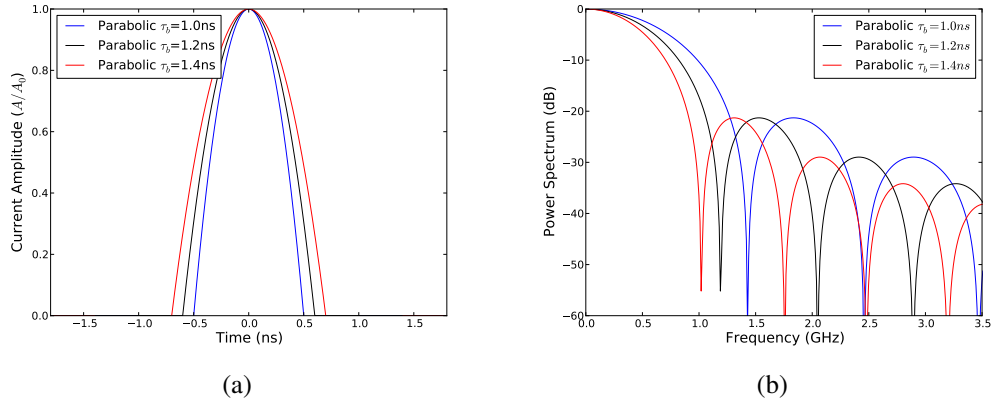
Figure 2.11: 2.11(a) The longitudinal profile and the 2.11(b) associated bunch power spectrum for a number of bunch lengths assuming a parabolic bunch profile.

decreased quite substantially as the bunch length increases. If we consider a finite bunch profile (non-gaussian), we note that we have high frequency lobes. The peak frequency of these lobes depends on the bunch length, as illustrated using a parabolic bunch profile for bunch lengths $\tau_b = 1ns, 1.2ns, 1.4ns$ in Fig. 2.3.1. As the bunch length is increased the lobes move to lower frequencies, and the width of the first branch decreases, as seen for the gaussian bunch. Similar behaviour is observed with the $\cos^2$ and water-bag bunch profiles.

Finally, a comparison of a measured bunch power spectra and the analytical power spectra is shown in Fig. 2.3.1. It can be seen that whilst it is possible to replicate some of the properties of the measured spectrum, an exact replication is non-trivial. Further
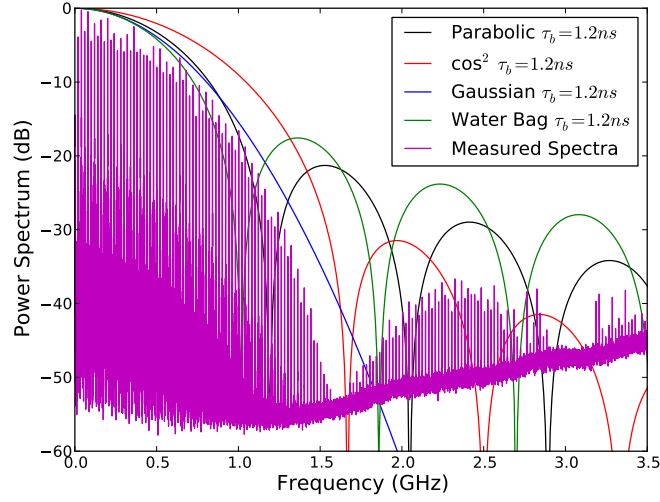
Figure 2.12: A comparison of a measured beam power spectrum and a number of analytical bunch profiles assuming a bunch length of 1.2ns.

investigation into the appropriate bunch profile is ongoing.

Beam induced heating due to a low Q impedance

For an impedance with a characteristic Q that is small (Q $<$ 10), it can be seen that the impedance peak will interact substantially with a number of beam harmonics (see Fig. 2.3.1) due to the broad frequency range it occupies.

Further investigation of the longitudinal beam spectrum reveals that there is significant structure between the major harmonics (which are due to the bunch spacing of the beam) which can be attributed to the other time structures of the beam, for example the bunch train spacing, or the interval between the pilot bunch train and the subsequent bunch train. As such the treatment of the estimation of beam losses requires a broad spectrum approach. If we consider Eqn.2.46 we see that we can treat the power losses in an integral form. We can observe a number of properties using this assumption. The power loss is proportional to the beam properties in the following manner:

1. $P_{loss} \propto N^2$

2. $P_{loss} \propto n_{bunch}$

54
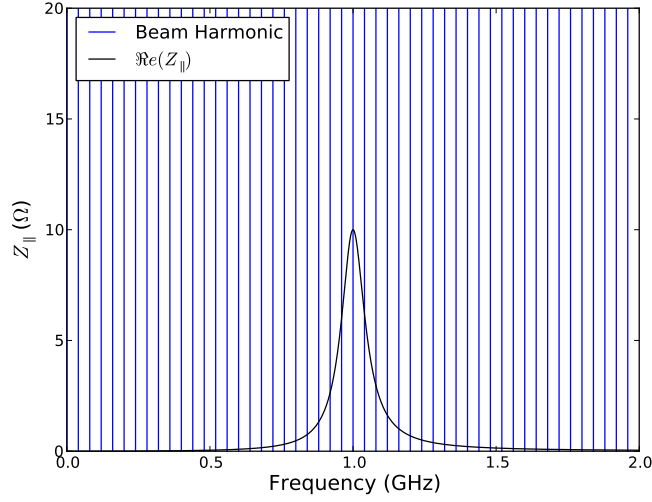
Figure 2.13: The beam harmonics of a beam with a bunch spacing of 25ns overlayed on the real component of the longitudinal impedance an example of a low Q impedance ($R_s = 10\omega$, Q = 10, $f_{res} = 1GHz$). The blue lines represent the frequency of a beam harmonic, not necessarily the magnitude of the power spectrum at that point. Note that a number of beam harmonics overlay non-zero impedance values.

Beam induced heating due to a high Q impedance

In contrast to the overlap of the beam spectrum with a low Q impedance, for a high Q impedance only one beam harmonic lies upon the resulting impedance to any significant quantity. This is illustrated in Fig 2.3.1 If we consider Eqn **??** and consider the situation where

$$
\left(2\left|\lambda\left(p\omega_{rev}n_{bunch}\right)\right|^2 \Re e\left(Z_\parallel\left(p\omega_{rev}n_{bunch}\right)\right)\right) = \begin{cases} \left(2\left|\lambda\left(\omega_{res}\right)\right|^2 \Re e\left(Z_\parallel\left(\omega_{res}\right)\right)\right) & \text{if } p\omega_{rev}n_{bunch} = \omega_{res} \\ 0 & \text{if } p\omega_{rev}n_{bunch}! = \omega_{res} \end{cases}
$$

$$(2.53)$$

It can then be seen that Eqn **??** simplifies to

$$
P_{loss} = \left(\omega_{rev}eN_bn_{bunch}\right)^2\left(2\left|\lambda\left(\omega_{res}\right)\right|^2 \Re e\left(Z_\parallel\left(\omega_{res}\right)\right)\right).
$$

$$(2.54)$$

The following properties can subsequently be seen as a result:
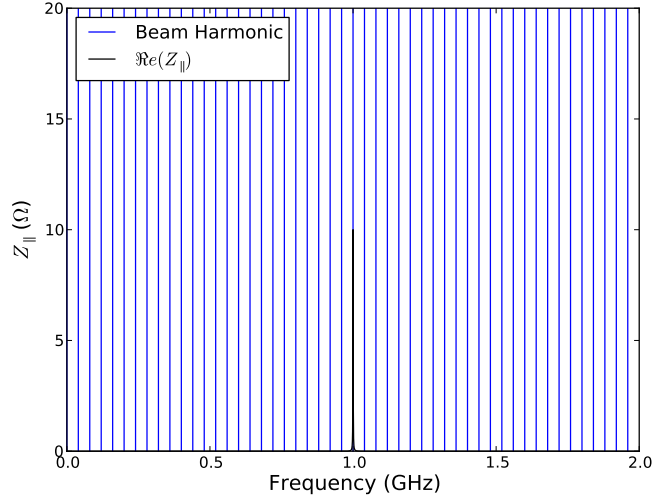
Figure 2.14: The beam harmonics of a beam with a bunch spacing of 25ns overlayed on the real component of the longitudinal impedance an example of a high Q impedance ($R_s = 10\omega$, Q = 1000, $f_{res} = 1GHz$). The blue lines represent the frequency of a beam harmonic, not necessarily the magnitude of the power spectrum at that point. Note that only a single beam harmonic overlays a non-zero impedance values.

1. $P_{loss} \propto N^2$

2. $P_{loss} \propto n_{bunch}^2$, provided that the resonant frequency of the resonance continues to coincide with a beam harmonic.

Some Examples of the Beam-Induced Heating

In this section we shall illustrate some important factors that have been covered in previous sections. In particular, the interaction of different bunch profiles at different bunch lengths with an example cavity resonance will be covered in some detail to illustrate how the estimated heating can change drastically depending on higher frequency lobes in the beam current spectrum. In addition, the heating due to two particle beams in the same vacuum chamber shall be briefly covered for interest.

The Effect of Bunch Length on Power Loss

As can be seen in Figs. 2.3.1 and , the bunch profile and the bunch length can significantly alter the magnitude of the beam current at higher frequencies. To illustrate this, let us consider two resonant impedances, one broadband Z_{bb} and one narrow band Z_{nb} impedance, characterised by having a low-Q and a high-Q respectively. Both impedances shall have the same resonant shunt impedance $R_s = 100\Omega$. The broadband impedance shall have a $Q_{bb} = 1$, and the narrow band impedance $Q_{nb} = 1000$. The resonant frequency will be changed to illustrate effects in different regimes of the bunch length and of different bunch profiles.

We shall use the gaussian bunch profile and the cos^2 bunch profile for these examples. The gaussian is useful to illustrate the effect of just the changing bunch length, and the cos^2 due to the presence of a high frequency lobe in it's frequency domain current spectrum. The cos^2 frequency domain current profile is given by

$$I\left(\omega\right) = \frac{sin\left(\omega\tau_b/2\right)}{\omega\tau_b/2\left[1 - \left(\omega\tau_b/2\right)^2\right]}. \tag{2.55}$$

First we shall consider a narrowband impedance which has a resonant frequency $\omega_0 = 2GHz$ which falls upon a beam harmonic such that $\omega_0 = n\omega_{rev}$ where n is an integer. It should be noted that for other cases the contribution of these sources of heating is negligible due to the small beam current at this frequency. There are two extreme cases; that of $\omega_0 \gg 1/\tau_b$, in which it can be seen that the current spectrum will be negligible at the frequency of the impedance, and $\omega_0 \ll 1/\tau_b$ where the beam current spectrum is essentially the same as the DC spectral component. The transition in this intervening regime is shown in Fig 2.3.1, assuming a bunch current of 1A. It can be seen that in this case the heating falls drastically as the bunch length increases.

If we instead consider a cos^2 distribution we instead see the effect of the secondary lobes in the beam current spectrum. The power loss with bunch length is shown in Fig. **??** in comparison to that of the gaussian profile. The beam power spectrum for a number of different bunch lengths are shown with the real component of the longitudinal impedance
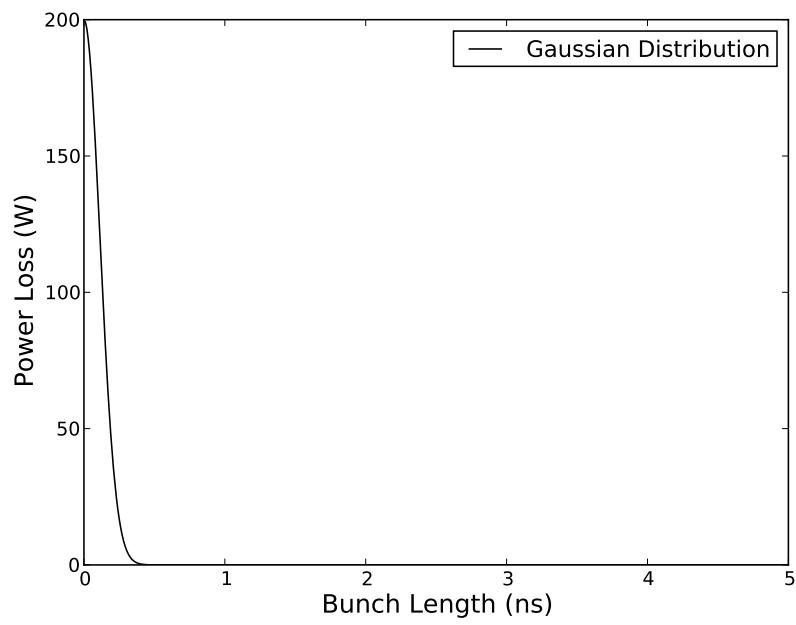
Figure 2.15: The change in power loss due to a narrow band resonance characterised by $\omega_0 = 2GHz$, $R_s = 100\Omega$, $Q = 1000$ with a gaussian bunch distrbution of different lengths.
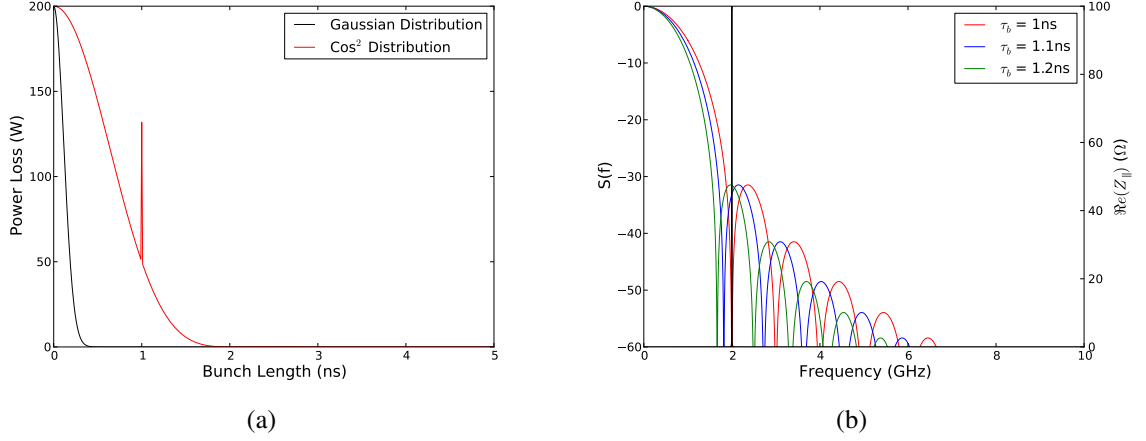
Figure 2.16: 2.16(a) The change in power loss due to a narrow band resonance characterised by $\omega_0 = 2GHz$, $R_s = 100\Omega$, $Q = 1000$ interacting with a $\cos^2$ bunch distribution with different bunch lengths. The impedance and the beam power spectrum are shown in 2.16(b) to illustrate how this relates to the power loss.

in Fig. 2.16(b). Here it can be clearly seen that the intersection of the secondary lobe with the resonant impedance causes a peak in the power lost by the beam, highlighting the neccessity to be aware of the resonant frequencies of resonant impedances with relation to the beam harmonics.

For the broadband heating we shall consider a resonant impedance defined by the following parameters, $\omega_0 = 2GHz$, $Q = 1$, $R_s = 100\Omega$. To account for the multiple beam harmonics that will interact with the resonance, it is assumed that the beam harmonics in this case occur at 20MHz intervals. The impedance and the beam power spectrum is shown in Fig. 2.17(a) and the resulting power loss in Fig. 2.17(b) where it can be seen that the power loss decreases slowly with increasing bunch length. This is due to the significant contribution to the power loss at low frequencies, in which the component of the beam power spectrum decreases only marginally due to the decreasing bunch length.

Beam-Induced Heating due to two traversing beams

Previous work [cite A. Grudiev TCTVB/TCLIA] has investigated the effect of two beams in a vacuum on the beam-induced heating. This is restated here for the sake of completeness.
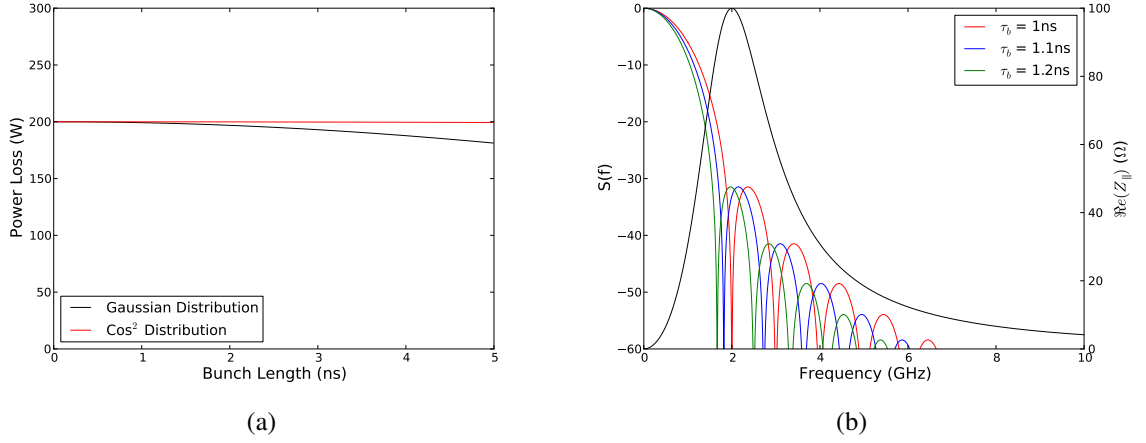
Figure 2.17: 2.17(a) The change in power loss due to a narrow band resonance characterised by $\omega_0 = 2GHz$, $R_s = 100\Omega$, $Q = 1$ interacting with a $\cos^2$ bunch distribution with different bunch lengths. The impedance and the beam power spectrum are shown in 2.17(b) to illustrate how this relates to the power loss.

To begin, consider the two currents $I_{b1} = I_0 e^{i\phi_1}$ and $I_{b1} = -I_0 e^{i\phi_2}$ representing two counter rotating beams. I_0 represents the beam current, and $\phi_{1/2}$ the phase of beam 1 and beam 2 respectively. Each beam also sees a seperate potential when it traverses the impedance, given by $V_{b1} = \int_{b1} E_z e^{i\omega_0 z/c} dz$ and $V_{b2} = \int_{b2} E_z e^{i\omega_0 z/c} dz$ respectively. By Ohms law it can then be seen that

$$\begin{pmatrix} V_{b1} \\ V_{b2} \end{pmatrix} = \begin{bmatrix} Z_{11} & Z_{12} \\ Z_{21} & Z_{22} \end{bmatrix} \begin{pmatrix} I_{b1} \\ I_{b2} \end{pmatrix}.$$ (2.56)

The power loss due to both beams can then be seen to be

$$P_{loss} = \begin{pmatrix} V_{b1} & V_{b2} \end{pmatrix} \begin{pmatrix} I_{b1} \\ I_{b2} \end{pmatrix}^{*}.$$ (2.57)

In the worst case scenario, the values of the impedance matrix are real, and are equal in value to the peak values of the resonant impedance

$$Z_{11} = 2R_s^{b1}; \ Z_{22} = 2R_s^{b2}; \ Z_{12} = Z_{21} = 2\sqrt{R_s^{b1} R_s^{b2}}.$$ (2.58)

The power loss then becomes

$$P_{loss} = I_0^2 2 \left(R_s^{b1} + R_s^{b1} - 2\sqrt{R_s^{b1} R_s^{b2}} \cos\left(\delta\phi \right) \right)$$ (2.59)

60

where $\delta\phi = \phi_1 - \phi_2$ is the phase difference between beam 1 and beam 2. This can be found relatively easy by comparing the distance δs from a collision IP of the machine. Assuming the beams are ultrarelativistic $\delta\phi = \omega_{rev}2\delta s/c$. It can then be seen that the the last term may either reduce or increase the power loss depending on whether $cos\left(\delta\phi\right) = 1$ or $cos\left(\delta\phi\right) = -1$ respectively.

2.3.2 Beam Instabilities

Beam Instabilities is the collective term for a various group of mechanisms which attribute to the degradation of beam properties during the circulation of a beam within a synchrotron. These can typically be into a number of different subgroups, summarised below:

1. Coherent Effects - Occuring due to the bulk oscillation of the bunch(es)

2. Incoherent Effects - Occuring due to a mechanism that effects particles dependent on their position within in the bunch

3. Single-Bunch - Occuring only on the scale of a single bunch

4. Multi-Bunch - Occuring due to coupling of the motion between multiple bunches.

The mechanisms driving these instabilities are multitudinous and of which beam coupling impedance is just one. Others include space charge effects (both direct and indirect)[cite], beam-beam interactions [cite], electron cloud [cite], IBS [cite] amongst others. Here we shall give a brief overview of how these effects cause a degradation in beam operation.

Tune Shift and Tune Spread

As seen in Sec. [ref introduction transverse motion], the transverse equation of motion can be viewed as an oscillatory system. If the particles experience an additional force F_x^{pert} due an external mechanism, not due to the machine optics, it's equation of motion (in the horizontal plane, for example) can be written as

Figure 2.18: A tune diagram illustrating the unperturbed tune of a machine, and the resulting perturbed tune and the tune spread as a result of an impedance source. Note that the tune spread has caused some particle to lie upon a major resonance harmonic.

$$\frac{d^2x}{ds^2} + \left(\frac{Q_{0,x}}{R}\right)^2 x = \frac{F_x^{pert}}{\beta^2 E_{total}}. \tag{2.60}$$

This subsequently leads to a perturbed oscillation frequency, characterised by the equation

$$\frac{d^2x}{ds^2} + \left(\frac{Q_{0,x} + \Delta Q_{pert,x}}{R}\right)^2 x = 0. \tag{2.61}$$

where $\Delta Q_{pert,x}$ is the part of the betatron frequency caused by the perturbing force. The perturbed tune may also be subsequently be further divided into coherent (the motion of the bunch centroid) and incoherent (motion of individual particles), such that $\Delta Q_{pert,x} = \Delta Q_{pert,x}^{coh} + \Delta Q_{pert,x}^{incoh}$. This seperation leads to the creation of a tune spread in a machine, in which the tune of the beam covers an area of the tune diagram as shown in Fig. 2.18. In this case particles may be lost when this tune shift causes them to lie upon a major resonance of the beam optics, there by causing cpherent oscillation growth and ultimately particle loss. This leads to negative effects such as emittance growth and lower beam lifetimes.

Longitudinal Single Bunch Instabilities

Similar to the change in the equations of motion for transverse particles, considering the induced fields in the longitudinal plane produces a perturbation in the longitudinal motion also. This can be thought of as an additional force alongside the electromagnetic force applied by the accelerating cavities. This leads to two interesting phenomenon; potential well distortion, occuring at bunch intensities below some stability criteria, and longitudinal mode coupling instability, or LMCI, above some stability criteria.

The potential well distortion is a direct effect of the incoherent synchrotron tune shift (again, similar in nature to the tune shifts experienced in the transverse plane), which is

Figure 2.19: The change in the bunch length of a proton beam in an SPS like machine due to the effects of a broadband resonator impedance (). Note that the bunch length increases when the beam is above transition, and decreases below transition, as the bunch intensity is increase

responsible for a growth in the stable emittance of the bunch. This reveals itself from measurements by a change in the bunch length with increasing bunch intensity, as shown in Fig. 2.19. It should be noted that depending on the source of impedance, the bunch length may increase or decrease depending on whether the bunch is above or below the transition energy of the accelerator.

LMCI occurs when a certain intensity threshold is crossed in the accelerator, leading to a regime known as *turbulent bunch lengthening*. In this mechanism the eigenfrequencies of the natural modes of oscillation of the particles within the RF bucket are shifted due to the changing potential due to the induced wakefield. In high intensity bunches two neighbouring modes may have their frequencies shifted to such an extent that the modes merge into one, thus leading to a case where the modes no longer have only a damped solution, but also a exponentially growing solution. This subsequently leads to the bunch oscillations becoming unstable.

Transverse Single Bunch Instabilities

In the transverse plane a number of instability mechanisms apply, which maybe seperated into two forms, those that occur on a time scale much shorter than the synchrotron period, and those that occur on a longer time scale than the synchrotron period. In both cases the leading particles of the bunch, often called the head of the bunch, drives and oscillation in the end, or tails of the bunch. This gives these instabilities their names, the fast head-tail instability, or transverse mode coupling instability (TMCI) and the head-tail instability.

In the case of the fast head-tail instability, the are a number of transverse oscillation modes (see Fig. 2.20 for examples), which as with the LMCI experience some frequency shift due to the presence of a wakefield. If the shift is large enough, two of these modes may again couple together, causing an exponential growth of the transverse size of the

Figure 2.20: Examples of a number of modes of transverse oscillation. Note that radial and azimuthal modes may occur, as may coupled modes in which the motion of the horizontal and vertical planes is coupled.

bunch to occur.

In the case of the head-tail instability, the movement of a particle from the head of the bunch to the tail and vice versa become important in determining the rate of growth of any unstable modes, and whether any stabilisation mechanisms have sufficient time to damp the growth. This means that the chromaticity of the beam now takes on a great importance, as this relates the betatron tune to the longitudinal motion. This leaves the option of changing the chromaticity of the beam to act as an additional stability mechanism.

Coupled Bunch Instabilities

In addition to single bunch instabilities, it is possible in machines where multiple bunches circulate, and possessing wakefields that do not damp in the spacing between bunches (typically caused by high Q resonant impedances), that the motion of the bunch centroids themselves may become coupled together, thus driving what are called coupled bunch instabilities (TCBI for the transverse plane, LCBI for the longitudinal plane).

This can be understood by imagining the bunch train as a possessing M bunches. This train will then have M possible modes of oscillation with a characteristic frequency of ω_M, which may be driven by an impedance at some frequency ω_0. If $\omega_0 \approx n\omega_M$ where n is an integer, then the wakefield due to the impedance may drive the oscillation either in a damped fashion (wakefield is out of phase with the oscillation of the mode) or an anti-damped fashion (wakefield is in phase with the oscillation of the mode). In the latter case, this driven oscillation may cause particle losses unless the oscillation is damped via an external mechanism, such as Landau damping or the use of a damper. This motion can occur in both the longitudinal and transverse planes of motion.

Chapter 3

Beam Based Measurements of Beam Coupling Impedance

3.1 Longitudinal Beam Impedance Measurements

3.1.1 Potential Well Distortion with Bunch Intensity

The equation for the longitudinal motion of a charged particle in an RF bucket can be linearised and solved to find the so called incoherent synchrotron frequency, that is it's oscillation in energy and phase, given by,

$$\omega_s = \frac{\omega_{RF}}{\beta} \left(\frac{\eta V_T cos\bar{\phi}}{2\phi E/e} \right)^{\frac{1}{2}} \tag{3.1}$$

where $\omega_{RF} = h\omega_0$ is the RF frequency, ω_0 is the revolution frequency, h is the harmonic number of the RF, $\eta = \alpha_c - \gamma^{-2}$ is the slip factor, $\alpha_c = \gamma_t^{-2}$ is the momentum compaction factor, γ_t is the transition energy gamma factor, $E = \gamma E_0$ is the total particle energy, E_0 is the rest eergy of the particle, $\bar{\phi}$ is the stable phase angle and V_T is the total voltage seen by the beam. For an empty bucket (i.e. no particles present) the voltage present is just that of the RF voltage V_{RF}, giving an associated synchrotron frequency ω_{s0}. We can subsequently see from Eqn. 3.1 that we have the ratio

$$V_T = V_{RF} \left(\frac{\omega_s}{\omega_{s0}} \right)^2 . \tag{3.2}$$

Additionally the bunch length L and the energy spread of the bunch $\Delta E / E$ can be shown to be related by

$$L = \frac{|\eta|\, c}{\beta \omega_s} \frac{\Delta E}{E} \tag{3.3}$$

within the linear approximation. If we assume that the emittance of the bunch is preserved (usually the case in a proton machine), i.e. $L\Delta E = constant$, Eqn. 3.2 leads to

$$L^2 \omega_s = L_0^2 \omega_{s0}. \tag{3.4}$$

The resulting induced voltage of the bunch depends heavily on the nature of the impedance on which the beam interacts with. In this case we shall illustrate the characteristics of the bunch lengthening with a simple inductive impedance ($Z = j\omega L$). More examples and detail can be found in Ref [B. zotter]. The voltage induced by a bunch with a parabolic line density through a purely inductive impedance is gives a resulting synchrotron frequency given by

$$\omega_s^2 = \omega_{s0}^2 \left[1 - \frac{C}{B^3} \frac{I_b}{hV_{RF}cos\bar\phi} \left(\left| \frac{Z}{n} \right| - \frac{gZ_0}{2\beta\gamma^2} \right) \right] \tag{3.5}$$

where $c = \frac{3}{\pi^2}$ is a constant dependent on the bunch profile, $B = \frac{L}{\pi R}$ is the bunching factor, given by the ratio of the bunch length to the machine circumference, I_b is the bunch current, $g = 1 + 2ln\left(\frac{b}{a}\right)$ is the direct space charge factor, b is the beam pipe radius, a is the beam radius and $Z_0 = 377\Omega$ is the impedance of free space.

If we consider an ultrarelativistic beam ($\gamma \to 1$), the space charge factor $g = 0$. Then, considering the value of $\bar\phi$ (i.e. whether the bunch is above transition $cos\bar\phi > 0$, or below transition $cos\bar\phi < 0$), the bunch length increases with the increased bunch current above transition, and decreases below transition. All variables other than Z/n may be measured directly using various instrumentation.

Generalisation of this method to a general complex impedance shows that it is the imaginary component of the longitudinal impedance that contributes the induced voltage, thus being the component of the impedance measured using this method.

3.1.2 Synchronous Phase Shift

As discussed in Section [ref beam induced heating], a particle circulating in circular accelerator losses energy due to interacting with impedances in the machine. If the particle is not undergoing acceleration, it can be seen that to keep the same energy, the particle must have a phase relative to the RF that ensures that the energy losses due to wakefields are equal to the energy gained during the traversal of the RF cavities, given by the equivalence of the energy gain by transit and the energy loss by traversal,

$$U = qeV sin\phi \tag{3.6}$$

where U is the total energy lost by a particle per turn, q is the unit charge, e is the electron charge, V is the RF voltage amplitude and ϕ is the synchronous phase. The total energy lost is the sum of all energy losses in the machine, given by

$$U = -e^2 N_b k \tag{3.7}$$

$$= -e^2 N_b \sum_n k_n \tag{3.8}$$

$$= -e^2 N_b \sum_n \Re e \left(Z_{\parallel,n} \left(\omega \right) \right) \left| \lambda \left(\omega \right) \right|^2 d\omega \tag{3.9}$$

where k_n is the kick factor of device n in the accelerator and $Z_{\parallel,n}$ is the longitudinalimpedance of device n. It can be seen that this allows the measurement of the impedance of the whole device. In addition where the movement of a device is permissible and can be carried out during operation (in collimation systems or insertion devices for example) it is possible to determine the impedance of specific devices by the change in their contribution to the total kick factor. Examples of this measuring method can be found in [ref energy loss of a single bunch in the sps, TDI measurements BS and J]

3.2   Transverse Beam Impedance Measurements

For a bunch interacting with a transverse impedance there are two commonly used methods of measuring the transverse impedance - the variance of the coherent betatron tune shift with bunch intensity and the change of growth/decay rate of head tail instabilities with the chromaticity of the beam [ref Sacherer, Zotter].

When a bunch is exposed to a tranverse inmpedance $Z_\perp$, it undergoes a complex frequency shift in in betatron frequency

$$\Delta\omega_\beta = \frac{N_p e c}{4\sqrt{\pi}\omega_\beta\left(E/e\right)T_0\sigma_t}i\left(Z_\perp\right)_{eff} \tag{3.10}$$

where N_p is the number of particles in the bunch, E is the energy, T_0 is the revolution frequency, $\sigma_t = \sigma_z/c$ is the bunch length, $\omega_\beta = 2\pi Q f_{rev}$ is the betatron frequency and $\left(Z_\perp\right)_{eff}$ is the effective transverse impedance. This is given by the impedance convolved with a weighting function h which is determined by the longitudinal bunch profile given by

$$\left(Z_\perp\right)_{eff}\left(\omega_\xi\right) = \int_{-\infty}^{\infty} Z_\perp\left(\omega\right)h_m\left(\omega - \omega_\xi\right)d\omega. \tag{3.11}$$

As an example, for the 0-mode coherent bunch oscillation and assuming a gaussian bunch profile the weighting function can be written as

$$h_0\left(\omega\right) = \frac{\sigma_t}{\sqrt{\pi}}e^{(\omega\sigma_t)^2}. \tag{3.12}$$

It can be seen from Eqn. 3.12 that the function is centred on ω_ξ which is dependent on the chromaticity ξ (see section[insert]) and the phase slip factor η as

$$\omega_\xi = \xi\frac{\omega_\beta}{\eta}. \tag{3.13}$$

Eqn 3.10 indicates that the imaginary component of the effective transverse impedance contributes to a real coherent tune shift, which the real component to an imaginary tune shift, visible as a growth/decay time in the oscillation. For a broadband impedance ($Q = 1$), at low frequencies it is possible to assume that $\Im m\left(Z_\perp\right) \approx const$. It then follows that

this is directly proportional to the real tune shift which can be obtained by measuring the coherent tune as a function of bunch intensity.

3.2.1 Tune shift change with bunch intensity

The real component of the solution to Eqn 3.10 can be related to the integer betatron tune by

$$\Delta Q = \frac{\Omega - \omega_\beta}{\omega_0} \approx \frac{1}{\omega_0} \frac{N_p e c^2}{4\sqrt{\pi}\omega_\beta (E/e) T_0 \sigma_t} \Im m (Z_\perp)_{eff}, \tag{3.14}$$

where Ω is the measured betatron frequency. It can easily be seen that by altering the bunch population the tune shift ΔQ can be measured also and subsequently the value for $\Im m (Z_\perp)$ can be obtained.

3.2.2 Growth time change with chromaticity

Similarly to the tune shift measurements, we consider the imaginary component of the solution. Similarly to a harmonic oscillator, the imaginary part of the solution denotes a damping time of the oscillation, τ, in this case given by

$$\frac{1}{\tau} = -T_0 \frac{N_p e c^2}{4\sqrt{\pi}\omega_\beta (E/e) T_0 \sigma_t} \Re e (Z_\perp)_{eff}. \tag{3.15}$$

$\Re e (Z_\perp)_{eff}$ is dependent only on the chromaticity ξ, being zero at $\xi = 0$ and different from zero for other values of chromaticity. Depending on whether the measurements are done above or below transition the produces either a damping for positive chromaticity above transition and growth below transition, and vice versa for negative chromaticity. Further details can be found in.

Chapter 4

Bench Top Measurements of Beam Coupling Impedance

Due to the sensitivity of the beam coupling impedance to the boundary conditions of the equipment used, it is necessary to utilise different measurement techniques to fully analyse the impedance of accelerator structures.

4.1   Low Q-factor Impedances

For structures that are expected to contain mostly low Q-resonances (i.e. resistive wall impedance) it is appropriate to use the coaxial wire method[ref], sometimes also called the stretched wire method. This method relies on the similarity of the electromagetic field profile due to an ultrarelativistic charged particle and that of a short electrical pulse sent along a coaxial wire.

An moving charged particle produces an electromagnetic field in a arc transverse to its direction of motion, where the angle of the arc opening is proportinal to the relativistic factor of the particle γ. For an ultrarelativistic particle ($\gamma \leftarrow \infty$), the field becomes entirely perpendicular to the direction of motion. If we place a conductive wire along the same path we would expect the charged particle to take (in most cases this is well represented by a straight wire), a short electrical pulse sent along this wire would propogate in

Figure 4.1: Comparison of the electromagnetic field profile of a moving charged particle and a short time pulse propogating along a coaxial wire.

Figure 4.2: Experimental setup for a measurement of the beam coupling impedance using the classical coaxial wire method

the TEM (transverse electrical and magnetic field) mode, producing a field profile similar to that emitted by the ultrarelativistic charged particle (see. Fig. 4.1)

4.1.1 Classical Coaxial Wire Method

The classical coaxial wire method, first proposed by V. Vaccarro in 1990 [ref], is a transmission method that measures the complex transmission coefficient of a DUT (Device Under Test) made up of the equipment whose impedance is to be measured and a coaxial wire passing through it.

The experimental setup is as shown in Fig. 4.2. Firstly the external circuit (i.e. everything not the DUT) is matched to the characteristic impedance of the coaxial line inside the DUT. This is done by measuring the reflection coefficient Γ for the setup with only one port connected to the DUT and the other end terminated by an open connection. Knowing the characteristic impedance of the VNA and associated cables (typically $Z_0 = 50\Omega$), we can easily calculate the characteristic impedance, Z_c, from the relation,

$$\Gamma = \frac{Z_c - Z_0}{Z_c + Z_0}.$$ (4.1)

We then electrically match the characteristic impedance by adding resistors in series just before the DUT to resistively match the characteristic impedance of the VNA to that of the DUT. It is possible to use physical matching also using transition cones but these are costly, time consuming to construct and require new cones for each piecof equipment measured. And as can be seen in Fig. 4.3, matching with a resistor is highly effective at removing the presence of reflections in coaxial measurements.

The value that we wish to measure to evaluate the beam coupling impedance of a device are the scattering parameters of the resulting circuit, in particular S_{21}, the normalised

Figure 4.3: An example of a reflection measurement made with and without a matching resistor. The faded line is the measurement without matching, the bold line that with. The reduction in the reflection can be seen.

transmission parameter through the DUT. S_{21} is calculated by taking the measured transmission parameter $S_{21,DUT}$ and dividing it by the transmission parameter through a reference line of the same physical length as the DUT,

$$S_{21} = \frac{S_{21,DUT}}{S_{21,REF}} \tag{4.2}$$

.

The effect of this is to correct the measured phase change in the DUT to be that only caused by the imaginary component of the beam coupling impedance.

There are subsequently a number of ways to evaluate the beam coupling impedance of the DUT depending on it's expected properties. For devices that are expected to have a either a small impedance, or those that are physically very short in length, it is possible to use the so called lumped impedance formula[ref];

$$Z = 2Z_c \frac{1 - S_{21}}{S_{21}} \tag{4.3}$$

.

For distributed impedances, it is suitable to use the so called log formula (called so due to attenuation causing a log function to appear in the evaluation),

$$Z = -2Z_c ln\left(S_{21}\right) \tag{4.4}$$

.

For long components or measurements at very high frequencies there exists the improved log formula. This takes into account more completely the electrical length of the device, given by

$$Z = -2Z_c ln\left(S_{21}\right)\left(1 + j\frac{ln\left(S_{21}\right)}{2\Theta}\right) \tag{4.5}$$

72

where $\Theta = 2\pi \frac{L}{\lambda}$ is the normalised electrical length of the device, L the length of the device, λ the wavelength of the frequency of measurement. It is possible to see that the lumped impedance formula can be used when $\Theta \leq 1$, and the improved log formula becomes useful for $\Theta \geq 5$[erk's paper].

4.1.2 Resonator Coaxial Wire Method

An alternative method for measuring the beam coupling impedance is by using the so called resonator method. The setup for this method is similar to that of the classical coaxial wire method, except that the matching resistor network between the VNA and DUT is replaced by a weak capacitive coupling ($S_{11} < 0.5dB$) at both ends of the DUT. This then produces a structure which resonates at frequencies where the wavelength corresponds to the classical closed structure form,

$$\lambda = \frac{2L}{n} \tag{4.6}$$

where λ is the wavelength of the resonance, n the harmonic of the resonance and L the length of the device.

The resonant method enables accurate measurement of the transmission losses due to the real longitudinal impedance. Additional advantages are that no matching is required, and a large number of mechanical uncertainties (electrical connections, consistency of calibration) can be avoided. However it can be seen that the frequency resolution is limited due to the length of the DUT so the method is not recommended as the only measurement method for structures expected to contain high-Q, narrowband resonances. It can however be used to corroborate the results obtained using the classical method.

For each resonancce peak, the loaded Q-factor and the frequency of the resonance are measured. For a weak coupling at both ends of the DUT, we can write the coupling coefficient k as

$$k = \frac{|S_{21}|}{1 - |S_{21}|}. \tag{4.7}$$

Figure 4.4: An example of the resonance pattern seen whilst performing measurements using the resonant method. Each peak corresponds to one data point in the final measurements.

The difference between the unloaded Q-factor, Q_0 , and the loaded Q-factor, Q_L, is a function of k. We can get an approximate correction by using the formula

$$Q_0 = Q_L \left(1 + k\right).$$ (4.8)

Subsequently the measured line attenuation (in Np/m) is then calculated

$$\alpha_m = \frac{\pi}{\lambda Q_0}.$$ (4.9)

Note that this attenuation includes both that from the beam coupling impedance due to the finite resistance of the wire material. We can estimate the attenuation due to the wire material as

$$\alpha_w = \sqrt{\pi \rho_w \epsilon f} \frac{1}{d \ln D/d}$$ (4.10)

where ρ_w is the wire resistivity, ϵ the permitivitty, f the frequency, d the diameter of the inner conductor and D the diameter of the outer conductor. At very low frequencies the finite skin depth of the inner conductor would also have to be taken into account. Using the corrected attentuation $\alpha = \alpha_m - \alpha_w$, the real longitudinal impedance per unit length can be found to be

$$\Re e \left\{Z\right\} = 2Z_c \alpha$$ (4.11)

To calculate the imaginary impedance using the resonant method involves a more involved calculation. In particular it is necessary to carry out measurements using the resonant method on a reference pipe of the same physical length to the DUT, either using physical measurements or a simulated measurement.

If we consider the complex impedance of the two measurements, Z_{DUT} for the DUT and Z_{REF} for a perfectly conducting reference pipe, we can simplify them as

$$Z_{DUT} = R + jX_1 = Z_1 e^{j\phi} \tag{4.12}$$

$$Z_{REF} = jX_2 = Z_2 e^{j.0} \tag{4.13}$$

where R is the resistive component of the DUT impedance, $X_{1/2}$ the imaginary component of the impedance (DUT and reference pipe respectively), ϕ is the angle of DUT impedance projected onto a complex plane and $Z_2 = \sqrt{R^2 + X^2}$. If we consider a measured value depedent on the impedance, for example the transmission parameter S_{21} at a resonance peak, we have the following relations

$$S_{21}^{DUT} = S_0 e^{j(\omega_1 t + \phi)} \tag{4.14}$$

$$S_{21}^{REF} = S_0 e^{k(\omega_2 t)} \tag{4.15}$$

where S_0 is some normalised scalar, $\omega_{1/2}$ is the frequency of the resonance and $t = \frac{L}{c}$. Thus for a pair of corresponding peaks from resonance measurements for which we have measured ω_1 and ω_2 we can equate $S_{21}^{DUT} = S_{21}^{REF}$ and thus show

$$\phi = t\left(\omega_2 - \omega_1\right). \tag{4.16}$$

Subsequently we can see that

$$X = Z_{DUT}sin\phi = R\frac{sin\phi}{cos\phi} = Rtan\phi \tag{4.17}$$

where $R = \Re e(Z)$.

4.1.3 Transverse Impedance Measurements

The above methods give a general impression of how to carry out coaxial wire measurements of the impedance of accelerator components. Directly applied as described they allow the measurement of the longitudinal impedance of a DUT. However, from a beam stability point of view it is often more interesting to look at the transverse imedance of

a device. In particular it would be useful to have a method of determining the vertical/horizontal dipolar (or driving) impedance and the vertical/horizontal quadrupolar (detuning) impedance of any device. In this section we describe how do this for structures with top/bottom, left/right symmetry and then generalising to asymmetric structures, with illustration from simple examples evaluated using simulations.

To allow a complete explanation of how to verify the methods of measuring transverse impedances, let us first consider the general form of the m-th order ($m = 0, 1, 2, ...$) longitudinal beam coupling impedance, given by [ref]

$$\bar{Z}_m = \frac{-1}{I^2} \int dV \bar{\mathbf{E}}_\mathbf{m} . \bar{\mathbf{J}}_\mathbf{m}^* \qquad (4.18)$$

where $\bar{J}_m$ is the current density of the source. For a beam propogating along the z-axis with an offset a and moment $cos\,(m\theta)$,

$$\bar{\mathbf{J}}_\mathbf{m} = \frac{I}{\pi a^{m+1} (1 + \delta_{m0})} \delta\,(r - a)\,cos\,(m\theta)\,exp\,(j\,(\omega t - kz))\,\mathbf{e}_\mathbf{z}. \qquad (4.19)$$

The electromagnetic field associated with a given current source $\bar{\mathbf{J}}_\mathbf{m}$ is $\left(\bar{\mathbf{E}}_\mathbf{m}, \bar{\mathbf{H}}_\mathbf{m} \right)$.

What can be seen is that any different azimuthal components of the m-th field of order n (i.e. $sin\,(n\theta)$ and $cos\,(n\theta)$ terms) are neglected in this treatment. To allow the treatment of coupling between different azimuthal orders we can define a longitudinal beam coupling impedance $Z_{m,n}$ (where $m, n = 0, \pm 1, \pm 2, ...$)

$$Z_{m,n} = \frac{-1}{I^2} \int dV \mathbf{E}_\mathbf{m} . \mathbf{J}_\mathbf{n}^* \qquad (4.20)$$

where

$$\mathbf{J}_\mathbf{m} = \frac{I}{\pi a^{|m|+1}} \delta\,(r - a)\,exp\,(jm\theta)\,exp\,(j\,(\omega t - kz))\,\mathbf{e}_\mathbf{z}. \qquad (4.21)$$

Importantly, this allows us to see that

$$\bar{\mathbf{J}}_\mathbf{0} = \mathbf{J}_\mathbf{0}$$

$$\bar{\mathbf{J}}_\mathbf{m} = \mathbf{J}_\mathbf{m} + \mathbf{J}_{-\mathbf{m}}. \qquad (4.22)$$

Figure 4.5: Measurement setup for measurements of the dipolar beam coupling impedance using the two wire setup for the classical coaxial wire method.

From here we use the principle of superposition for electromagnetic fields, and thus can derive

$$\bar{Z}_0 = Z_0 \tag{4.23}$$

$$\bar{Z}_x = \bar{Z}_1 = Z_{1,1} + Z_{1,-1} + Z_{-1,1} + Z_{-1,-1} = kZ_x^{dip} \tag{4.24}$$

$$\bar{Z}_x = \bar{Z}_1(\text{cos replaced with sin}) = Z_{1,1} - Z_{1,-1} - Z_{-1,1} + Z_{-1,-1} = kZ_y^{dip} \tag{4.25}$$

$$\bar{Z}_m = Z_{m,m} + Z_{m,-m} + Z_{-m,m} + Z_{-m,-m}, m = 1, 2, ... \tag{4.26}$$

From this start we will apply this two both two wire measurements and to displaced single wire measurements.

Two Wire Measurements

It is possible to directly measure the dipolar impedance of a device through the use of a two wire coaxial method. The measurement setup is identical to that of the single wire method, except that two wires, seperated by distance Δ, are placed in the device, and a $180°$ hybrid is place between the wires and the VNA at both ends of the device. This setup is illustrated in Fig. **??**

The measurements are done in the same way as described in the previous sections for either the classical transmission method or the resonator method. By using two wires each carrying a signal 180° out of phase with one another we produce a field pattern similar to a dipole and thus measure the dipole impedance in either the horizontal or vertical plane depending on the orientation of the two wires.

What is directly measured is the longitudinal impedance of just the dipole impedance, as is to be expected from the Panofsky-Wenzel theorem (see Chap. **??** for further explanation).

For two wire placed as positions $x = \pm a$, the current density is given by [ref]

$$J = I \left(\delta \left(x - a \right) - \delta \left(x + a \right) \right) \delta(y) exp \left(j \left(\omega t - kz \right) \right)$$

$$= \frac{I}{\pi a} \sum_{m=-\infty}^{\infty} exp \left(j \left(2m + 1 \right) \theta \right) exp \left(j \left(\omega t - kz \right) \right)$$

$$= 2 \sum_{m=-\infty}^{\infty} a^{|2m+1|} J_{2m+1}. \tag{4.27}$$

The impedance is then

$$Z = -\frac{1}{I^2} \int dV \left(2 \sum_{m=-\infty}^{\infty} a^{|2m+1|} E_{2m+1} \right) \left(2 \sum_{n=-\infty}^{\infty} a^{|2n+1|} J_{2n+1}^* \right)$$

$$= 4 \sum_{m,n} a^{|2m+1|+|2n+1|} Z_{2m+1,2n+1}$$

$$= (2a)^2 \left(Z_{1,1} + Z_{-1,1} + Z_{1,-1} + Z_{-1,-1} \right) + O(a^4)$$

$$= (2a)^2 \bar{Z}_x + O(a^4). \tag{4.28}$$

Again using the Panofsky-Wenzel theorem we can deduce that the transverse dipolar impedance $Z_{x/y}^{dip}$ is given by

$$Z_{x/y}^{dip} = \frac{\bar{Z}_{x/y}}{k} = \frac{c}{\omega} \frac{Z}{\Delta^2} \tag{4.29}$$

where $\Delta = 2a$ and Z is the measured complex impedance.

Structures with Top/Bottom, Left/Right Symmetry

If we consider a source particle at at $x_1 = a_1 cos\theta_1, y_1 = a_1 sin\theta_1$ and a test particle at $x_2 = a_2 cos\theta_2, y_2 = a_2 sin\theta_2$, the source current density is

$$J_z = I\delta \left(x - x_1 \right) \delta \left(y - y_1 \right) exp \left(k \left(\omega t - kz \right) \right)$$

$$= \sum_{m=-\infty}^{\infty} a_1^{|m|} exp \left(-jm\theta_1 \right) J_m \tag{4.30}$$

The impedance would therefore be

$$Z = \frac{-1}{I^2} \int dV \left(\sum_{m=-\infty}^{\infty} a_1^{|m|} exp \left(jm\theta_1 \right) E_m \right) \left(\sum_{n=-\infty}^{\infty} a_1^{|n|} exp \left(jn\theta_2 \right) J_n^* \right)$$

$$= \sum_{m,n=-\infty}^{\infty} a_1^{|m|} a_2^{|n|} exp \left(-jm\theta_1 \right) exp \left(-jn\theta_2 \right) Z_{m,n}$$

$$= Z_{0,0} + \left(x_1 - jy_1 \right) Z_{1,0} + \left(x_1 + jy_1 \right) Z_{-1,0} + \left(x_2 + jy_2 \right) Z_{0,1} + \left(x_2 - jy_2 \right) Z_{0,-1}$$

$$+ \left(x_1 - jy_1 \right)^2 Z_{2,0} + \left(x_1 - jy_1 \right) \left(x_2 - jy_2 \right) Z_{1,-1} + \left(x_2 - jy_2 \right) Z_{0,-2}$$

$$+ \left(x_1 - jy_1 \right) \left(x_2 + jy_2 \right) Z_{1,1} + \left(x_1 + jy_1 \right) \left(x_2 - jy_2 \right) Z_{-1,-1}$$

$$+ \left(x_1 + jy_1 \right)^2 Z_{-2,0} + \left(x_1 + jy_1 \right) \left(x_2 - jy_2 \right) Z_{-1,1} + \left(x_2 - jy_2 \right)^2 Z_{0,2}$$

$$+ O \left(\left(x_1, y_1, x_2, y_2 \right)^3 \right). \tag{4.31}$$

By applying Panofsky-Wenzel we see

$$kZ_x = \frac{\partial Z}{\partial x_2} = Z_{0,1} + Z_{0,-1} + \left(x_1 - jy_1 \right) Z_{1,-1} + 2 \left(x_2 - jy_2 \right) Z_{0,-2}$$

$$+ \left(x_1 - jy_1 \right) Z_{1,1} + \left(x_1 + jy_1 \right) Z_{-1,-1} + \left(x_1 + jy_1 \right) Z_{-1,1} + 2 \left(x_2 + jy_2 \right) Z_{0,2}$$

$$+ O \left(\left(x_1, y_1, x_2, y_2 \right)^2 \right)$$

$$= Z_{0,1} + Z_{0,-1} + x_1 \bar{Z}_x + jy_1 \left(-Z_{1,-1} - Z_{1,1} + Z_{-1,-1} + Z_{-1,1} \right)$$

$$+ x_2 \left(2Z_{0,-2} + 2Z_{0,2} \right) + jy_2 \left(-2Z_{0,-2} + 2Z_{0,2} \right) + O \left(\left(x_1, y_1, x_2, y_2 \right)^2 \right)$$

$$\tag{4.32}$$

$$kZ_y = \frac{\partial Z}{\partial y_2} = jZ_{0,1} - jZ_{0,-1} - j \left(x_1 - jy_1 \right) Z_{1,-1} - 2j \left(x_2 - jy_2 \right) Z_{0,-2}$$

$$+ j \left(x_1 - jy_1 \right) Z_{1,1} - j \left(x_1 + jy_1 \right) Z_{-1,-1} + j \left(x_1 + jy_1 \right) Z_{-1,1} + 2j \left(x_2 + jy_2 \right) Z_{0,2}$$

$$+ O \left(\left(x_1, y_1, x_2, y_2 \right)^2 \right)$$

$$= j \left(Z_{0,1} - Z_{0,-1} \right) + y_1 \bar{Z}_y + jx_1 \left(-Z_{1,-1} + Z_{1,1} + Z_{-1,-1} + Z_{-1,1} \right)$$

$$+ y_2 \left(-2Z_{0,-2} - 2Z_{0,2} \right) + jx_2 \left(-2Z_{0,-2} + 2Z_{0,2} \right) + O \left(\left(x_1, y_1, x_2, y_2 \right)^2 \right). $$

$$\tag{4.33}$$

Two properties to note for later use are that

$$\mathbf{J}_{-m}\left(\omega\right) = \mathbf{J}_{m}^{*}\left(-\omega\right) \tag{4.34}$$

$$Z_{-m,-n}\left(\omega\right) = Z_{m,n}^{*}\left(-\omega\right). \tag{4.35}$$

If we now assume a single wire rather than a source and test particle, such that $x_1 = x_2 = x_0, y_1 = y_2 = y_0$. This gives a source current density

$$
\begin{aligned}
J &= I\delta\left(x - x_0\right)\delta\left(y - y_0\right)exp\left(j\left(\omega t - kz\right)\right) \\
&= \frac{I}{2\pi a}\delta\left(r - a\right)\sum_{m=-\infty}^{\infty} exp\left(jm\left(\theta - \theta_0\right)\right)exp\left(jm\left(\theta - \theta_0\right)\right)exp\left(j\left(\omega t - kz\right)\right) \\
&= \sum_{m=-\infty}^{\infty} a^{|m|}exp\left(-jm\theta_0\right)J_m. \tag{4.36}
\end{aligned}
$$

We can then define $x_0 = a\cos\theta_0, y_0 = a\sin\theta_0$. Entering this into Eqn. 4.31 gives

$$
\begin{aligned}
Z =\quad & Z_{0,0} + \left(x_0 - jy_0\right)Z_{1,0} + \left(x_0 + jy_0\right)Z_{-1,0} + \left(x_0 + jy_0\right)Z_{0,1} \\
& + \left(x_0 - jy_0\right)Z_{0,-1} + \left(x_0 - jy_0\right)^2 Z_{2,0} + \left(x_0 - jy_0\right)^2 Z_{1,-1} + \left(x_0 - jy_0\right)^2 Z_{0,-2} \\
& + \left(x_0 - jy_0\right)\left(x_0 + jy_0\right)Z_{1,1} + \left(x_0 + jy_0\right)\left(x_0 - jy_0\right)Z_{-1,-1} + \left(x_0 + jy_0\right)^2 Z_{-2,0} \\
& + \left(x_0 + jy_0\right)^2 Z_{-1,1} + \left(x_0 + jy_0\right)^2 Z_{0,2} + O\left(\left(x_0, y_0\right)^2\right) \\
=\quad & Z_{0,0} + x_0\left(Z_{1,0} + Z_{-1,0} + Z_{0,1} + Z_{0,-1}\right) + jy_0\left(-Z_{-1,0} + Z_{-1,0} + Z_{0,1} - Z_{0,-1}\right) \\
& + x_0^2\left(Z_{1,-1} + Z_{1,1} + Z_{-1,-1} + Z_{-1,1} + Z_{2,0} + Z_{0,-2} + Z_{0,2} + Z_{-2,0}\right) \\
& + y_0^2\left(-Z_{1,-1} + Z_{1,1} + Z_{-1,-1} - Z_{-1,1} - Z_{2,0} - Z_{0,-2} - Z_{0,2} - Z_{-2,0}\right) \\
& + 2jx_0y_0\left(-Z_{2,0} - Z_{0,-2} + Z_{-2,0} + Z_{0,2} + Z_{-1,1} - Z_{1,-1}\right) \\
=\quad & Z_{0,0} + x_0\left(Z_{1,0} + Z_{-1,0} + Z_{0,1} + Z_{0,-1}\right) + jy_0\left(-Z_{-1,0} + Z_{-1,0} + Z_{0,1} - Z_{0,-1}\right) \\
& + x_0^2\left(\bar{Z}_x + Z_{2,0} + Z_{0,-2} + Z_{0,2} + Z_{-2,0}\right) \\
& + y_0^2\left(\bar{Z}_y - Z_{2,0} - Z_{0,-2} - Z_{0,2} - Z_{-2,0}\right) \\
& + 2jx_0y_0\left(-Z_{2,0} - Z_{0,-2} + Z_{-2,0} + Z_{0,2} + Z_{-1,1} - Z_{1,-1}\right). \tag{4.37}
\end{aligned}
$$

It can then be seen that if measurements are made with $x_0 = 0$ and take different values of y_0 that one obtains data with a parabolic fit in the y_0 axis. Be fitting a curve to this we obtain constant (equal to the longitudinal impedance), linear and quadratic terms. Doing the same for $y_0 = 0$ allows us to derive two quadratic terms

$$Z_x^\perp = \left(\bar{Z}_x + kZ_{quad}\right)\frac{1}{k} = Z_x^{dip} + kZ_{quad} \tag{4.38}$$

$$Z_y^\perp = \left(\bar{Z}_y - kZ_{quad}\right)\frac{1}{k} = Z_y^{dip} - kZ_{quad} \tag{4.39}$$

$$\tag{4.40}$$

where $Z_{quad} = \frac{1}{k}\left(Z_{0,2} + Z_{2,0} + Z_{0,-2} + Z_{-2,0}\right) = \frac{2}{k}\left(Z_{0,2} + Z_{0,-2}\right)$, representing the impedance due to the displacement of the test particle in an accelerator. As we can measure $\bar{Z}_{x/y}$ independently using the two wire method we can thus indepedently measure Z_{quad} using a displaced single wire scan in both the x- and y-planes.

It can also be seen that

$$Z_x^\perp + Z_y^\perp = \frac{1}{k}\left(\bar{Z}_x + \bar{Z}_y\right) = Z_x^{dip} + Z_y^{dip} \tag{4.41}$$

where $\bar{Z}_{x/y}$ can be measured independently which gives a method of obtaining confidence in the wire measurements.

Asymmetric Structures

If Eqn. 4.37 is transformed from (x, y) coordinates to (a, θ), the result is

$$Z = Z_{0,0} + a\left[cos\theta\left(Z_{-1,0} + Z_{0,1}\right) + jsin\theta\left(Z_{-1,0} + Z_{0,1}\right)cos\theta\left(Z_{1,0} + Z_{0,-1}\right) - jsin\theta\left(Z_{1,0} + Z_{0,-1}\right)\right]$$

$$+ a^2\left[cos^2\left(Z_{1,1} + Z_{-1,-1}\right) + sin^2\left(Z_{1,1} + Z_{-1,-1}\right)\right]$$

$$+ a^2\left[cos^2\left(Z_{2,0} + Z_{0,-2} + Z_{1,-1}\right) + 2jsin\theta cos\theta\left(Z_{2,0} + Z_{0,-2} + Z_{1,-1}\right)\right]$$

$$- a^2\left[sin^2\left(Z_{2,0} + Z_{0,-2} + Z_{1,-1}\right)\right]$$

$$+ a^2\left[cos^2\left(Z_{-2,0} + Z_{0,2} + Z_{-1,1}\right) + 2jsin\theta cos\theta\left(Z_{-2,0} + Z_{0,2} + Z_{-1,1}\right)\right]$$

$$+ a^2\left[sin^2\left(Z_{-2,0} + Z_{0,2} + Z_{-1,1}\right)\right]. \tag{4.42}$$

Grouping like terms this becomes

$$Z = Z_{0,0} + a\left[e^{-j\theta}\left(Z_{-1,0} + Z_{0,1}\right) + e^{j\theta}\left(Z_{1,0} + Z_{-0,1}\right)\right]$$

$$+ a^2\left[\left(Z_{1,1} + Z_{-1,-1}\right) + e^{-2j\theta}\left(Z_{2,0} + Z_{0,-2} + Z_{1,-1}\right) + e^{2j\theta}\left(Z_{-2,0} + Z_{0,2} + Z_{-1,1}\right)\right]$$

$$= A_1 + ae^{-j\theta}A_2 + ae^{-j\theta}A_3 + a^2e^{-2j\theta}A_4 + a^2e^{2j\theta}A_5 + a^2A_6 \qquad (4.43)$$

where $A_1 = Z_{0,0}$, $A_2 = Z_{0,1} + Z_{-1,0}$, $A_3 = Z_{0,-1} + Z_{1,0}$, $A_4 = Z_{0,2} + Z_{-1,1} + Z_{-2,0}$, $A_5 = Z_{2,0} + Z_{1,-1} + Z_{0,-2}$ and $A_6 = Z_{1,1} + Z_{-1,-1}$. Taking the earlier definition of Z_{quad} it can be deduced that

$$Z_{quad} = \left(A_4 + A_5 + A_6 - \bar{Z}_x\right)\frac{1}{k} = \frac{A_4 + A_5 + A_6}{k} - Z_x^{dip} \qquad (4.44)$$

$$= \left(A_4 + A_5 - \frac{\bar{Z}_x - \bar{Z}_y}{2}\right)\frac{1}{k} = \frac{A_4 + A_5}{k} - \frac{Z_x^{dip} - Z_y^{dip}}{2}. \qquad (4.45)$$

Consideration of Eqn. 4.43 lets it be seen that

$$A_4 + A_5 + A_6 = \frac{Z(a,0) + Z(a,\pi) - 2Z(0,0)}{2a^2} \qquad (4.46)$$

$$A_4 + A_5 = \frac{Z(a,0) + Z(a,\pi) - Z\left(a,\frac{\pi}{2}\right) - Z\left(a,\frac{3\pi}{2}\right)}{2a^2} \qquad (4.47)$$

4.1.4 Measurements on Example Geometries

In this section shall be presented a number of example analyses of coaxial wire measurements done on geometries exhibiting top/bottom, left/right symmetry and an asymmetric structure. This permits a step-by-step guide to analysis of the wire measurements, which may not be immediately clear from the mathematical introduction. These simulations are simulated using both Ansoft HFSS and Maxwell using a driven modal solution.

The simulations with HFSS are carried out in the following manner: the measurement system is simulated by placing waveguide ports at either end of the geometry with a conducting cylinder placed as the inner conductor of the coaxial system. The transmission parameters are then acquired as a result of the simulations. The wire may then be

displaced as neccessary for the displaced single wire measurements. For two wire measurements a quarter geometry may be simulated, using suitable boundary conditions on the quarter geometry.

Maxwell is a frequency domain code optimised for low frequencies (less thans 10s of MHz). It does not permit the use of waveguide ports, however does allow the definition of current segments with phase changes between them. By considering the current (either a single current segment to simulate a single wire, or two current carrying segments 180° out of phase for two wires) to be the equivalent of a beam current, and assuming the inclusion of the current carrying component is a negligible perturbation to the geometry, the impedance can be found by summing the power loss in the system. This can be seen to be equivalent to the beam induced heating experienced by a beam interacting with an impedance.

This can be thought of by comparing the system to a homogenous transmission line[cite Kroyer]. The power P of a wave travelling along the line is given by

$$P = P_0 e^{-2\alpha z} \tag{4.48}$$

where P_0 is the power at the beginning of the transmission line, α is the attenuation coefficient and z the distance along the line. By differentiation it can be seen that

$$\alpha = -\frac{1}{2P}\frac{dP}{dz} \approx \frac{1}{2P}\frac{\delta P}{\delta z} \tag{4.49}$$

where δP is the power lost over the short distance δz. The transmission parameter of a line S_{21} is given by

$$S_{21} = e^{-\alpha \delta z}. \tag{4.50}$$

If the impedance is evaluated using the log formula ($Z = Z_c ln S_{21}$), it can be seen that the real impedance is subsequently given by

$$\Re e\left(Z\right) = Z_c \frac{2\delta P}{P}. \tag{4.51}$$

(a)

(b)

Figure 4.6: The geometries used for coaxial wire measurement simulations. For the geometry with top/bottom, left/right symmetry we use the Tsutsui model (4.6(a)) using two parallel plates. For the asymmetric structure we use the Zannini-model for a c-core ferrite kicker magnet (4.6(b)), which generates a constant term and a noticeable asymmetric term.

Figure 4.7: The complex permeability of 4A4 ferrite. Taken from the model in [cite]

Assuming a peak current I_0 on the wire, $P = I_0^2 Z_c / 2$, which gives

$$\Re e\left(Z\right) = \frac{2\delta P}{I_0^2}. \tag{4.52}$$

To acquire the transverse impedance for two wire simulations it is simply neccesary to normalise by the wavenumber $k = \omega/c$ and the seperation of the wire Δ

$$Z_{dip} = \frac{c}{\omega \Delta^2} \frac{2\delta P}{I_0^2}. \tag{4.53}$$

Structure with Top/Bottom, Left/Rght Symmetry

For the structure exhibiting top/bottom, left/right symmetry we use the Tsutsui model of two parallel plates as shown in Fig. **??**. We use this due to the model allowing the prediction of the longitudinal, dipolar and quadrupolar impedances for a wide variety of materials and frequency ranges [cite Tsutsui longitudinal, transverse]. For these simulations a short segment of a Tsutsui geometry is simulated using two different materials, in this case graphite, to represent a structure with a poor conductivity ($\sigma_{graphite} = 7^4 Sm^{-1}$), and 4A4 ferrite, to represent a magnetically lossy material (In this case, $\epsilon_r = 10$, $\sigma_{4A4} = 10^{-6} Sm^{-1}$ (a mild conductivity is applied to prevent static build up in ferrite components in accelerators), and $\mu_r = \mu' + j\mu''$, shown in Fig. 4.1.4.). In both cases the following dimensions are used: $a = 25mm$, $b = 5mm$, $d = 5mm$. A structure 150mm in length is used to reduce numerical artefacts.
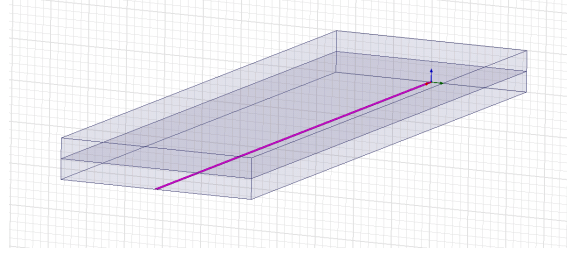
Figure 4.8: An example of the simulation model used for coaxial wire simulations. In this case a displaced single wire between two ferrite plates. The wire is highlighted in purple.

Two Parallel Ferrite Plates

For the simulations of two parallel ferrite plates the following parameters were used; for the displaced single wire measurements a wire of 0.3mm in radius is used, and the following displacement used to acquire the total transverse terms:

1. In the horizontal axis - displaced between -6mm to +6mm at intervals of 2mm

2. In the vertical axis - displaced between -4mm to +4mm at intervals of 2mm.

For the two wire simulations, two wires of radius 0.3mm are used, with a seperation of 4mm in the x-dimension, and 3mm in the y-dimension. 4 simulation configurations are used described below:

1. an adaptive mesh generation set to a convergence criteria of S_{21} diverging by less than 0.005 between two subsequent solutions, at an adaptive frequency of 20MHz solving to a second order basis. A discrete frequency sweep is then carried out in the range 1-10MHz at 1MHz intervals.

2. an adaptive mesh generation set to a convergence criteria of S_{21} diverging by less than 0.005 between two subsequent solutions, at an adaptive frequency of 200MHz solving to a second order basi. A discrete frequency sweep is then carried out in the range 10-100MHz at 10MHz intervals.

3. an adaptive mesh generation set to a convergence criteria of S_{21} diverging by less than 0.005 between two subsequent solutions, at an adaptive frequency of 2GHz

Figure 4.9: The longitudinal impedance of two parallel ferrite plates measured using a longitudinal coaxial wire. Presented are is the impedance as measured in the horizontal plane (4.9(a)) and in the vertical plane 4.9(b).

solving to a second order basis. A discrete frequency sweep is then carried out in the range 100MHz-1GHz at 100MHz intervals.

4. an adaptive mesh generation set to a convergence criteria of S_{21} diverging by less than 0.005 between two subsequent solutions, at an adaptive frequency of 10GHz solving to a second order basis. A discrete frequency sweep is then carried out in the range 1-10GHz at 1GHz intervals.

These parameters are used to benefit from an appropriate mesh count for the given frequency range, thus increasing simulation speed by not using a high density mesh at frequencies where no benefits would be gained.

The longitudinal impedance is as measured by taking the constant term for a series of displaced wire measurements in both the vertical and horizontal planes is shown in Fig. 4.1.4. It can be seen that in the frequency range below 100MHz the agreement between the coaxial wire results and the analytical results is very good in both the vertical and horizontal plane. Above 100MHz the agreement for the real components is very good for both results, however the imaginary component in the vertical plane displays some substantial disagreement. This is likely due to the high mesh density required to correctly evaluate the phase change along the length of the simulated structure. A higher mesh

86
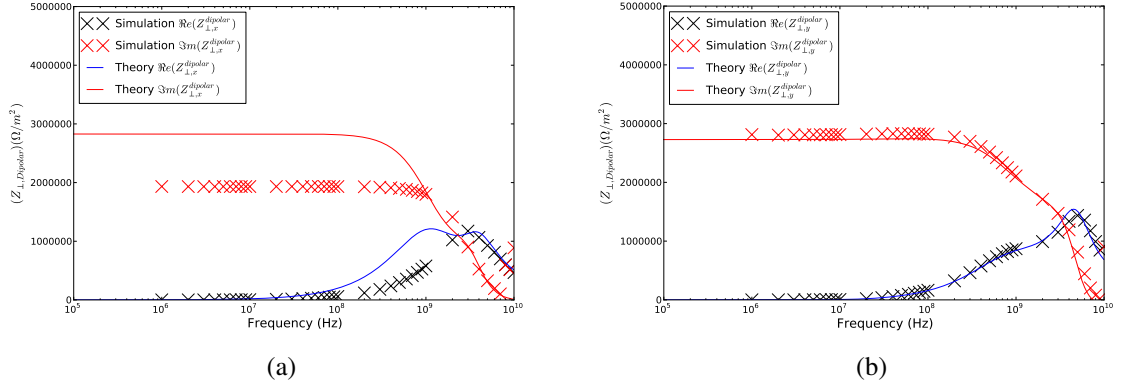
Figure 4.10: The dipolar impedance of two parallel ferrite plates measured using two longitudinal coaxial wires. Presented are is the impedance as measured in the horizontal plane (4.10(a)) and in the vertical plane 4.10(b).
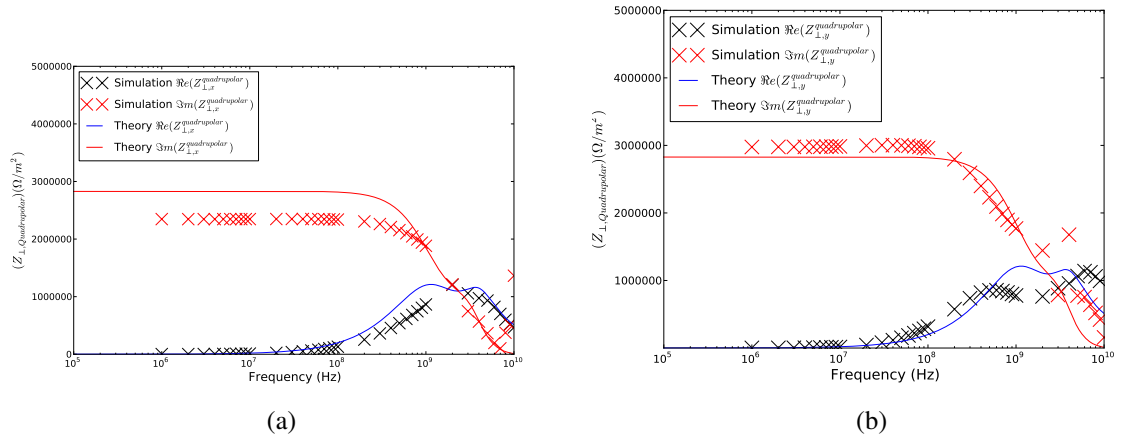
Figure 4.11: The quadrupolar impedance of two parallel ferrite plates measured using a combination of displaced single wire measurements and two wire mesurements. Presented are is the impedance as measured in the horizontal plane (4.11(a)) and in the vertical plane 4.11(b).

density may correct this, however limits of computational resource make this unfeasible for these results.

The agreement between the simulations of the vertical dipolar impedance and the theoretical model is excellent across all frequencies for both the real and imaginary components. The agreement below 100MHz and above 1GHz is very good for the horizontal dipolar, with some divergence in the constant term of the imaginary impedance. The key difference is the failure of the coaxial method to resolve one of the peaks in the real impedance. The results for the dipolar impedance are shown in Fig. 4.1.4.

The results for the quadrupolar impedance are shown in Fig. 4.1.4. The vertical simulations agree well with the theory, correctly identifying the two peaks in the quadrupolar impedance. The agreement for the horizontal simulations with theory is less good. This can be explained as the derivation of the horizontal quadrupolar is highly dependent on the quality of the horizontal dipolar impedance results due to them cancelling each other to form the total transverse impedance. As the horizontal dipolar impedance does not resolve the the subpeaks neither does the horizontal quadrupolar impedance calculations.

Two Parallel Graphite Plates

For the simulations of measurements of two parallel graphite plates, two different methods were used. Due to the non-ferritic properties of the graphite, it is possible to use Maxwell3D to simulate the power loss at lower frequencies, thus acquiring the real component of the impedance for low frequencies, in addition to using the classical coaxial wire method at higher frequencies in HFSS.

For the simulations of the power loss in Maxwell3D the following parameters were used; for the displaced single wire measurements a wire of 0.5mm in radius is used, and the following displacement used to acquire the total transverse terms:

1. In the horizontal axis - displaced between -6mm to +6mm at intervals of 2mm

2. In the vertical axis - displaced between -4mm to +4mm at intervals of 2mm.

For the two wire simulations, two wires of radius 0.3mm are used, with a seperation

of 8mm in the x-dimension, and 4mm in the y-dimension. 5 simulation configurations are used as described below:

1. an adaptive mesh generation set to a convergence criteria of S_{21} diverging by less than 0.005 between two subsequent solutions, at an adaptive frequency of 20kHz solving to a second order basis. A discrete frequency sweep is then carried out in the range 1-10kHz at 1kHz intervals.

2. an adaptive mesh generation set to a convergence criteria of S_{21} diverging by less than 0.005 between two subsequent solutions, at an adaptive frequency of 200MHz solving to a second order basi. A discrete frequency sweep is then carried out in the range 10-100kHz at 10kHz intervals.

3. an adaptive mesh generation set to a convergence criteria of S_{21} diverging by less than 0.005 between two subsequent solutions, at an adaptive frequency of 2MHz solving to a second order basis. A discrete frequency sweep is then carried out in the range 100kHz-1MHz at 100kHz intervals.

4. an adaptive mesh generation set to a convergence criteria of S_{21} diverging by less than 0.005 between two subsequent solutions, at an adaptive frequency of 10MHz solving to a second order basis. A discrete frequency sweep is then carried out in the range 1-10MHz at 1MHz intervals.

5. an adaptive mesh generation set to a convergence criteria of S_{21} diverging by less than 0.005 between two subsequent solutions, at an adaptive frequency of 100MHz solving to a second order basis. A discrete frequency sweep is then carried out in the range 10-100MHz at 10MHz intervals.

These parameters are used to benefit from an appropriate mesh count for the given frequency range, thus increasing simulation speed by not using a high density mesh at frequencies where no benefits would be gained.

For the simulations of the single displaced wire in HFSS the following parameters were used; for the displaced single wire measurements a wire of 0.3mm in radius is used, and the following displacements to acquire the total transverse terms:

1. In the horizontal axis - displaced between -6mm to +6mm at intervals of 2mm

2. In the vertical axis - displaced between -4mm to +4mm at intervals of 2mm.

For the two wire simulations, two wires of radius 0.3mm are used, with a seperation of 4mm in the x-dimension, and 3mm in the y-dimension. 3 simulations configuration are used as described below:

1. an adaptive mesh generation set to a convergence criteria of S_{21} diverging by less than 0.005 between two subsequent solutions, at an adaptive frequency of 20MHz solving to a second order basis. A discrete frequency sweep is then carried out in the range 1-10MHz at 1MHz intervals.

2. an adaptive mesh generation set to a convergence criteria of S_{21} diverging by less than 0.005 between two subsequent solutions, at an adaptive frequency of 200MHz solving to a second order basi. A discrete frequency sweep is then carried out in the range 10-100MHz at 10MHz intervals.

3. an adaptive mesh generation set to a convergence criteria of S_{21} diverging by less than 0.005 between two subsequent solutions, at an adaptive frequency of 2GHz solving to a second order basis. A discrete frequency sweep is then carried out in the range 100MHz-1GHz at 100MHz intervals.

As before these parameters are used to benefit from an appropriate mesh count for the given frequency range, thus increasing simulation speed by not using a high density mesh at frequencies where no benefits would be gained.

The longitudinal impedance can be seen in Fig. 4.1.4. It can be seen that the agreement for both the real component is excellent across the entire frequency range, for simulations using both the classical coaxial wire method and the power loss method of Maxwell3D.
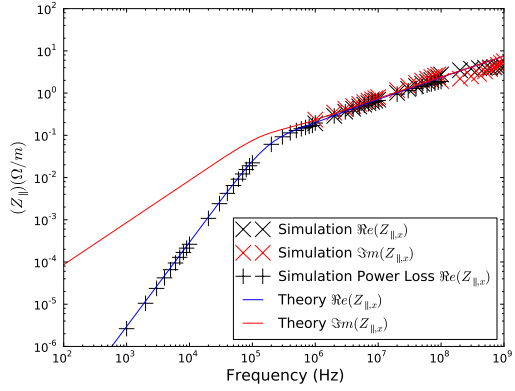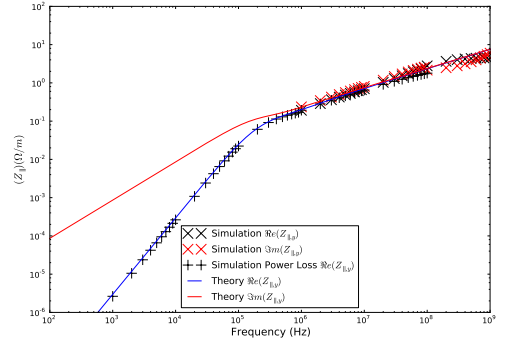
(a)   (b)

Figure 4.12: The longitudinal impedance of two parallel graphite plates as measured by taking the constant term of a quadratic equation fitted to a series of displaced single wire measurements. Shown are measurements acquired from fitting displacements in 4.12(a) horizontal axis and in 4.12(b) the vertical axis.
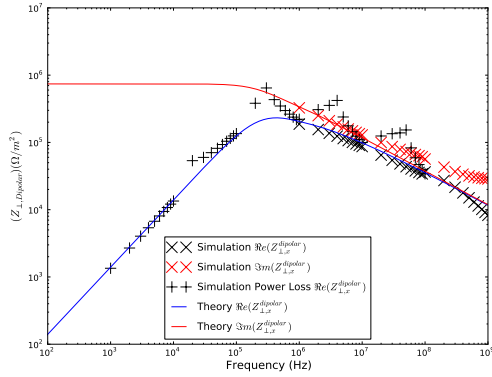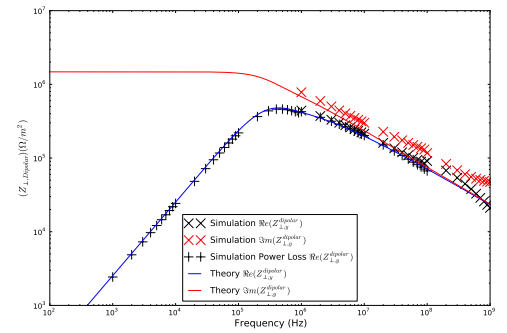
(a)   (b)

Figure 4.13: The dipolar impedance of two parallel graphite plates measured using two longitudinal coaxial wires. Presented are is the impedance as measured in the horizontal plane (4.13(a)) and in the vertical plane 4.13(b).
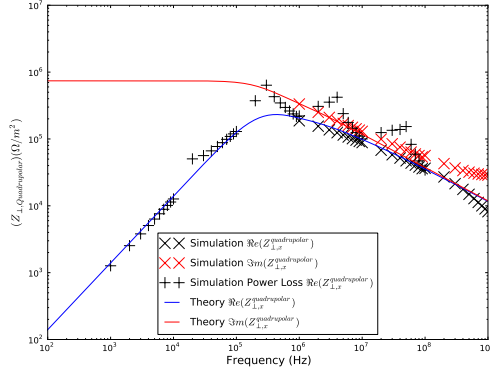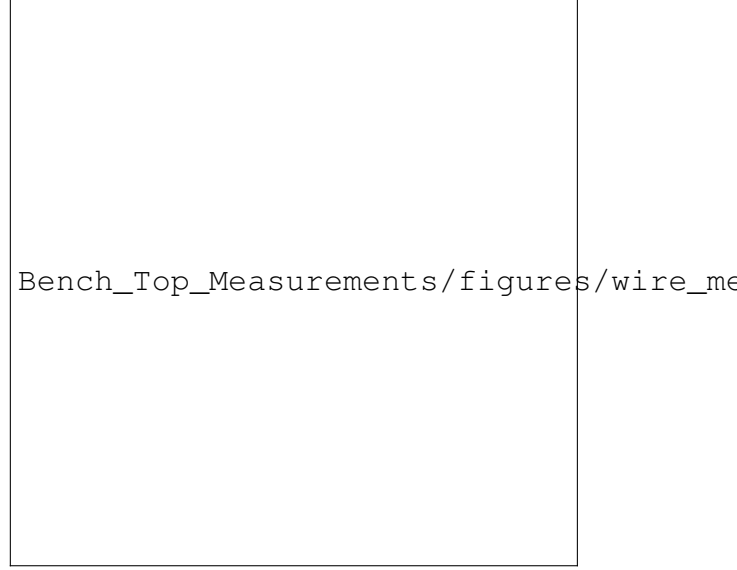
Figure 4.14: The quadrupolar impedance of two parallel graphite plates measured using a combination of displaced single wire measurements and two wire mesurements. Presented are is the impedance as measured in the horizontal plane (4.14(a)) and in the vertical plane 4.14(b).

The agreement is also good for the imaginary component over much of the frequency range, becoming worse above 100MHz. This is likely due to insufficient mesh density to catch the relatively small phase shift at this frequency range.

The agreement between simulations and theory for the vertical dipolar impedance can be seen to be very good over the entire frequency range also (see Fig. 4.13(b)). The results at low frequencies (below 100kHz) for the power loss method and at all frequencies for the classical coaxial wire method for the horizontal dipolar impedance agree very well with theory (see Fig. 4.13(a)).

4.2 High Q-factor Impedances

For high Q-factor impedances, such as cavity impedances, it is not appropriate to use a coaxial wire method to measure the impedance due to the large perturbation of the boundary conditions that it causes [ref Vaccaro coaxial method], in particular below the cut-off frequency of the connecting beam pipes. This is due to the presence of the coaxial wire

(a)   (b)
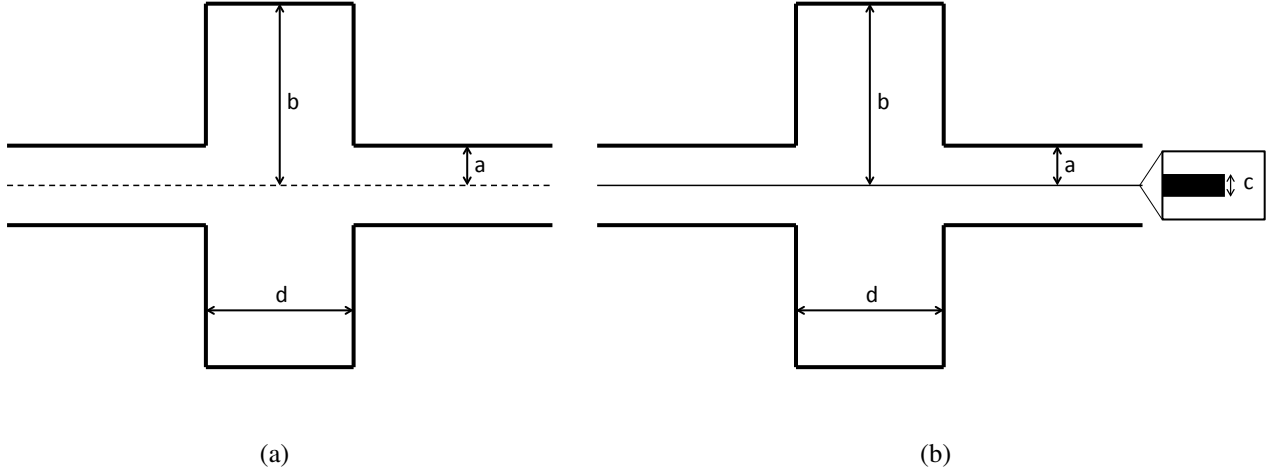
Figure 4.15: Comparison of the geometries of a cavity and attached beampipes 4.15(a) without and 4.15(b) with the coaxial wire in place. Note the dimensions and that the dashed line in 4.15(a) represents the rotational plane of symmetry

reducing the cut-off frequency to 0Hz, thus allowing propogation losses at all frequencies rather than just above cut-off. To illustrate this, we can consider the total Q of a cavity to be related to the "trapped" cavity mode Q and the propogation losses as;

$$\frac{1}{Q_{total}} = \frac{1}{Q_{cavity}} + \frac{1}{Q_{prop}} \tag{4.54}$$

Under excitation by a charged particle beam, propogation losses do not exist below the cutoff frequency and thus $Q_{prop} = 0$. However, the addition of the coaxial wire causes these propogation losses to occur at all frequencies. Importantly, the Q-factor of these propogation losses is of a similar magnitude or smaller than that of the cavity resonance, leading to a great distortion of the measured Q. Similarly, the perturbation of the conductive wire in the centre of the structure leads to a shift in the resonance frequency of the cavity modes.

To illustrate this phenomena, a number of simulations have been carried out to compare the measurements using the coaxial wire method compared to the impedance as simulated using CST Particle Studio[ref]

93

Chapter 5

Computational Simulations of Beam Coupling Impedance

Whilst beam-based measurements and bench-top measurements techniques have been used for some time to measure the impedance of devices and machines, the use of numerical codes to solve 2D and 3D structures is relatively young as a method of identifying the impedance of devices. Recent progress in computational power has now made these a powerful tool in the regime of impedance evaluation. Codes exist that solve simple 2D structures (ECHO2D, ABCI [ref both]), 3D structures (CST Particle Studio, HFSS, Maxwell 3D, ECHO3D, MAFIA) and 3D structures using highly parallelised codes (GdFidl, ACE3P) which allow the simulation of large, complex structures. The codes may be seperated in to two seperate families of codes; time-domain, which calculate the EM fields in a structure by solving Maxwell's equations in the time domain due to a signal inpulse, and frequency-domain which can be used in a number of ways to simulate the beam coupling impedance.

Each of these families of codes has there own relative advantages and disadvantages and peculiarities to use. In this chapter there will a general introduction to a number of the techniques that may be used to calculate the beam coupling impedance from both time-domain and frequency-domain simulations, along with the limitations of each method.

5.1 Time Domain Simulations

- A VERY general introduction to time domain simulations codes. This is not a thesis of computational methods, only one thing you may do with them. Write this way

- General experience - advantages of time domain methods (speed, memory footprint). Weaknesses (mesh resolution of structure, CPU limitation, long simulations times for high-Q resonances)

5.1.1 Direct Simulation of a Particle Beam

A large majority of time domain simulation codes (ECHO, MAFIA, CST Particle Studio, GdfidL) use a method that in effect simulates the passage of a particle beam through the structure and evaluates the subsequent electromagnetic fields in the structure by this signal. This is done in the following way:

1. A signal representing the source bunch is defined using a given profile, and then passed through the structure from a defined starting displacement and at a given velocity. Additionally a line of integration is defined along which the witness signal will be taken. This is effect defines a source bunch and a witness particle.

2. The simulation is propogated for a given period of time to acquire a significant quantity of the wakefield to correctly analyse the frequency components. It can be seen that for both high-Q resonances and low frequencies this requires a longer wakelength, to encompass the long damping time and correctly resolve the signal this frequency respectively.

3. The observed signal is subsequently deconvolved with the source signal to obtain a single particle wakefunction.

4. This may then be fourier transformed (using an FFT algorithm or other numerical methods) to acquire the beam coupling impedance.

(a)(b)(c)(d)

Figure 5.1: An illusration of the 5.1(a) source signal and 5.1(b) witness integration in a time domain code. The source signal and the resulting wakefield are shown in 5.1(c), and the subsequent calculated impedance in 5.1(d).
??

These steps are illustrated for clarity in Fig. **??** using a simple pillbox cavity as an example using the time domain code CST Particle Studio.

It can readily be seen that by defining either the source signal or witness at different displacements it is possible to acquire both the dipolar and quadrupolar impedances. Additional, by taking the gradient of the transverse impedances any constant transverse impedance terms can also calculated.

5.2 Frequency Domain Simulations

There are a number

- Advantages of frequency domain - good resolution of structure by meshing, fast solution for individual modes, accurate for resonant structures. Weaknesses - Very memory intensive. Very time consuming to characterise structures over a large frequency ranges

5.2.1 Eigenmode Simulations

Eigenmode solvers are a subset of frequency domain solver that are used to identify strongly resonant modes in a structure. These can be cavity modes, antenna like oscillations or a number of other resonances within the structure. The resulting output of the simulation is typically the resonant frequency of the eigenmode(s), the quality factor Q of the mode (if lossy boundary materials are defined) and the field pattern of the eigenmode solution.

From the field pattern it is possible to readily calculate the longitudinal and transverse R/Q of each cavity mode as defined in Sec. **??**. The field patterns may also be used to

calculate a number of other properties for each eigenmode, such as surface losses and stored energy in the cavity, which will be explained in further details in Sec. **??**.

- To identify cavity modes of structures

- Extract the resonant frequency and Q of cavity modes

- fields on axis/off axis to extract R/Q, transverse R/Q

5.2.2 The Coaxial Wire Method by Simulation

The coaxial wire method as described in Sec. **??** can be directly simulated using waveguide ports to represent matched connections at the ends of the device under test. The resulting simulations provide a transmission coefficient S_{21} which may subsequently be evaluated in the same manner as measurements made with a physical wire. As with the measurements used in practice, a displaced wire and two wires may be simulated and again treated as measurements.

- port solutions for driven modal simulations

- Allow the extraction of S21

- Evaluate as in previous section

5.2.3 Simulation of the particle beam

It is also possible to simulate a particle beam directly in the frequency domain. This is done by defining a wave source that produces a field similar to that of the particle beam. For ultrarelativistic beams this neccessitates a source field that is tangential to the direction of motion, and this may technically be possible for cases in which $\beta < 1$. The field components due to the source may be acquired and are the equivalent of the wakefield contribution at a given frequency. The beam impedance Z can subsequently be easily evaluated from the resulting fields

- Refer back to the nature of the EM field surrounding a charged particle beam (TEM-like)

- We can enforce a TEM like profile on emitted radiation of a surface

- With a TEM source with no wire - basically a particle beam

- Evaluation as mentioned in Oleksey's paper

Chapter 6

Beam Coupling Impedance Reduction Techniques

- Introduction to the concepts behind impedance reduction - we must let the image currents follow a path of miniml resistance

- Commence introduction to different impedance reduction methods

6.1   Tapering of Step Transitions

Although the ideal beam pipe of an accelerator would be a pipe of unchanging diameter, it is often necessary to vary the width of the beam pipe for the use of beam instrumentation, insertion devices and machine protection, amongst others. As was shown in Sec. 2.2.3, the presence of changes in the pipe diameters gives rise to beam impedance originating at the point of transition. It has been previously demonstrated that this impedance is heavily influenced by the angle of the transition [cite], in addition to the frequency of the resonance of the resulting cavity structure. In particular, this has an influence on the low-frequency broadband impedance, with gentler slopes causing a reduction in the low-frequency impedance.

There are of course space constraints which restrict the length which tapers may have, both in terms of machine length and the neccessities of size due to the correct operation

Figure 6.1: An example pillbox structure with and without a tapered transition region 6.1(a), in this case with the taper at 45°. The resulting imaginary component of the longitudinal impedances are shown in 6.1(b), as these are the most significant for beam stability.

Figure 6.2: Examples of both 6.2(a) transition pieces (for the SPS Injection Kicker Magnets, between the kicker cells and the vacuum tank) and 6.2(b) RF fingers (in this case for the PIMS module, placed between cryo-modules in the LHC).

of the device (for example, collimators or beam instrumentation such as synchrotron radiation monitors). And example of this approach is shown in Fig. 6.1. This reduction technique has a strong effect of the broadband impedance contribution of a strong resonant impedance caused by step transitions. In particular, it is effective at reducing the imaginary component of the longitudinal beam coupling impedance, as could be seen in the design of the LHC Yellow Book design report for instance [cite]. In this case it was determined that all transitions must observe a maximum gradient of 15° unless a design requirement neccessitated otherwise.

- Introduction to the changes in impedance with the steepness of a taper

6.2 Transition Pieces

Often it is necessary to have transitions in the beam pipe which can not be tapered, either due to space constraints or the operational requirements of the device containing the transition. This a common requirement in devices that require some mechanical freedom, such as bellows, or electrical isolation from the beam pipe, such as kicker magnets. For these devices it is often possible to use a transition piece, that is a one or several pieces of conducting material to screen any transition. These may be rigid, as is shown in Fig. 6.2(a), or moveable as shown in Fig. 6.2(b), often referred to as RF fingers.

This method of impedance reduction is effective for a number of reasons. Firstly it provides a short, good conducting path for the image currents to flow that does not

(a)(b)

(c)

Figure 6.3: The layout of the RF fingers in the VMTSA both in 6.3(a) the fully operational configuration and 6.3(b) when the RF fingers lose contact. 6.3(c) shows the resulting beam coupling impedance of the two types of impedance as acquired by coaxial wire measurements.

expose it to the cavity created by the transition. This serves to reduce the broadband impedance increase due to the transition. Secondly, by correctly designing the spacing in the transitions, it is possible to minimise field leakage to the surrounding cavities therefore decreasing the visibility of cavity resonances. As an example of a cavity with and without RF fingers and a number of intermediatary steps, see Fig. 6.2, which illustrates the case of the VMTSA, a vacuum interconnect in the injection region of the LHC. It is characterised by a large vacuum chamber (due to needing to contain two circulating beams) with a long set of bellows. They were screened by a long set of RF fingers, which functioned well when good surface contact was maintained between the fingers and the beam pipe. However, when this connection was disrupted (easily created via mechanical stress due to the weak pressure exerted by the afixing spring).

6.3   Conductive Coatings

As can be seen in Sec. 2.2.4, a higher conductivity in the material seen by the beam in a particle accelerator results a lower beam coupling impedance. Typically this rule of thumb is followed in the design of particle accelerators, however the operational requirements of devices in the machine often require that they not be made from a good conducting material. Examples of this include collimators (requiring high strength, mechanical stability and certain radiation properties), beam instrumentation and numerous other devices.

It has been seen [citey mccite cite] that a thin layer of high conductivity material placed on the surface of a poorly conducting material can effectively screen the beam from interacting with the poorly conducting material for a large frequency range. This

can be explained by considering the skin depth of a material δ. As shown in Sec. 2.2.4,

$$\delta\left(\omega\right) = \sqrt{\frac{2}{\mu_0 \sigma \omega}}. \tag{6.1}$$

The skin depth can be thought of as the distance of penetration of the electromagnetic field into the material. In thus be seen that for a good conducting material like copper $(\sigma_{cu} \approx 6 \times 10^7 Sm^{-1})$, for frequencies of the order of a hundred megahurtz or above, a thickness of a $10\mu m$ is much larger than the skin depth at 100MHz $(\delta\left(100\text{MHz}\right) = 6\mu m)$, thus effectively screening the layer below. For many machines the part of the frequency spectrum of concern is above this area (most electron machines, small hadron colliders). It is possible to use thicker coatings (on the order of millimetres) for machines that require a very broad frequency range screened. This is investigated in detail in Sec. **??**.

6.4 Beam screens in kicker magnets

A substantial contributor to the beam coupling impedance in many machines, in both the longitudinal and transverse planes, are kicker magnets. These are magnets that generate a pulsed magnetic field for a limited period of time (i.e. not always on during beam operation as the dipoles and quadrupoles used for beam optics are), often for orbit corrections, extraction and injection. They have been known to be a problematic component of particle accelerators for a number of decades, mostly in lepton machines due to the traditionally higher beam currents that operate in these machines.

In lepton machines they suffered from problems of heating due to eddy currents induced by traversing bunches, and the neccessity that a remedy to this solution maintain the rapid rise time of the magnetic field required for normal kicker magnet operation, which typically requires a field rise time on the order of the bunch or bunch train seperation in a machine [citing all the cite].

A plain ceramic chamber contributes it's own problem from a beam impedance point of view, especially contributing a large imaginary component to the longitudinal impedance due to it's high permitivitty and poor conductivity. In addition it is liable to build up static

charges due to being an insulator in a region subject to high electric and magnetic fields. The solution to these problems neccessitates a thin conductive coating on the inside surface of the chamber, either a continuous thin layer (which itself can greatly reduce the field rise time of the kicker magnetic field), or the use of longitudinal stripes, which carry a large proportion of the beam image current, whilst maintaining the rise time characteristics of the magnetic field.

This method will be studied in further depth in Sec. **??**, with particular attention to the limitations in use in a high current hadron machine.

- Kickers are usually constructed from materials with either large losses (magnetic losses - ferrite) or from strong segmentations (laminated kickers) - both bad for impedance

- We need kickers - find a way to screen the beam from kicker material whilst allowing the kicker to operate as intended - capacitively coupled screens etc.

6.5   Seriagraphy on Kicker Magnets

As described in Sec. 6.4, kicker magnets are often a substantial contributor towards beam coupling impedance. For many machines they were not foreseen to be a limiting factor to beam operation during construction due to either low beam current, long bunch lengths, large bunch seperations or both. However, with increasing improvements in machine performance, it is possible that they may become a limiting factor, as was the case in the SPS extraction kicker magnets[cite].

For these existing devices, limitations of both time and budget may require the use of retroactive solutions to large beam impedances. Often these must be added to the original equipment, as the continued correct operation of the device requires minimal disruption to the geometry and surfaces of the device. In the case of the SPS extraction kicker magnet (SPS-MKE), the aperture size had to be preserved, as well as the field rise time of the kicker. In this an innovative solution was found - The use of seriagraphy. This entailed

(a)(b)(c)

Figure 6.4: An example of seriagraphy in the SPS Extraction Kicker Magnets (SPS-MKE). The layout of the interleaved fingers is shown in 6.4(a) and the actual seriagraphed magnets in 6.4(b). A comparison of the longitudinal beam coupling impedance with and without the seriagraphy is shown in 6.4(c).

the printing of a set of interleaved fingers (see Fig. 6.4) made from a good conductor (in the case of the SPS-MKE silver), which form a good conductive path for the beam image currents, capactively coupled across the seperation of the interleaved fingers. This serves to replace the broadband impedance typically associated with a ferrite dominated resistive wall impedance with a low broadband impedance, with strong resonant impedances due to the capcitively coupling and physical length of the fingers. The results in the case of the SPS-MKE can be seen in Fig. 6.4(c).

- Kicker magnet problems, introduced in

6.6   Use of damping materials to de-Q resonant caviities

For a number of devices it is unavoidable to have a cavity present in the structure. In addition it is often not possible to design the cavity with either tapering or transition pieces due to the need for moveable components, such as a wire scanner or a collimator whose aperture changes with beam parameters. In this case it is necessary to find a way of reducing the beam impedance by altering the properties of resonances. Often it is only the peak value of the impedance attributable to a resonance that is of concern from a beam stability/beam induced heating point of view.

If we consider the defining properties of a resonant impedance, f_{res}, R/Q and Q, there are a number of properties that should be noted in changing them. Both f_{res} and R/Q are strongly determined by the geometry of the structure, and thus can not be significantly modified without possibly neccessitating a modification of the device being altered which may hinder the intended operation. Thus one approach to use is to alter the Q of the

Figure 6.5: The complex permeability of a number of sample materials used to damp cavity modes.

resonance. A well known method of altering the Q of a resonant cavity is to add a dispersive or ferritic material to the cavity volume [cite ferrite RF cavities from CAS RF for accelerators], that is a material that has complex permitivitty or permeability , given by $\epsilon_r = \epsilon' - j\epsilon''$ and $\mu_r = \mu' - j\mu''$ respectively. An example of the permeability of some sample ferrite damping materials is shown in Fig. 6.6

The addition of this family of materials to the cavity has the following effect on the cavity resonances:

1. The resonant frequency of any resonance ω_{res} is reduced by the inclusion of the dispersive material. This can be understood either by considering the μ_r/ϵ_r increasing the effective electrical volume of the cavity by it's inclusion, thereby increasing the dimensions of the resonant cavity. Alternatively, considering the RLC equivalent circuit of a cavity resonance, the inclusion of the dispersive material increases either or both of (depending the properties of the material) the inductance and capacitance of the cavity.

2. The R/Q of the cavity experiences little change. There is a slight modification; either an increase that can be attributed to the increased stored energy in the cavity mode due to ϵ' 1 or a decrease due to the reaaranging field patterns (caused by the incluson of the dispersive material) decreasing the stored energy.

3. The Q of the resonance is drastically reduced. This is due to the strong change in the damping time of the resonance that the addition of the damping material. In terms of cavity properties this can be thought of as the losses in the cavity increasing more rapidly than the stored energy in the cavity. In equivalent circuit terms this may be thought of as the capacitance of the cavity decreasing or the inductance increasing depending on whether a dielectric or ferrous material is added.

Figure 6.6: The change in the peak impedance value of a cavity impedance with a constant R/Q, but changing Q.

As can be seen, the resulting effect is to drastically reduce the Q of a cavity resonance, and then by the relation $R_s = R_s/QQ$ it can be seen that the shunt impedance will decrease proportional to Q. This reduces the peak of R_s, but broadens the width of the resonance peak, as can be seen in Fig. 6.6. This indicates two effects of using damping materials as an impedance reduction technique; effects dependent on the shunt impedance R_s are suppressed, however effects dependent on the broadband behaviour may suffer negatively as a result. Due to the strong frequency dependent nature of many impedance-driven instability mechanisms and beam-induced heating, these negative side effects rarely outway the benefits using damping material in a cavity if necessary.

6.6.1 Heat Loads on the Damping Material

During experience of estimating the heat loads on ferrite damped cavities in high intensity hadron machines (see Sec. **??** for more details), a number of surprising observations were made. In particular was that the placement of ferrite in a cavity does not always produce a significant reduction in the Q of a resonance and that is such cases the percentage of the power loss in the ferrite was comparatively small compared to conventional wisdom, this being that the ferrite experienced the majority of the heat load of the damped cavity. It was thus decided to investigate how the addition of a damping material, in this case a ferrous material, to a cavity would alter both the characteristic resonance properties of the cavity and the location of the power load due to interaction with the beam in the cavity.

Two different geometries were used, one of which could be treated analytically to provide a benchmark for the simulation code, and one in which the ferrite is shielded from being directly seen by the traversing beam, as is normally done to reduce the effects of a resistive wall type impedance due to the ferrite. These geometries are shown in Fig. 6.6.1. A single eigenmode of each cavity is investigated, both with and without a damping material.
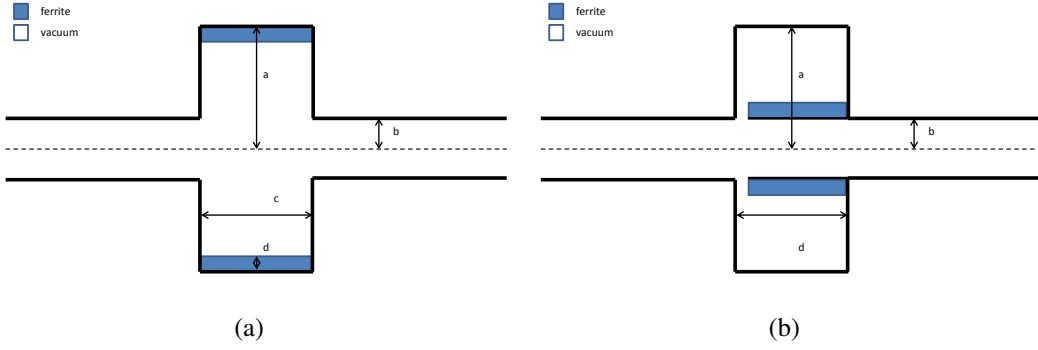
Figure 6.7: Two sample geometries used to examine the effects of ferrite damping material on cavity resonances. 6.7(a) shows a cavity with the ferrite unshielded, and 6.7(b) shows a more realistic case in which the ferrite is shielded from directly seeing the traversing beam.

For this analysis, a cavity of dimensions $a = 60mm$, $b = 5mm$, $c = 20mm$, made from a material with a conductivity $\sigma = 1.1 \times 10^6 Sm^{-1}$ is used for the simulations of an unshielded cavity. A layer of "ferrite" 0.5mm thick is placed as shown in Fig 6.7(a). This material is given the following properties: $\epsilon' = 10$, $\epsilon''/\epsilon' = 0$, $\mu' = /1$. μ''/μ' is changed between 0 and 0.02 in steps of 0.02 in order to alter the Q of the resonant mode in incremental steps with the intent of observing how the properties of the cavity change with different scales of damping of the resonance. The "ferrite" is also given a mild conductivity ($\sigma_{ferr} = 10^{-6} Sm^{-1}$) as is normal in accelerator ferrites to reduce electrostatic charge build up. For comparison to an analytical formalism, we use the Biancacci finite length impedance model for axisymmetric structures [cite Biancacci IPAC '12].

For the shielded geometry, we use a cavity of the same dimensions as for the unshielded case, with a layer of conductive material 1mm thick placed on the interior of the cavity. A gap of 5mm is left between the beam pipe and the cavity for the beam to couple to the cavity. A ring of ferrite 0.5mm in thickness is then placed on this surface as is shown in Fig. 6.7(b).

Before carrying out the analysis of the location of the heat loss in ferrite, it is prudent verify that the losses calculated using the field calculator in HFSS are self-consistent and well understood. HFSS calculates two losses internally; the surface loss density and

volume loss density. The surface loss density p_s is defined in HFSS as

$$p_s = \Re e\left(\mathbf{S.n}\right) \tag{6.2}$$

where $\mathbf{S}$ is the Poynting vector and n is the out normal vector to the surface boundary[cite HFSS docs]. By integrating this over all surfaces the total surface losses in the cavity are obtained. The total wall losses are also given by

$$P_{loss,wall} = \frac{R_{wall}}{2}\int_S |\mathbf{H_{surf}}|^2\, dS \tag{6.3}$$

where R_{wall} is the surface resistance of the wall and $\mathbf{H_{surf}}$ is the surface magnetic field.

HFSS defines the volume loss density p_v as

$$p_v = \frac{1}{2}\Re e\left(\mathbf{E.J} + \left(-\nabla \times \mathbf{E}\right).\mathbf{H}\right) \tag{6.4}$$

where again this may be intergrated over all space to obtain the total volume losses. In addition to these methods of loss calculations of the losses due to the fields in the cavity, it is possible to calculate an equivalent loss of a particle traversing on axis. By considerations of ohmic losses, with the voltage V that experienced by the particle traversing the cavity, the voltage $R = R_s$ the shunt impedance of the cavity resonance and I the beam current. As the eigenmode simulation does not directly simulate a beam, the effective power loss is given by

$$P_{loss} = \frac{V^2}{R_s}. \tag{6.5}$$

The surface losses and volume losses are subsequently seperately compared. For the surface losses, the internal surface loss density integrated over all surfaces calculated by HFSS, wall losses as given by Eqn. **??** and the equivalent losses of a particle on axis are compared. For this we use the unscreened cavity with no ferrite present to have only surface losses present. The different calculated results are shown in Tab. 6.1, given in watts normalised to a peak electric field of $1 vm^{-1}$ in the cavity. It can be seen that the

Table 6.1: Comparison of the power loss on the surface of a pillbox cavity by both direct calculation and internal calculation by HFSS (In units normalised to 1V/m maximum electric field)

Calculation Type	Normalised Power Loss (W)
Direct Calculation	6.2e-10
HFSS Internal Loss Calculations	6.22e-10
Loss of an on-axis particle	5.1e-10

Table 6.2: Comparison of the power loss in the volume of a pillbox cavity by both direct calculation and internal calculation by HFSS (In units normalised to 1V/m maximum electric field)

Calculation Type	Normalised Power Loss (W)
Direct Calculation	1.28e-8
HFSS Internal Loss Calculations	1.29e-8
Loss of an on-axis particle	1.33e-8

two calculations due to the surface fields themselves agree exceptionally well, and the calculation for the equivalent loss of an on-axis particle is agrees to within 20%.

For the volume losses the cavity geometry for the unshielded case is used, with a layer of ferrite 0.5mm thick on inside surface of the cavity. This ferrite has the following material properties; $\epsilon' = 10$, $\epsilon' = 0$, $\mu' = 10$, $\mu''/\mu'' = 0.1$. For this comparison the internal volume loss density integrated over the whole volume as calculated by HFSS, calculating the volume losses using Eqn. 6.4 and the equivalent loss of an on axis particle are calculated, again with loss normalised to a peak electric field of $1Vm^{-1}$ in the cavity. The results are shown in Tab. 6.2. It can be seen that the agreement between all three methods of calculating the losses in the cavity is exceptionally good, differing by less than 10%.

The resulting real component of the longitudinal beam coupling impedance for the case of unshielded ferrite is shown in Fig. 6.6.1. The change in the resonant frequency and the increase in the peak impedancefrom the cavity without any damping material to that with is due to the presence of a region of $\epsilon_r > 1$. Clearly seen can be the effect of the presence of increasing loss tangent of the ferrite, greatly broadening the impedance
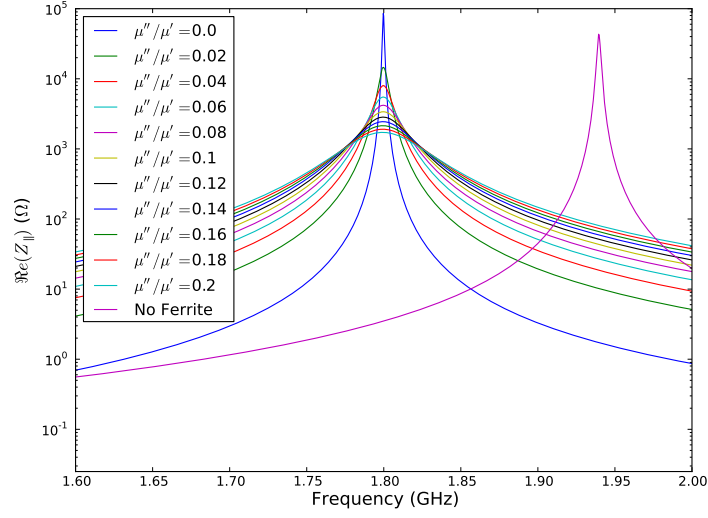
Figure 6.8: The real component of the longitudinal beam coupling impedance of a cavity without and with a damping material with $\epsilon' = 10$, $\mu' = 10$ and μ'/μ' is varied. The non-damped cavity is shown for comparison. The change in resonance frequency and shunt impedance impedance is due to the increased ϵ' of the damping material.

peak, with the effect of reducing R_s of the resonance. The cause of this reduction of R_s can be attributed to the reduction in Q for each resonance, as shown in Fig. 6.9(a). It can be clearly seen that the presence of a small piece of ferrite very strongly decreases the Q of a resonance. The corresponding change in the percentage of the power loss in the ferrite itself as the Q is decreased is shown in Fig. 6.9(b). It can be seen that the power loss is rapidly localised to the ferrite as the Q decreases. To quantification to this power loss, the power loss due to this cavity resonance is calculated assuming a beam with 1.15×10^{11} particles per bunch, 288 bunches, a ring circumference 6911m and a bunch length $4\sigma = 0.04m$ assuming a gaussian bunch distribution and that the resonance falls on a beam harmonic, shown in Fig. 6.6.1. Here it can be clearly seen that the power loss in the ferrite rapidly converges to the total losses in the cavity, confirming the assumption that most of the power loss for a cavity resonance damped by a damping material is lost in the damping material. Further information on the numerical results of these simulations is give in Appendix. **??**.

For the case of the shielded ferrite, the real component of the beam coupling impedance

(a) (b)
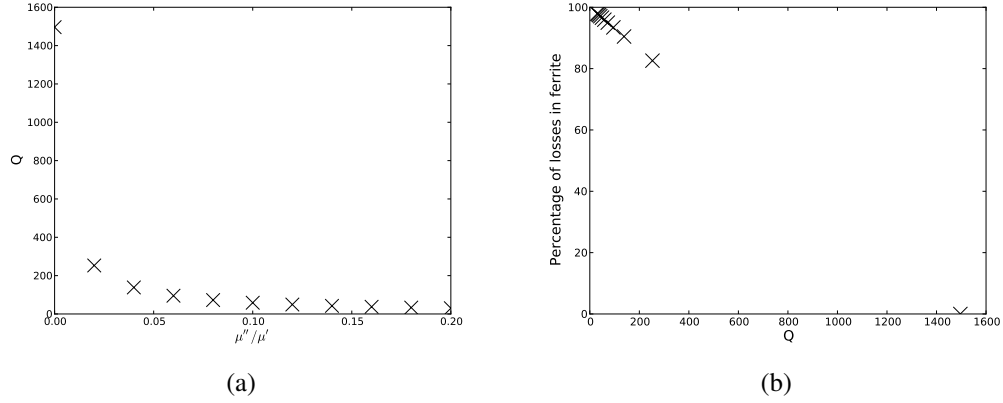
Figure 6.9: 6.9(a) The reduction in the Q of the cavity resonance with the increasing loss tangent of the ferrite damping, showing a strong decrease of the resonant Q with a small increase in loss tangent. 6.9(b) The percentage of the power loss in the ferrite as the resonant Q decreases. this can be seen to tend towards 100% as the Q approaches 0.
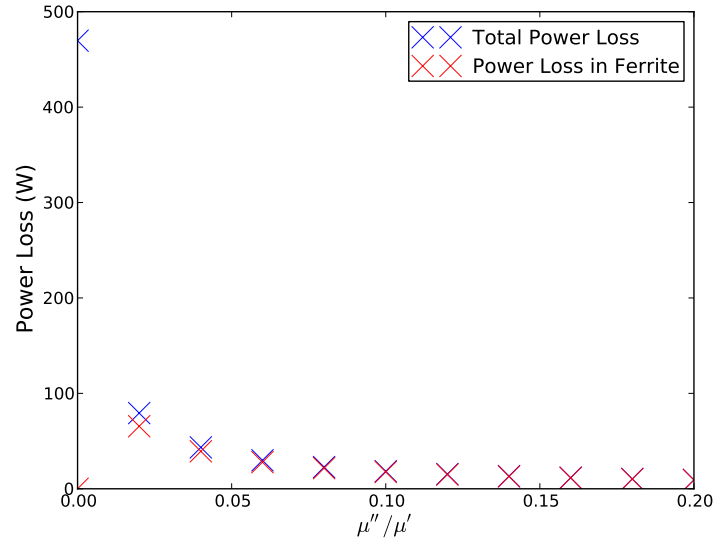
Figure 6.10: The power loss due to a beam with 1.15×10^{11} particles per bunch, 288 bunches, a ring circumference 6911m and a bunch length $4\sigma = 0.04m$ assuming a gaussian bunch distribution in the unscreened cavity.
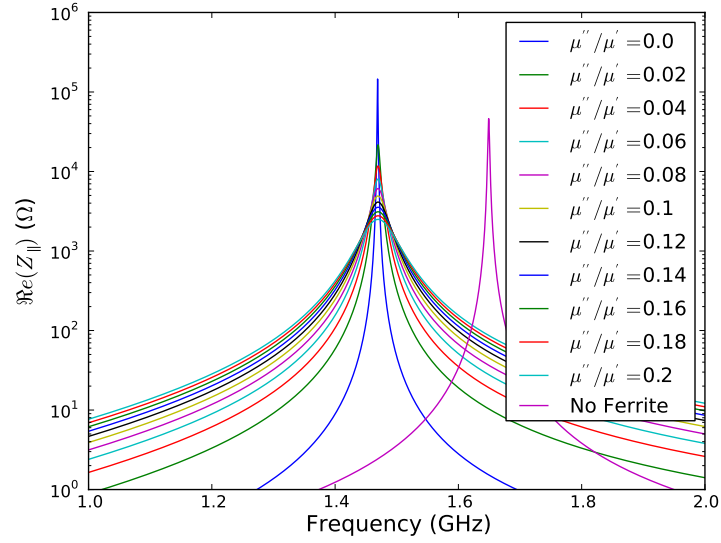
Figure 6.11: The real component of the longitudinal beam coupling impedance of a cavity without and with shielded damping material with $\epsilon' = 10$, $\mu' = 10$ and μ'/μ' is varied. The non-damped cavity is shown for comparison. The change in resonance frequency and shunt impedance impedance is due to the increased ϵ' of the damping material.

is shown in Fig. 6.6.1. As with the case of the unshielded ferrite, the addition of the damping material causes a decrease in the resonant frequency of the cavity mode, again due to the addition of a material with $\epsilon_r > 1$. In addition, the shielding causes a further decrease in the resonant frequency, in this case due to the rearrangement of the field lines due to the changed boundary conditions.

As can be seen from Fig. 6.12(a) the decrease in the Q of the resonance by the increasing more lossy ferrite follows a similar pattern to that shown by the unshielded structure, as is the increase in the percentage of power loss in the ferrite for the increasing damping of the resonance, shown in Fig. 6.12(b). The corresponding change in the power loss in both the cavity as a whole and the ferrite is shown in Fig. 6.6.1. As with the unscreened case, the power lost in the ferrite rapidly converges with the power loss in the entire cavity, indicating that magnetic losses are dominating the losses.

From these results it can thus be seen that the inclusion of the shielding does not substantially effect the losses due to strong cavity resonances, whilst aiding in reducing

(a)   (b)
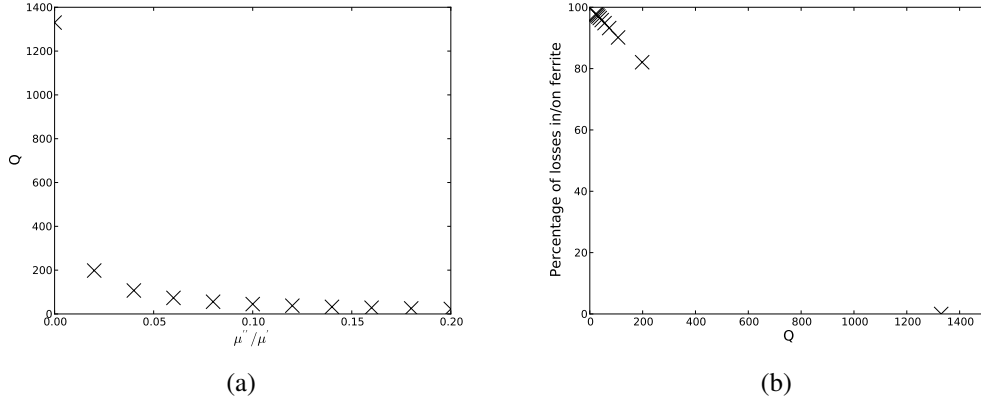
Figure 6.12: 6.12(a) The reduction in the Q of the cavity resonance with the increasing loss tangent of the ferrite damping, showing a strong decrease of the resonant Q with a small increase in loss tangent. 6.12(b) The percentage of the power loss in the ferrite as the resonant Q decreases. this can be seen to tend towards 100% as the Q approaches 0.
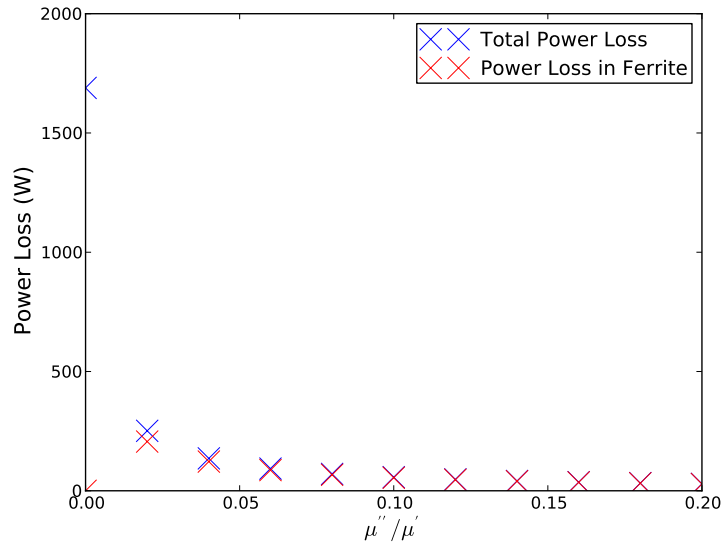
Figure 6.13: The power loss due to a beam with 1.15×10^{11} particles per bunch, 288 bunches, a ring circumference 6911m and a bunch length $4\sigma = 0.04m$ assuming a gaussian bunch distribution in the screened cavity.

113

the effects of image current flowing through the ferrite (a broadband effect, and thus not considered in the eigenmode simulations). In addition, we see that if the cavity mode is strongly damped by the presence of ferrite (i.e. the Q is reduced by a factor 20 or so) it should be expected that the vast majority of the remaining power lost by particles interacting with the cavity resoance should ultimately be lost in the damping material.

Chapter 7

LHC Collimation Upgrades

7.1 Introduction

The LHC collimation system is a key part of the machine protection system in the LHC. Due to extremely high stored beam and magnetic energy in the LHC [cite], amounting to some 160MJ of beam energy and 3GJ of stored magnetic energy, it is neccessary to keep close control on the losses experienced by the system. In the LHC this is done by a combination of monitoring the losses within the machine, carefully controlled losses by the collimation system, and a rigorous interlock system designed to dump the beam safely in the event of the development of dangerous behaviour by the circulating beam [LHC machine protection].

The collimation system in the LHC is a four-stage system, composed primarily of primary (TCP), secondary (TCS), and tertiary (TCT) collimators. These serve to scatter the particle halo, then further scatter and absorb the scattered particles. Further protection is provided by absorbers (TCLA), collimators at the injection regions (TCLI and TDI) and at the extraction region (TCDQA). In particular the TCTs are placed near the experimental IPs to protect the inner triplet magnets (used for final focusing of the beam before collision). In total the collimation system is broken down into two IRs; IR3 for betatron cleaning, in which there are:

1. 1 primary collimator

Figure 7.1: Different components the impedance reduction measures in the phase 1 collimator design. 7.1(a) shows the longitudinal RF fingers, ensuring a good conducting path for the beam image currents, and 7.1(b) shows the sliding RF contacts on the collimators jaw. These are intended to minimise the volume seen by the beam, thus making any cavity modes that may be excited by the beam at very high frequencies where the beam power spectrum is very small.

2. 4 secondary collimators

3. 4 absorbers

per beam and IR7 for momentum cleaning, which is composed of:

1. 3 primary collimators

2. 11 secondary collimators

3. 5 absorbers

per beam, with an additional 8 tertiary collimators (2 per experimental IP) per beam. In addition to the collimators at the injection and extraction region each beam is exposed to 44 different moveable collimators per circulation of the machine. The primary and secondary collimators presently all have a jaw material carbon reinforced graphite (conductivity $\sigma_{graphite} = 7 \times 10^4 Sm^{-1}$). This material was chosen due to the requirement for a robust jaw material (mechanically stable under large thermal shock) from a machine protection point of view, however not optimised from a beam impedance point of view.

The current collimation system has demonstrated to be exceptionally effective at it's job of providing machine protection to the LHC [cite Chamonix 2012 MP presentation], however it has been shown to be a limiting factor in the luminousity of the LHC due to the large contribution to the transverse beam coupling impedance by the primary, and especially the numerous secondary collimators in the system, which are also almost double the length of the primary collimators[cite].

The phase 1 collimator (those presently (as of 2012) in place in the LHC) designs have a number of design features that are designed to reduce the beam coupling impedance of

each device. Although the resistive wall contribution to the beam coupling impedance due to the poorly conducting jaw material is significant, the use of longitudinal RF fingers in the transition between the beam pipe to the collimator jaws and of a system of sliding contact fingers to isolate the beam from seeing the collimator vacuum tank (see Fig 7.1 for more details). These function well as impedance reduction techniques, however have some limitations from a mechanical point of view. In particular, the sliding contacts have been suspected to be a significant producer of dust in the LHC due to the moving physical contact during collimator alignment [cite].

Due to these factors (high transverse impedance due to the resistive wall impedance and problems of dust due to sliding contacts) a phase 2 upgrade of the LHC collimation system has been proposed. This entails two components;

1. The replacement of the current secondary collimators (the prime contributor to the large transverse impedance) by a phase 2 design using a good conducting material as the jaw material. There will be some loss of mechnical robustness but it is thought that this will not be detrimental to the requirements of machine protection with a suitable choice of material.

2. Replacing the existing sliding RF contacts with a contactless RF system (shown in Fig. **??**). This is designed to remove the problem of dust caused by the sliding RF contacts in the phase 1 system by removing the moving physical contacts. This increase the volume of the cavity visible to the particle beam, decreasing the frequency of the lowest cavity modes. To counteract these new resonances, ferrite is placed in the cavity to decrease the resulting Q of the resonances.

In this chapter shall be presented an comparison of the different jaw materials proposed for use in the phase 2 secondary collimators, in particular a combination of jaw materials aimed at combining extremely robust materials with highly conductive metals, and the results of full 3D simulations of a TCTP collimator - a tertiary collimator for use in the LHC - which is incorporates the ferrite damping system in comparison to the sliding contacts of the phase 1 RF system.
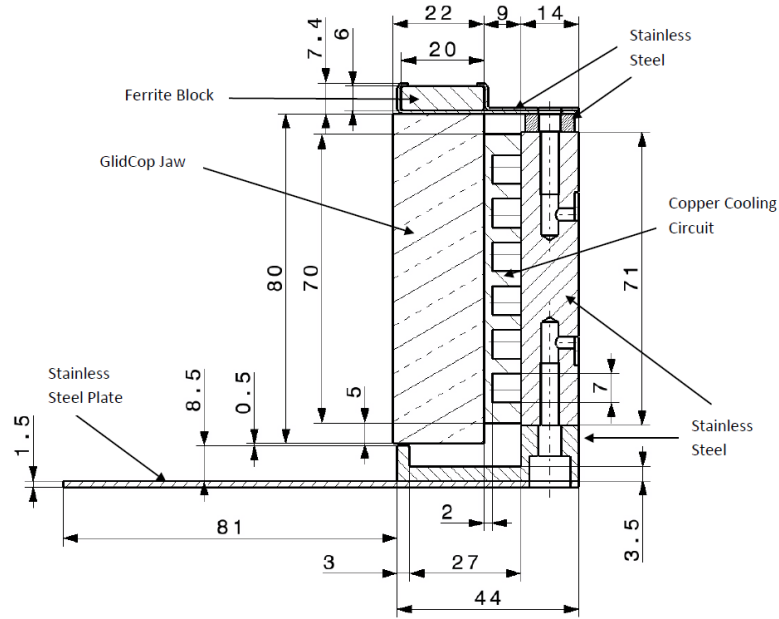
Figure 7.2: The RF system for use in the phase 2 collimation system. The sliding RF contacts of the phase 1 design are replaced with a ferrite damping system. The RF contacts are removed, allowing the beam to see the entire RF cavity, causing resonances at lower frequencies. The Q of these resonances are decreased by the use of ferrite damping tiles.

7.2 LHC Phase 2 Secondary Collimator Jaw Material

The phase 2 secondary collimators are proposed as an addition to the current phase 1 secondary collimators. They have stringent mechanical requirements, particularly due to the neccessity to withstand impacts by a limited number of bunches in the LHC during injection. In addition they must meet a stringent limit on beam impedance - new devices in the LHC must not increase the total impedance of the machine due to the stability limits imposed due to the existing large transverse and longitudinal impedance. If possible, the effective impedance in the machine should be reduced during operation. The requirements for the material requirements are detailed and summarised in [cite a. dallocchio phase 2 advanced materials].

To meet the strict requirements of the differing physical requirments on the jaw material, both from a mechanical point view and an impedance point of view a number of

Table 7.1: The electrical conductivity of the different jaw materials proposed for use in the phase 2 design. All results are given for measurements at room temperature (20°C)

Material	Conductivity (Sm^{-1})
Glidcop	5.4×10^7
Molybdenum	1.87×10^7
Copper Diamond Compositie (CuCD)	1.25×10^7
Molybdenum Diamond Composite (MoCD)	5.5×10^6
Graphite	7×10^4

different jaw design solutions have been proposed. These include both single jaw material designs, mixtures of composites and pure metals, and varities on a design including ceramic. The proposed jaw material combinations are listed below:

1. GlidCop, a copper compositie including aluminium oxide particles[ref]. The conductivity is marginally worse than pure copper (see Tab. 7.1), but the addition of the aluminium oxide greatly increases the resistance to thermal softening and increases the strength at high temperatures.

2. Molybdenum - An metal with good mechanical properties and a conductivity comparable to copper.

3. Copper Diamond Composite - A copper composite formed by hot pressing copper with the addition of boron powder and small synthetic diamonds. Produces a very mechanically robust material.

4. Molybdenum Diamond Composite - As with the above, a molybdenum compositie formed by the use of sintering molybdenum with artificial diamonds.

5. Carbon reinforced carbon (CFC) - The current material of the phase 1 secondary collimators. Included for comparison.

More information on the material choices can be found in [cite AD/AB papers]. The conductivities of the different materials can be found in Tab. 7.1. The layouts of the various possible jaw designs can be found in Fig. **??**.
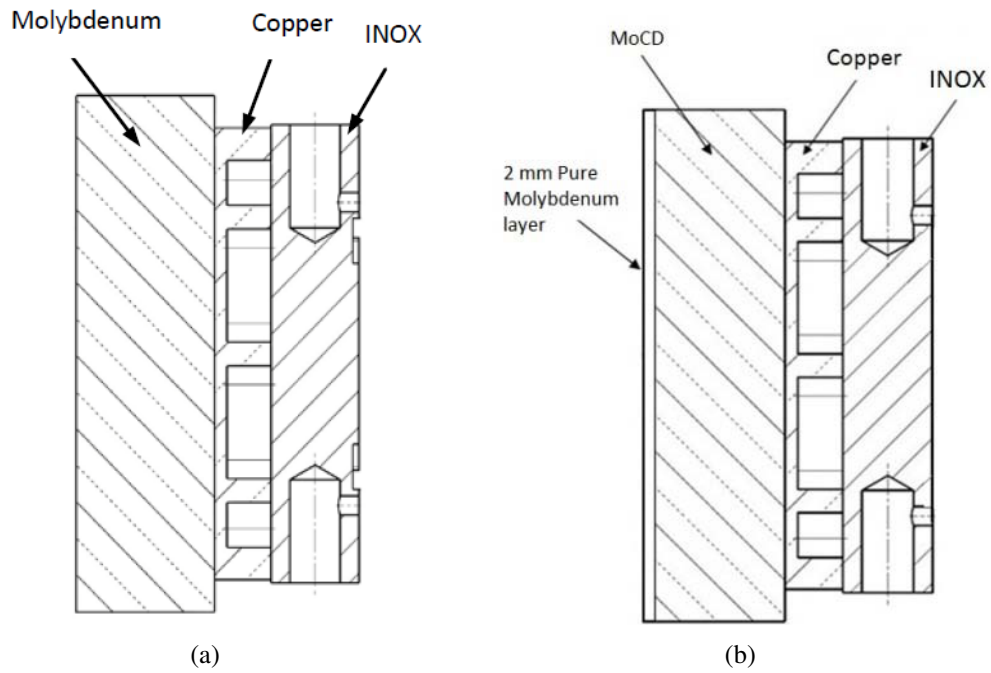
Figure 7.3: A number of the proposed jaw designs for the phase 2 secondary collimators. 7.3(a) shows the jaw made entirely from molybdenum. Glidcop maybe substituted for molybdenum in this design. 7.3(b) shows the jaw made from a mixture of molybdenum diamond composite with a 2mm coating of molybdenum on the surface. The composite ensure a mechanically strong jaw, whilst the coating screens the higher resistivity composite and provides a smooth surface on the beam-facing part of the jaw. In this case the composite maybe substituted with copper diamond composite, and likewise the coating may be replaced with GlidCop.
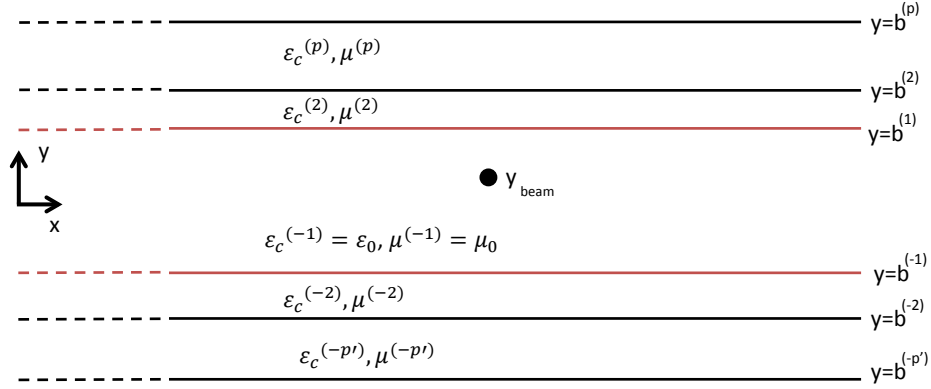
Figure 7.4: The physical model of the Mounet model of parallel plate impedance. Note that the two sides of the structure do not have to be symmetric. The materials maybe any material provided it's frequency dependent properties are well defined.

7.2.1 Impedance Studies and Analysis

To analyse the jaw material impedance the Mounet model [ref N. Mounet thesis/notes] for parallel plates with infinite layers is used. This model assumes infinite parallel plates with n-layers of material. It supports non-symmetric structures in addition. The representation of this structure is shown in Fig. 7.2.1. For this model we assume a jaw seperation of 4mm (half-width of 2mm), the closest nominal seperation of the secondary collimators.

The frequency range of concern is determined by the instability mechanism driving the stability limit in the LHC. It has been demonstrated that this range of concern is from 11.8kHz up to some number of GHz[cite phase 2 conf note] in the transverse plane, driven by loss due to tune spread over an optical resonance. This neccessitates investigating the transverse beam coupling impedance over a very large frequency range, hence the choice of using an analytical method of investigation.

The beam coupling impedances for the various jaw materials is shown in Fig. 7.2.1. From the consideration of the longitudinal impedance, the collimator jaw material is not a significant contirbutor to the machine impedance. The significant concern is the transverse impedance. It can be seen from **??** that all the potential jaw materials reduce the imaginary
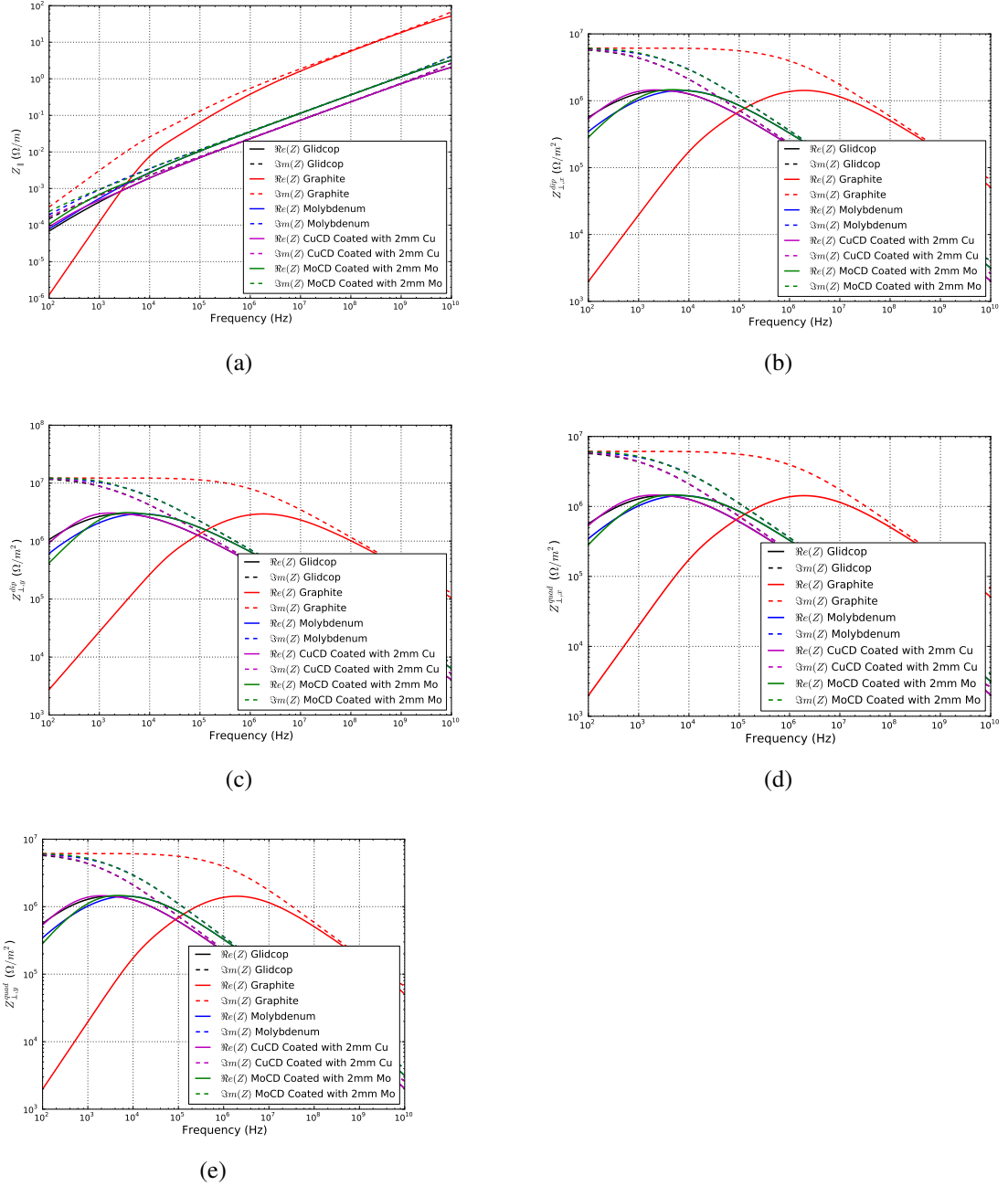
Figure 7.5: The impedances of different jaw materials for the phase 2 secondary collimators. 7.5(a) The longitudina impedance, 7.5(b) the horizontal dipolar impedance, 7.5(c), the vertical dipolar impedance, 7.5(d) the horizontal quadrupolar impedance and 7.5(e) the vertical quadrupolar impedance.
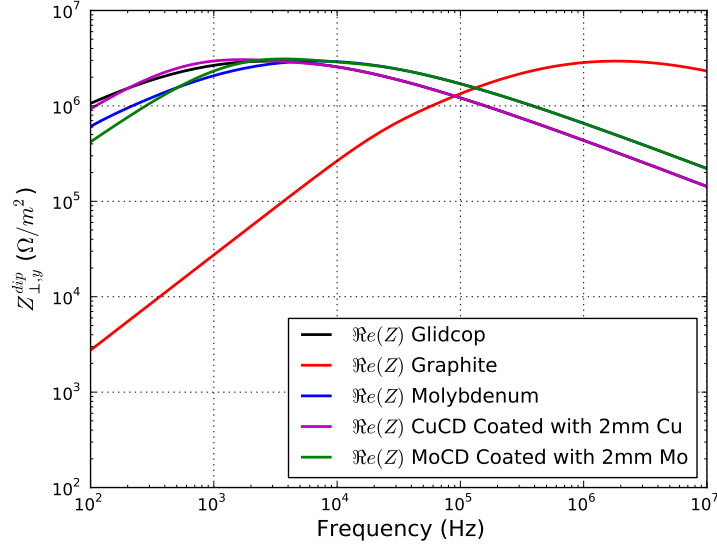
Figure 7.6: The real component of the vertical dipolar impedance of the various collimator jaw materials assuming a 2mm half gap.

component of the transverse impedance (dipolar and quadrupolar) above 10^3 Hz. By comparison to the change in tune shift discussed in Sec. 3.2.1 it can be seen that this reduces the magnitude of the imaginary component of the tune shift - i.e. the change in betatron tune is reduced.

Conversely, the peak of the real component of the transverse impedance is moved to lower frequencies as the conductivity of the innermost jaw material increases (shown in greater magnitude for the vertical dipolar impedance in Fig. 7.2.1). Importantly, this causes the high conductivity jaw materials to present a larger real component of the impedance in the important frequency range from $10^4 - 10^5$ Hz. Reviewing Sec. 3.2.2 it can be seen that this produces an decrease in the growth time.

7.3   TCTP Impedance Studies

As part of the ongoing collimation upgrade in the LHC, several advances in the LHC design have been proposed. These are as follows:

1. For the reasons given in Sec. 7.2, the jaw material of the collimators, specifically the secondary collimators is under review in an effort to reduce the beam impedance, improve cleaning efficiency and continue the present robustness and excellent performance of the LHC collimation system.

2. The inclusion of on collimator BPMs. This is due to the present method of alignment of the collimators relying on investigating the beam loss patterns in the LHC as a function of collimator aperture being a very time intensive procedure due to the inherentl slow natyure of beam loss. The use of on collimator BPMs allows a near instantaneous feedback on the position of the beam relative to the collimator jaw thus greatly increasing collimator setup time[cite setup paper gianluca/on collimator BPM paper]

3. A new RF system (Shown in Fig. 7.1) to reduce the side effects of the sliding RF contacts used in the phase 1 collimators.

As part of the upgrade, a series of TCTP collimators shall be installed in the LHC in replacement of a number of tertiary collimators (TCTs). In total, 8 TCTP and 1 TCSG will be added to the LHC. These collimators are in part intended to act as a test for two of these upgrades, the use of on collimator BPMs and the new RF system[cite collimators with onboard BPMs]. As part of the ongoing effort to limit increases to the LHC machine impedance (shown in Tab. 7.2) and due to continuing concerns about beam-induced heating [cite cham/evian 2012], all new devices to be placed in the LHC must be examined for their effect on the beam and as a possibly luminuousity limiter in the LHC. Due to the large number of phase 2 secondary collimators that are planned to be put in the LHC (30 additional secondary collimators to be installed during long shutdown 2[cite eucard report]) it is vital that the new collimator design, especially the new RF system is verified for it's efficacy as an impedance reduction technique.

Table 7.2: The impedance budgets (both transverse and longitudinal) for LHC. Taken from the LHC Design Report[cite LHC design report 2003-2004]

Beam Operation	Longitudinal $\Im m(Z_\parallel/n)$ (Ω)	Longitudi
Total Broadband at injection (450GeV)	0.07	
Total Broadband at collisions with squeezed optics (7TeV)	0.076	

(a)   (b)
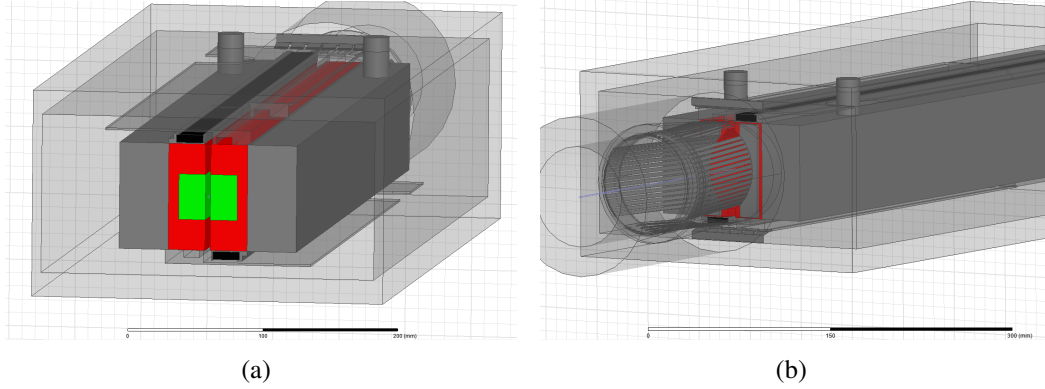
Figure 7.7: The TCTP collimator has a number of important impedance reduction techniques present in its design. The RF system, 7.7(a), replaces the sliding RF contacts of the phase 1 design, using ferrite tiles (shown in black) to reduce the resonant Q of the structure. The longitudinal RF fingers, shown in 7.7(b), provide a good conducting path for the beam image current in the transition from the beam pipe to the collimator jaw.

7.3.1 TCTP Collimator - Design and Geometry

The TCTP is a tertiary type collimator with a jaw made of tungsten. The principle components of interest from a beam impedance reduction point of view are the longitudinal RF fingers that cover the transition from the beam pipe to the collimator structure, and the RF system utilising ferrite blocks and a screen structure, shown in Fig. 7.7(a).

The RF system is designed to work in the following way, where comparison is given to the phase 1 RF system to clarify the differences and the design choices made. The phase 1 sliding contacts adequately masked the surrounding vacuum cavity from the beam, causing the resonant modes of the structure to be dominated by the geometry of the internal structure of the collimator jaw. Due to the small dimensions this volume the resonant frequencies are thus very high (in the realm of gigahertz) where the beam spectrum is very small and thus the beam-structure interaction is relatively small thus avoiding both impedance driven instabilities due to cavity modes and beam-induced heating. However the sliding contacts are believed to produce a large quantity of dust which is problematic for beam losses.

Conversely, the TCTP RF system removes the sliding contacts to remove the dust problem. This allows the beam to 'see' the entire vacuum tank of the collimator. This increases the characteristic dimensions driving the resonant frequency modes, thus lowering the minimum frequency of the cavity modes. This moves the frequency of the cavity modes into an area over the beam power spectrum where the spectrum is comparable to the DC beam current in the machine. To counteract this the Q of the cavity modes is reduced by the placement of ferrite tiles in the device to act as a damping material. This strongly reduces the peak height of the impedances thus reducing their effect on both instability and beam-induced heating.

7.3.2 Impedance Simulations and Results

The impedance of the TCTP collimator is examined through the use of simulation codes. In order to verify the simulation results it was decided to use both a time domain and a

(a)(b)(c)

Figure 7.8: The different RF systems considered for the TCTP collimator. 7.8(a) shows an RF system similar to the phase 1 RF system. In these simulations the sliding RF contacts are replaced by a perfect connection - for frequencies lower than 2-3GHz this is a good approximation and greatly simplifies the simulation model. 7.8(b) shows the RF circuit complete with ferrite. 7.8(c) shows the phase 2 RF circuit but without any ferrite present.

frequency domain code, in this case CST Particle Studio[cite] for the time domain and Ansoft HFSS[cite] for the frequency domain. Due to the reduced simulation time for time domain simulations compared to frequency domain simulations (which must be evaluated mode by mode to correctly evaluate the eigenmodes), the preliminary comparisons are done using the time domain code and the most promising solutions are subsequently investigated in depth using the frequency domain model.

For this comparison we investigate a number of different designs of the RF system for comparison to the ferrite damping solution chosen for construction;

1. The phase 1 sliding RF contacts, to provide comparison to the existing RF system. Shown in Fig. 7.1.

2. The proposed RF system including the ferrite damping tiles and the RF screen as shown in Fig. 7.1.

3. The proposed RF system without the ferrite damping tiles. This is too investigate the benefit of including the ferrite tiles.

The three different systems are shown in Fig. 7.3.2.

7.3.3 Beam-Induced Heating

As seen in Sec. 7.3.2, the longitudinal impedance of the phase 2 RF design indicates a significant number of beam impedance resonances below 1GHz. Although their contribution in the imaginary component of the beam coupling impedance is not significant enough to be of concern from a stability point of view, the resonances may present a problem from the point of view of beam-induced heating. To fully investigate both the effectiveness of

the ferrite in damping the cavity resonances and to identify the locations of the power loss the phase 2 structure is investigated using the frequency domain code HFSS.

For these simulations we simulate half of the structure (due to the reflective symmetry in the longitudinal plane), using alternatively perfect E-field (enforcing perpendicular electric fields at the boundary) and H-field (enforcing perpendicular magnetic fields at the boundary) boundary conditions at the symmetry plane to indentify and characterise the eigenmodes up to 2GHz (to cover the majority of the beam spectrum). The structure with and without ferrite is simulated to characterise the effect of the ferrite in damping the cavity modes. Simulations are carried out using the following parameters:

- Using a 2nd order basis function solver to ensure good resolution of the fields for R/Q and localised loss calculations.

- The ferrite is assumed to be 4A4, materials data is imported from an external data file and interpretted fit is used between data points. An analytical model (see [cite entry] for details).

- We simulate using a single jaw seperation, in this case a half-seperation of 2mm. This is an extremely close jaw seperation, closer in fact than the TCTP collimator would be placed at, but similar to that that the phase 2 collimators would be placed at. This allows some prediction of a worst case scenario for the TCTP and also an analysis of the efficacy of the RF system for the type of operational parameters the phase 2 secondary collimators would be placed at.

- The mesh was auto-generated by the HFSS mesh generator, and run for a convergence criteria of a 0.5% convergence of the eigenmode frequency between two successive meshes with a 30% refinement of the mesh between successive solutions.

Here we shall evaluate the resonances as a whole, or a few key resonances from a heating point of view. For a complete listing of the eigenmodes please see App. **??** for a complete breakdown of the TCTP eigenmode simulations. To have a comprehensive review of the heating we consider the following heating possibilities
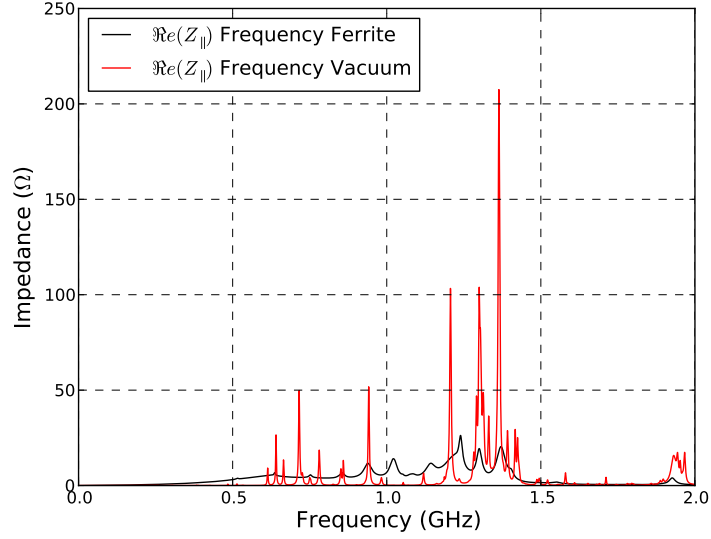
Figure 7.9: The real component of the longitudinal impedance for the TCTP collimator as simulated by both the time and frequency domains for the case with and without ferrite damping tiles. The strong resonances present in the case without ferrite can be seen to be strongly damped when the ferrite tiles are added. However a substantial broadband component occurs in addition due to the broadened resonance peaks.

- A beam harmonic occuring exactly on the resonant frequency with a certain bunch profile. Here we consider gaussian and $\cos^2$ bunch profiles. Parameters for a number of different beam operating modes (summarised in Tab. 7.3) are considered.

- Taking theoretical spectra for both 50ns and 25ns bunch spacings. In this case we consider the heating for both nominal operational parameters (1ns bunch length), running conditions from 2012 (bunch length between 1.2-1.4ns) and for HL-LHC parameters. These parameters are summarised in Tab. 7.3. Different bunch profiles are considered - gaussian and $\cos^2$ to account for high frequency lobes observed in measured beam spectra.

- Using measured multi-bunch spectra for 50ns bunch spacing measured in the LHC. These measurements are for the beam from injection, through the ramp to squeeze and finally collisions.

The heating estimates assuming on resonance beam harmonics can be seen in Tab. 7.3.3

129

Table 7.3: The LHC operational parameters considered for heating estimates for the TCTP. Operational parameters include the nominal LHC parameters for 25ns bunch spacing, the peak operational intensity for 50ns bunch spacing used in 2012, and the two possible HL-LHC operational schemes, using both 25ns and 50ns bunch spacing. Here the bunch length is assumed to encompass the 4σ gaussian width.

Operational Mode	τ_b (ns)	t_{bunch} (ns)	N_b	$n_{bunches}$
50ns, 2012 LHC Operation	1.2	50ns	1.7×10^{11}	1380
25ns, Nominal LHC Operation	1.0	25ns	1.15×10^{11}	2808
HL-LHC 25ns	1.0	25ns	2.0×10^{11}	2808
HL-LHC 50ns	1.0	50ns	3.3×10^{11}	1380

Table 7.4: The power loss of a the TCTP collimator with ferrite for a number of operational modes in the LHC and HL-LHC assuming each cavity mode falls upon a beam harmonic. All losses are in watts using the parameters found in Tab. 7.3

τ_b (ns)	50ns, 2012		25ns nominal		50ns, HL-LHC		25ns, HL-LHC	
	$P_{loss,g}$	$P_{loss,c}$	$P_{loss,g}$	$P_{loss,c}$	$P_{loss,g}$	$P_{loss,c}$	$P_{loss,g}$	$P_{loss,c}$
1.0	5.6	14.2	10.6	27.0	21	53.4	32.2	81.8
1.1	3.8	10.2	7.2	19.6	14.4	38.8	22.0	59.0
1.2	2.6	7.4	5.0	14.0	10.2	27.8	15.4	42.2
1.3	2.0	5.4	3.6	10.0	7.2	20.0	11.0	30.4
1.4	1.4	3.8	2.6	7.4	5.2	14.6	8.0	22.2
1.5	1.0	2.8	2.0	5.4	3.8	10.8	5.8	16.4

for a variety of bunch lengths between 1-1.5ns assuming gaussian and $\cos^2$ bunch distributions. The same data for the TCTP without the ferrite damping tiles can be seen in Tab. 7.3.3. A number of things area immediately evident; The addition of the ferrite drastically reduces the power loss in the TCTP collimator, by a factor of ≈ 3. In addition, the consideration of the higher frequency lobes in the heating estimates for the TCTP is significant, as can be seen in Fig. 7.3.3. In this case the usefulness for the ferrites is clear.

Considering the heating taking beam harmonics seperated the inverse of the bunch seperation ($40MHz$ for $t_{bunch} = 25ns$ and $20MHz$ for $t_{bunch} = 50ns$) we acquire the

Figure 7.10: The beam-induced heating of the TCTP with ferrite damping tiles for a number of different bunch lengths assuming both a gaussian and $\cos^2$ distributions.

Table 7.5: The power loss of a TCTP collimator without the ferrite damping tiles for a number of operational modes in the LHC and HL-LHC assuming each cavity mode falls upon a beam harmonic. All losses are in watts using the parameters found in Tab. 7.3

τ_b (ns)	50ns, 2012		25ns nominal		50ns, HL-LHC		25ns, HL-LHC	
	$P_{loss,g}$	$P_{loss,c}$	$P_{loss,g}$	$P_{loss,c}$	$P_{loss,g}$	$P_{loss,c}$	$P_{loss,g}$	$P_{loss,c}$
1.0	2.8	7.1	5.3	13.5	10.5	26.7	16.1	40.9
1.1	1.9	5.1	3.6	9.8	7.2	19.4	11.0	29.5
1.2	1.3	3.7	2.5	7.0	5.1	13.9	7.7	21.1
1.3	1.0	2.7	1.8	5.0	3.6	10.0	5.5	15.2
1.4	0.7	1.9	1.3	3.7	2.6	7.3	4.0	11.1
1.5	0.5	1.4	1.0	2.7	1.9	5.4	2.9	8.2

Table 7.6: The power loss of a TCTP collimator with ferrite for a number of operational modes in the LHC and HL-LHC assuming beam harmonics spaced at the reciprocal of the bunch spacing. All losses are in watts using the parameters found in Tab. 7.3

τ_b (ns)	50ns, 2012		25ns nominal		50ns, HL-LHC		25ns, HL-LHC	
	$P_{loss,g}$	$P_{loss,c}$	$P_{loss,g}$	$P_{loss,c}$	$P_{loss,g}$	$P_{loss,c}$	$P_{loss,g}$	$P_{loss,c}$
1.0	19.0	36.2	18.2	35.0	71.6	136.8	54.8	104.6
1.1	14.8	29.2	14.2	28.0	56.2	110.0	42.8	85.0
1.2	11.8	23.6	11.2	22.6	44.8	89	34.0	68.6
1.3	9.6	19.2	9.0	18.4	36.2	72.6	27.4	55.6
1.4	7.8	16.0	7.4	15.2	29.4	60.0	22.2	45.8
1.5	6.4	13.2	6.0	12.6	24.2	50.0	18.4	38.0

results presented in Tab. 7.3.3 and Tab. 7.3.3 respectively, again for a variety of LHC operational parameters and assuming either a gaussian or a $\cos^2$ longitudinal bunch profile. In this case it can be seen that the power loss for the ferrite case is larger than that experienced by the case without ferrite. This can be understood due to the fixed frequencies of the beam harmonics - if a high-Q resonance does not occur at or near a beam harmonic then the beam does not couple to the resonance. Due to the broad resonance peaks of the ferrite damped TCTP design the beam may couple to the resonance even if the resonance frequency of the cavity mode does not match the beam harmonic precisely due to the low-Q of the resonance.

Table 7.7: The power loss of a TCTP collimator without ferrite for a number of operational modes in the LHC and HL-LHC assuming beam harmonics spaced at the reciprocal of the bunch spacing. All losses are in watts using the parameters found in Tab. 7.3

τ_b (ns)	50ns, 2012		25ns nominal		50ns, HL-LHC		25ns, HL-LHC	
	$P_{loss,g}$	$P_{loss,c}$	$P_{loss,g}$	$P_{loss,c}$	$P_{loss,g}$	$P_{loss,c}$	$P_{loss,g}$	$P_{loss,c}$
1.0	2.8	7.1	5.3	13.5	12.1	25.0	16.1	40.9
1.1	1.9	5.1	3.6	9.8	7.2	19.4	11.0	29.5
1.2	1.3	3.7	2.5	7.0	5.1	13.9	7.7	21.1
1.3	1.0	2.7	1.8	5.0	3.6	10.0	5.5	15.2
1.4	0.7	1.9	1.3	3.7	2.6	7.3	4.0	11.1
1.5	0.5	1.4	1.0	2.7	1.9	5.4	2.9	8.2

(a)(b)

Figure 7.11: The different thermally sensitive components of the TCTP collimator. 7.11(a) shows the ferrite tiles, and 7.11(b) the longitudinal RF fingers.

Location of Power Deposition

Due to the poor cooling available in vacuum (cooled by radiative heating only. Although surrounded by a housing/in contact with surrounded components, the thermal contact between different components within the collimator is poor) it is important to know of the proportion of beam-induced power loss that is lost in thermally sensitive areas. These are areas where large increases in temperature can either lead to direct physical damage (as is the case with RF fingers) or may lead to a worsening physical condition of the collimator (if the ferrite tiles go above their Curie temperature). The components are highlighted in Fig. 7.3.3

The losses on or in different surfaces and volumes is calculated using the loss calculations within HFSS, and then normalised to the total losses in the TCTP structure for each mode. The produces a variety of losses depending on the field pattern of the mode. These are collated in App. **??**. To provide a conservative estimate of the power load we take the highest proportions of power loss of all the modes and assume this is the case for all modes. The percentages for the total device, the ferrite tiles and the longitudinal RF fingers are shown in Tab. 7.3.3.

Table 7.8: The percentage of power loss lost in thermally sensitive components in the TCTP.

Component	Percentage of Power Loss
Whole Device	100
Ferrite Tiles	5
Longitudinal RF Fingers	4

Table 7.9: The power loss in the ferrite of the TCTP collimator. The most pessimistic of the losses estimated in Tab. 7.3.3 and Tab. 7.3.3 for the 1.0ns case. All losses are in watts using the parameters found in Tab. 7.3

τ_b (ns)	50ns, 2012 $P_{loss,c}$	25ns nominal $P_{loss,c}$	50ns, HL-LHC $P_{loss,c}$	25ns, HL-LHC $P_{loss,c}$
1.0	1.8	1.7	6.8	5.2

The thermal behaviour as a result of this power load can be analysed using design software such as ANSYS[cite]. The results of these thermal simulations can be seen in [cite F. Carra/M. Garlasche colwg meeting], a summary of which is given in Fig. 7.3.3. The important figure of merit is in whether the temperature of the ferrite increases beyond its Curie temperature. For the TT2-111R, this 375°C[cite data sheet]. The power loss for the worst cases of the nominal, HL-LHC and HL-LHC parameters without crab cavities (bunch length 0.5ns rather than 1.0ns) is considered, in this case with a factor of two margin of error included to be conservative (i.e. we assume double the power on the ferrite tiles), and it can be seen that the temperature increase for even the worst case results in the temperature being significantly below the Curie temperature for this material.
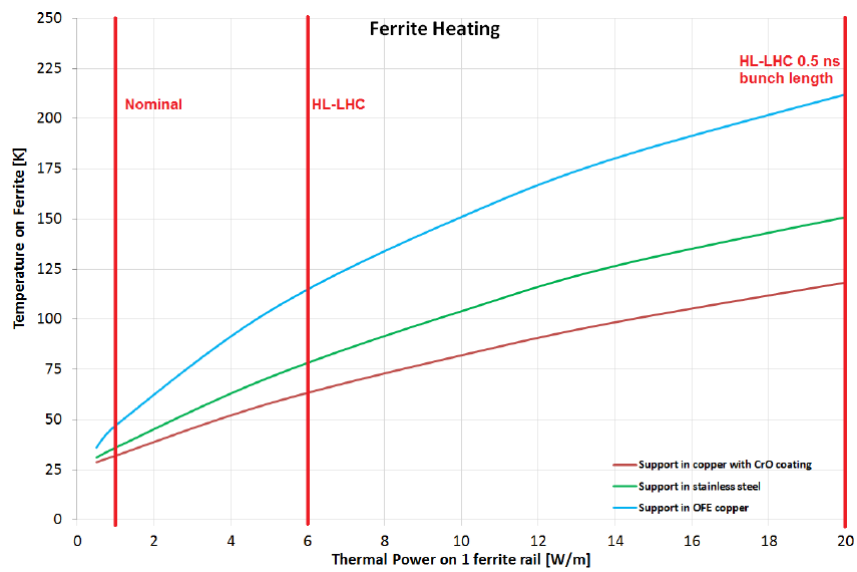
Figure 7.12: The temperature increase of the ferrite damping tiles in the TCTP collimator under a number of beam operating conditions and for a number of different jaw support materials. Plot taken from [cite Carra and Garlasche].

Chapter 8

LHC Injection Kicker Magnet

The injection kicker magnets in the LHC are part of the injection system for the LHC machine. This system is used to match the trajectory of the injected beam to that of the stable beam path in the accelerator. An example schema for the LHC can be seen in Fig. 8. The system typically uses two components, a septum, which may provide a slowly rising and falling time, but strong, field, and kickers, which may provide a rapidly rising and falling, but comparatively weak field, to match the injected beam to the correct trajectory. Similar components are used for the extraction of beam also.

By design kickers must always be visible to the beam due to the need to quickly fire to apply their kick. In addition the need for a highly homogeneous field whilst the kick is applied, as well as the strength of the field neccesitates that the aperture for kickers often be very narrow, meaning they are in close proximity to the beam. This leads to two concerns - that the close proximity of the beam to a device that may be made of either a highly lossy material [cite ferrite kicker magnets] or of a source of strong geometrical impedance [cite stripline kickers] may be source of impedance that drives instabilities in the beam [impedance of the SPS], and secondly that the large real component of ferrite kicker magnets may be subject to intense heating in high beam current machines [cite beam induced heating in the SPS MKEs].

Figure 8.1: An example layout of a injection system for an accelerator.

Figure 8.2: The location of the LHC injection systems in the LHC ring.

(a)(b)

Figure 8.3: 8.3(a) A cross section of an MKI. Visible are the alternating HV and ground plates, seperated by capacitor plates. The HV drive plate and the ground return can be seen in the c core of the ferrite yoke. 8.3(b) shows an MKI in it's vacuum tank.

8.1   LHC Injection Kicker Magnets

The LHC injection kicker magnets (LHC-MKIs, or MKI) are a 3m long travelling wave transmission line kicker magnet (ferrite length 2.7m). For LHC there are two injection regions, at near IPs 2 and 8, each consisting of an septa system and four MKIs injecting vertically into the machine (The position of the LHC injection systems is shown in Fig. 8.1). As a transmission line magnet the magnet is constructed of a c-core ferrite yoke, segmented by alternating HV and ground plates capacitively coupled together by ceramic capacitor plates. The pulse is generator in a pulse forming network (PFN), stationed above ground, which is subsequently carried by a cable with a characteristic impedance of 5Ω, matching the characteristic impedance of the MKI. The performance parameters of the magnets rise time, fied strength and homogeneity are given in Tab. 8.1[cite].

Table 8.1: MKI Operational parameters

Number of Kickers per System	4	
Kick strength per magnet	0.3	T.m
Magnet beam aperture (diameter)	38	mm
Characteristic Impedance	5	Ω
Operating charging voltage (PFN)	54	kV
Field flat top ripple	$< \pm 0.5$	%
Field flat top duration	up to 7.86	μ s
Field rise time 0.5%-99.5%	0.9	μ s
Field fall time 99.5%-0.5%	3.0	μ s
Magnet kength	2.7	m

8.1.1 Development of the LHC-MKI Beam Screen

??

During the commissioning of the CERN accelerator complex for LHC type beam with 25ns, 50ns and 75ns bunch spacing, drastic heating and outgassing was observed in the SPS extraction kicker magnets (MKEs) [cite PAC paper]. During an extensive measuring campaign, it was deduced that this was due to extensive beam-induced heating due to the large real component of the longitudinal impedance of the MKEs. Subsequently a number of retroactive impedance reduction methods were proposed and evaluated for their effectiveness in reducing the longitudinal impedance[cite Kroyer et co.].

These experiences motivated some debate on the need for a beam screen for the LHC-MKIs [cite Vos paper/Caspers], which ultimately was implemented in the final design. The beam screen is composed of a ceramic pipe housing up to 24 screen conductors - conductive wires which extend the length of the magnet, connected directly to the LHC beam pipe at one end, and capacitively coupled at the other. A scheme involving printed conductive strips on the inside surface of the ceramic was considered but was not implemented due to extensive tracking and electrical breakdown between the strips during firing of the kickers. The capacitive coupling is required due to the short rise time requirement of the kicker field - direct connections at both ends would create a faraday cage, causing the characteristic rise time of the system to dramatically increase. In this case electrical simulations indicate that this must be the pulse input end, i.e. the upstream end of the kicker[cite the beam screen mki]. This will become relevent during the evaluation of heating patterns of the MKI during operation.

The use of the capacitive coupling gives rise to a discontinuity of the conducting path of the beam image current. This gives rise to the possibility of exciting resonances in the surrounding structure of the image current path. In this case, resonant modes of a characteristic frequency due to the screen conductors acting as $n\lambda/4$ resonators. To damp these low frequency modes (the screen conductors are some 3m in length), a series of ferrite (NiZn) toroids is placed at each end of the beam screen to damp these modes [cite].

During testing and conditioning of the MKIs it was discovered than there was still significant electrical breakdown/sparking occuring during firing. Electrical simulations and measurements indicated that above a PFN voltage of 30kV large quantities of discharge were observed originating from the screen conductors. In particular, the highest voltage was found to occur on the screen conductors closest to the HV busbar [cite improved beam screen]. Due to the operational voltage requirements a solution had to be found. It was decided to remove the screen conductors exposed to the highest voltages (those closest to the HV busbar) in an effort to reduce the number of discharges. Experiments showed that removing the 9 conductors closest to the HV busbar increased the PFN voltage reached before discharges began to 57kV, above the required 54kV to meet the design parameters for the MKI. Measurements demonstraed that this would worsen the longitudinal beam impedance but this was determined to not be large enough to pose a problem from the point of view of beam induced heating[cite improved beam screen].

8.1.2 Observations of heating during 2011 and 2012 until Technical Stop 3

Beginning with the increasing intensity in the LHC during operation in 2011 a number of devices within the LHC were observed to be heating [Evian/Mini-Cham/Chamonix 2012]. Observations and calculations demonstrated a strong relationship between the observed heating and the increasing intensity (first the number of bunches, then the increase in bunch population) indicating that the source of the heating was due to the stored beam interacting strongly with the impedance of many structures - evidenced also by the deteriorating vacuum in vacuum sensitive components also. A number of key devices were observed to be exposed to significant heating, in particular devices around the injection region (injection projection collimators, injection kickers, VMTSA (a two beam vacuum interconnect in the injection region)) and some small insertion devices (ALFA roman pot), as explained at the Evian 2011 workshop[cite] and Chamonix 2012[cite]. Examples of this heating for a number of devices in 2011 are shown in Fig. 8.1.2.

Figure 8.4: The heating of a number of devices during 2011 in the LHC.

(a)(b)

Figure 8.5: The heating of the MKIs at 8.5(a) IP2 and 8.5(b) IP8 during 2011 in the LHC. Note MKI8b and MKI8d experience significantly more heating than the other MKIs.

The heating of the LHC-MKIs in particular is shown in Fig. 8.1.2. Some important notes about the heating can be made, firstly that MKIs 8b and 8d both experience the strongest heating, MKI8d in particular demonstrating much higher heating, experiencing temperatures $\approx 20°$C higher than that experienced by the other MKIs. Secondly, that the time constants of the temperature is very long (on the order of 25 hours [cite]), indicating a large portion of the tank is heating, and additionally that if the temperature reached is detrimental to magnet operation, the neccesary cool-down time will be substantial enough to effect machine operational schedules. It can also be seen that the peak temperature only gets worse as the beam intensity is increased.

The temperatures in MKIs are measured using 4 PT-100 thermacouples, placed in the beam pipe up and down stream, and on the outermost ground plates up and down stream, shown in Fig. 8.1.2. Due to the component of concern in the MKI being the ferrite yoke of the kicker but there being no direct temperature measurement on this component, one difficulty in analysing the heating of the MKI is to identify the temperature of the ferrite yoke which corresponds to which temperature at the points of measurement. This is a problem which has been analysed in depth in [cite - temp in mki ipac2012 and mki strategy meeting], in particular using field strength from kicks under a softstart condition (the firing of the magnet with no beam to inject), and inferences from both the kick strength measured in correspondance to the temperatures, and the rise time of the kicker field. Current analysis has given a certain margin of safety to the current interlock level, but due to the possible damage that may be done due to a misinjection of the beam this is very conservative, still requiring a few hours of cool down time between injections[cite mki strategy meeting].

Prior to technical stop 3 in 2012 there were 2 configurations of the beam screen in

Figure 8.6: The location of the temperature measuring thermacouples in the MKI. The upstream end is towards the capactive coupling end of the beam screen.

the LHC-MKIs - 7 MKIs are in place with 15 tapered screen conductors, the 9 screen conductors closest to the HV busbar having been removed due to the electrical breakdown concerns mentioned in Sec. **??**. A single MKI, MKI8c is fitted with 24 screen conductors, 15 tapered as in the other MKIs, and 9 shortened screen conductors (trimmed such they do not overlap with the external metallization at the capacitively coupled end). This was found to reduce the induced voltage in the screen conductors closest to the HV busbar, but not significantly improve the beam coupling impedance of the MKI.

8.2 Simulations and Measurements of the MKI with 15 Screen Conductors

To begin an analysis of the heating of the MKIs, and to verify the use of simulations as a tool for evaluating different designs of the MKI impedance reduction methods it was important to measure an existing MKI configuration as a benchmark. Due to the expected low beam coupling impedance of the MKI even with 15 screen conductors (on the order of 100Ω longitudinal beam coupling impedance) it was decided to do the measurements using the resonant coaxial wire method, described in Sec. 4.1.2. This method limits the frequency resolution of the measurements ($\Delta f = c/\Delta\lambda = c/2L_{device} \approx 40MHz$ where c is the speed of light and $L_{device} \approx 3.5m$ is the length of the MKI in it's vacuum tank), but the added accuracy in this measurement is considered appropriate in this case.

The measurements were carried out on a fully assembled MKI inside it's vacuum tank, with a beam screen housing 15 tapered screen conductors. For the single wire measurements a copper wire of radius 0.5mm was placed in the central beam pipe, suspended on a vacuum flange modified to take a Sucobox connection allowing a capacitor housed in a seperate sucobox to be attached to the connecting box (The experimental setup is shown

(a)(b)

Figure 8.7: The measurement setup of the coaxial wire measurements of an LHC-MKI. Shown is the vacuum tank with connecting N-type cables 8.7(a) and a coupling capacitor in it's associated Sucobox 8.7(b).

in Fig. 8.2). To displace the wire for displaced single wire measurements, a pair of nylon screws (one at each flange) were used to physically displace the wire. Displacements were taken at 3mm intervals in both the vertical and horizontal planes, between -9mm and +9mm displacement.

For the two wire measurements, two wires were suspended in the device, seperated by 7mm. The wires were connected to a single VNA, each connection run through a 180° hybrid to generate the appropriate phase difference between the two. The experimental setup for the two wire measurements is shown in Fig. 8.2.

The VNA is calibrated using an 8532E calibration kit, using an IF bandwidth of 1kHz. 2000 equally space data points are used over a frequency range of 1MHz-2GHz. The Q factors and resonant frequencies of the resonant modes are calculated using a peak finding algorithm on the VNA, and the conductive losses due to the copper wire calculated analytically and compensated for.

The simulations of the MKI are carried out using CST Particle Studio, a time domain simulation code. A simplified model of the magnet is created, shown in Fig. 8.2. An integrated wakelength of 15m is used in the simulations, and a simulated bunch of a gaussian profile with σ_z =45mm used. A half model is used for displacements of the source/integration path in the vertical axis due to the symmetry plane in the y-z plane, giving a mesh count of $\approx$ 16 million for vertically displaced simulations and $\approx$ 16 million for horizontally displaced simulations. To acquire the dipolar and constant impedance terms, the source signal is displaced whilst the path of integration is kept on axis. The linear variation in the resulting impedance can be seen to be the dipolar term and the constant impedance the constant term. Similarly for the quadrupolar term the source signal is kept on axis and the

The results for the measurements be seen in the following figures:

Figure 8.8: The measurement setup for the two wire measurement setup. The 180° hybrid can be seen on top of the vacuum flange.

Figure 8.9: The simulation model of the LHC injection kickers implemented in CST Particle Studio.

1. Fig. 8.2 the longitudinal impedance

2. Fig. 8.11(a) the horizontal dipolar impedance

3. Fig. 8.11(b) the vertical dipolar impedance

4. Fig. 8.12(a) the horizontal quadrupolar impedance

5. Fig. 8.12(b) the vertical quadrupolar impedance

6. Fig. 8.13(a) the horizontal constant impedance

7. Fig. 8.13(b) the vertical constant impedance

It can be seen that there is generally good agreement between the measurements and simulations in all planes. In particular the agreement for the real component of the longitudinal impedance between measurements and simulations is exceptionally good below 1.5GHz. This is considered an important verification of the simulation model as this is the impedance of greatest concern presently due to beam-induced heating. Discrepencies can be seen in the longitudinal measurements above 1.5GHz - this is likely due to differences between the internal structure of the magnet and that represented by the simulation model.

8.2.1   Beam Induced Heating Estimates for 15 Screen Conductors

It can clearly be seen from the measurements of the real longitudinal impedance (8.2) that there is a significant broadband impedance to the structure which could a cause of beam induced heating. This strongly indicates that the removal of the 9 screen conductors

Figure 8.10: The longitudinal impedance of the LHC MKI acquired by measurements using the resonant coaxial wire method and time domain simulations using CST Particle Studio.

(a)(b)

Figure 8.11: The dipolar impedances of the LHC MKI acquired by measurements using the resonant coaxial wire method and time domain simulations using CST Particle Studio. 8.11(a) shows the horizontal dipolar impedance, and 8.11(b) the vertical dipolar impedance

(a)(b)

Figure 8.12: The quadrupolar impedances of the LHC MKI acquired by measurements using the resonant coaxial wire method and time domain simulations using CST Particle Studio. 8.12(a) shows the horizontal quadrupolar impedance, and 8.12(b) the vertical quadrupolar impedance

closest to te HV busbar has drastically decreased the screening of the ferrite from the beam image current.

To provide a first estimate of the expected heating of the MKI it is neccesary to estimate the power loss in the MKI. Taking the simulation impedance (due to allowing a finer resolution of frequency) the power is estimated using the broadband method of heat calculation given in Sec. **??**. For these calculations we consider the operational parameters for the 2012 proton run in the LHC, summarised in Tab. 8.2.1. Estimates for longitudinal profiles of gaussian, parabolic and $\cos^2$ profiles assuming bunch lengths between 1.0 and 1.4ns are shown in Tab. 8.2.1. The thermal evolution of the MKI with this power load (assuming all the power is lost on the ferrite yoke for a worst case scenario) has by evaluated extensively by Garlasche et al [cite], and has been found to be compatible with the measured temperature of the MKI thermal probes [cite MKI Strategy Meeting/IPAC'12]. As a response to this the interlock temperature was increased a number of times during 2011 and 2012 to take account of the expected internal temperature of the ferrite in relation to the measured temperature at the location of the temperature probes. In particular

(a)(b)

Figure 8.13: The constant transverse impedances of the LHC MKI acquired by measurements using the resonant coaxial wire method and time domain simulations using CST Particle Studio. 8.13(a) shows the horizontal constant impedance, and 8.13(b) the vertical constant impedance

Table 8.2: The 2012 LHC operational parameters used for estimating the power loss in the MKI with 15 screen conductors.

Bunch Spacing	50	ns
Number of bunches	1380	
Particles per bunch	1.7×10^{11}	

Table 8.3: Power loss estimates for the LHC-MKI with 15 screen conductors in the beam screen.

Bunch Length (ns)	$P_{loss,gaussian}$	$P_{loss,parabolic}$	P_{loss,cos^2}
1.0			
1.1			
1.2			
1.3			
1.4			

the measurement of the magnetic field parameters of the fired kicker (rise time, ripple and field strength) during the so called soft-start regime (firing the kicker with no beam) have provided accurate relations between the measured temperature and the ferrite yoke temperature [cite Barnes IPAC12].

It has thus been shown that the power loss due to the beam induced wakefields into the MKI can describe the temperature behaviour seen during 2011 and 2012 operation, giving us confidence in our understanding of the sources of and heating processes occuring within the MKI. To propose workable improvements to the beam screen, it is first neccesary to understand both the sources of the impedance due to the beam screen layout and the limitations that both manufacturability and the electrical potential build up on the screen conductors produces. In addition other methods of increasing decreasing both the power load and of improving the rate of cooling of the kicker are complementary avenues of study to reduce the problem of beam-induced heating in the MKIs, the problem ultimately being the high temperature of the ferrite yoke.

8.3 Other Concerns for the MKI Operation and Temperature Reduction

Given the breadth of concerns that must also be considered alongside beam impedance when discussing the heating of the MKIs and alterations to the beam screen design it is suitable to include a brief discussion on these matters here.

First of the concerns is the induced electrical potential in the screen conductors during the firing of the kicker magnet. It is due to this high induced voltage (up to 45kV on the conductor closest to the HV busbar) and the resulting sparking/electrical breakdown between screen conductors and to the end of the beam screen at the capacitively coupled end that were the initial motivation to remove the 9 screen conductors from the beam screen. The reasoning for this was that sparking produces vacuum spikes, can cause the decay of the screen condition and may be a source of UFOs (unidentified falling objects - microscopic dust particles that drop through the beam causing spikes in beam losses due to scattering, resulting in the beam being dumped).

In addition to improving the screening of the ferrite yoke from the beam any proposed beam screen design must also allow the PFN to be fired at the desired voltage (54kV from the technical specifications). Work by Barnes et al [cite MKI strategy meeting] has found there are a number of factors that can reduce the induced potential on the screen conductors. These include the use of elongated spheres on the ends of the screen conductors to reduce the high electric fields at the ends of the screen conductors (Fig. **??**), alternating the length of the screen conductors (Fig. **??**) and replacing the metallization with a cylindrical metal tube away from the surface near the areas of overlap between the screen conductors and external metallization (Fig. **??**). The aim of this last measure is to remove the external ground further away from the outside of the ceramic beam screen, as the metallization has been observed to force the ground plane closer to the screen conductors due to the high permitivitty of the ceramic beam screen. The effects of these changes on the beam coupling impedance are discussed in later sections.

The second major concern is the transfer of thermal energy out of the kicker magnets.

Due to the HV pulsed nature of the kicker magnet operation there is no active cooling within the device, thus cooling is reliant exclusively on radiative transfer of the heat from the components to the surrounding air via the vacuum tank. Experiments have shown that the internal surface of the vacuum tank has a very low emissivity in the IR range [cite M. Barnes], and subsequent thermal simulations have shown that the stable temperature of the MKI is very sensitive to the emissivity of the vacuum tank internal surface [cite M. Garlasche]. Subsequently a significant quantity of work has been carried out on methods to improve the emissivity of the internal surface of the vacuum tank [cite M. Barnes] so as to more effectively passively cool the device.

8.4 Simulations and Measurements of the MKI with 19 Screen Conductors

As can be seen from Fig. 8.5(b), MKI8d had experienced significantly higher temperatures than the other kicker magnets during operation. Although estimated to experience the same degree of power loss within the structure as the other kicker magnets (due to the similarity of the beam screen layout) the large variation in the emissivity of the internal surface of the vacuum tank can have contributed to the higher temperatures observed. As a result of this, and the necessity to find a solution to the high temperatures of the MKIs, which were acting as a severe limiter on the integrated luminousity delivered by the LHC, it was decided to implement an improved beam screen in a replacement magnet in an effort to reduce the power loss in this magnet, and at the same time test some of the principles of future alternative beam screen designs.

The following design features were implemented in the replacement MKI8d (explanations are given with the description):

1. 19 screen conductors are placed within the beam screen in order to improve the shielding of the ferrite from the beam. These are clustered together, with the 5 empty screen conductor slots closest to the HV busbar to minimise the induced

(a)(b)

Figure 8.14: Several components of the replacement MKI8d. **??** shows the layout of the screen conductors, and 8.14(b) shows the beam screen enlarged for the elongated spheres.

voltage on the screen conductors (shown in Fig. 8.14(a)). Both impedance and electrical simulations have indicated that this will drastically reduce the beam coupling impedance of the MKI, and that the PFN may fire at the operational voltage without inducing electrical breakdowns in the beam screen.

2. Elongated metal spheres are placed on the capacitively coupled end of the kicker magnet. These are intended to reduce the field amplification due to any sharp edges at the ends of the screen conductors, thus reducing the possibility of electrical breakdown. This method has some drawbacks due to the need to expand the slots housing the screen conductors to accept the larger elongated spheres (shown in Fig. 8.14(b)).

3. The screen conductors are arranged to alternate in length (i.e. there are two lengths of screen conductor in the beam screen, see Fig. 8.14(a)) to further reduce the induced potential on the screen conductors. The effect here is for the longer length screen conductors to effectively shield the shorter screen conductors, thus reducing the potential difference between neighbouring screen conductors.

Due to the primary motivation for altering the beam screen being the increasing beam-induced heating seen in the kicker magnets the impedance studies were primarily motivated by reducing the real component of the longitudinal beam coupling impedance. Simulations carried out prior to the construction of the magnet predicted that the beam-coupling impedance would be strongly reduced by the inclusion of 4 additional screen conductors. Measurements taken of the magnet confirmed these simulations to very good accuracy, and shown in Fig. 8.4 along with the measurements and simulations for an MKI with 15 screen conductors. It can be seen that the real component of the beam coupling impedance is reduced drastically across the entire frequency range of concern, and the predicted power loss as a result of the simulated impedance (shown in Tab. 8.4) shows
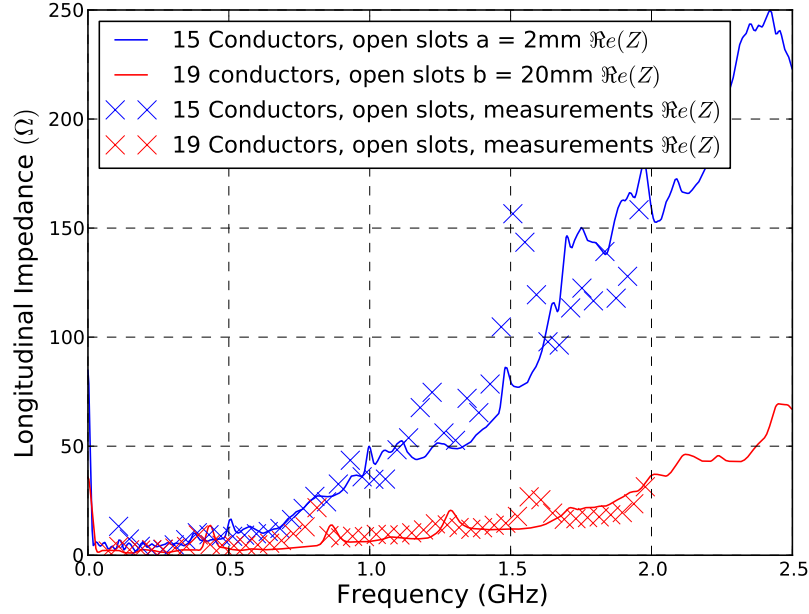
Figure 8.15: The real component of the longitudinal beam coupling impedance of the reaplcement MKI8d with 19 screen conductors from both simulations and measurements. The corresponding impedance for an MKI with 15 screen conductors is shown for comparison.

that the expected power loss in reduced by a factor of 2-3. Calculations of the thermal evolution of the proposed MKI8d replacement also indicated that the maximum temperature reached would decrease significantly due to this reduced power load[cite].

8.4.1 Temperature of MKI8d after Technical Stop 3

Due to the promising results of the impedance, electrical and thermal simulations of the proposed MKI8d replacement with 19 screen conductors it was decided to construct the replacement magnet and install it during technical stop 3 (TS3)[cite]. It is said the proof is in the pudding, and in this case mine is exceptionally tasty; Fig. 8.4.1 shows the temperatures for the kicker magnets at IP8 both before and after TS3. It can clearly be seen that MKI8d (solid red trace) changes from being the warmest magnet in IP8 - An excellent confirmation of the understanding of the sources of power loss within the kicker magnet and the thermal evolution due to the power loss. From these very promising results a great

Table 8.4: The power loss due to the impedance calculated for the MKI with 15 (most common configuration) and 19 (as for MKI8d) screen conductors. Estimates are given assuming a beam with 1380 bunches, seperated by 50ns, with each bunch containing 1.7×10^{11} particles. Estimates of the power loss assuming a gaussian, a parabolic and a $\cos^2$ longitudinal bunch profile are calculated, and a range given for the lowest (typically the gaussian distribution) and highest (typically the $\cos^2$ distribution due to the large high frequency lobes) values calculated.

Bunch Length (ns)	P_{loss} 15 Screen Conductors	P_{loss} 19 Screen Conductors
1.0	P_{loss} 15 Screen Conductors	P_{loss} 19 Screen Conductors
1.1	P_{loss} 15 Screen Conductors	P_{loss} 19 Screen Conductors
1.2	P_{loss} 15 Screen Conductors	P_{loss} 19 Screen Conductors
1.3	P_{loss} 15 Screen Conductors	P_{loss} 19 Screen Conductors
1.4	P_{loss} 15 Screen Conductors	P_{loss} 19 Screen Conductors

Figure 8.16: The temperature profile of the IP8 injection kicker magnets during the time period before and after technical stop 3 (TS3), when the MKI8d was changed from a kicker magnet with 15 screen conductors to one with 19 screen conductors. It can be seen this magnet (solid red trace) goes from being the hottest magnet to the coolest after TS3.

deal of confidence in the simulation tools for predicting the beam coupling impedance and the understanding of the causes of the beam coupling impedance were acquired. As such more significant changes to the MKI design

8.5 The Dependence of the Beam Coupling Impedance on The Kicker Components

As part of the study to improve the beam screen it was decided to investigate systematically the effect of the various commponents of the kicker magnet on the resulting beam coupling impedance. This is divided into two sections, the study of the effect of the beam screen on the beam coupling impedance of the ferrite yoke, and subsequently a study of the effects of the dimensions of the beam screen and screen conductors on the beam coupling impedance.

8.5.1 The Impedance of the MKI - Effects of the Inclusion of the Beam Screen

To first judge the effectiveness of the concept of the beam screen as an impedance reduction technique we simulate the MKI by systematically adding components to the magnet to determine their effect on the beam coupling impedance. We consider the following configurations of the MKI:

1. The c-core ferrite yoke

2. The c-core ferrite yoke with a ceramic cylinder inserted inside

3. As above but with 24 screen conductors inserted into the cylinder, capactively coupled at one end

4. The internal magnet structure including the vacuum tank, HV and ground plates and the surrounding connections.

These geometries are shown in Fig. 8.5.1, and the resulting impedance simulations for the real component shown in Fig. 8.5.1. Several points can be seen; firstly that the inclusion of the beam screen with screen conductors very effectively screens the beam from the other components of the kicker magnet - including the ceramic of the beam screen, the surrounding structures and the ferrite itself. This indicates that for a beam screen in which the ceramic tube holds a large number of screen conductors, the beam is effectively screened from the surrounding structure up to a frequency characterised by seperation of the screen conductors. This has benefits for the impedance simulations as it is valid to use a reduced simulation model considering just the capacitively coupled end provided we can assume the ferrite is well screened (i.e. we have 24 screen conductors in place). Secondly the inclusion of the ceramic beam pipe does not effectively screen the ferrite by itself - the screen conductors are necessary to correctly screen the surroundings. And lastly that the use of the ceramic beam screen contributes significantly to the imaginary component of the longitudinal impedance (evidenced by the linear increase of the imaginary impedance
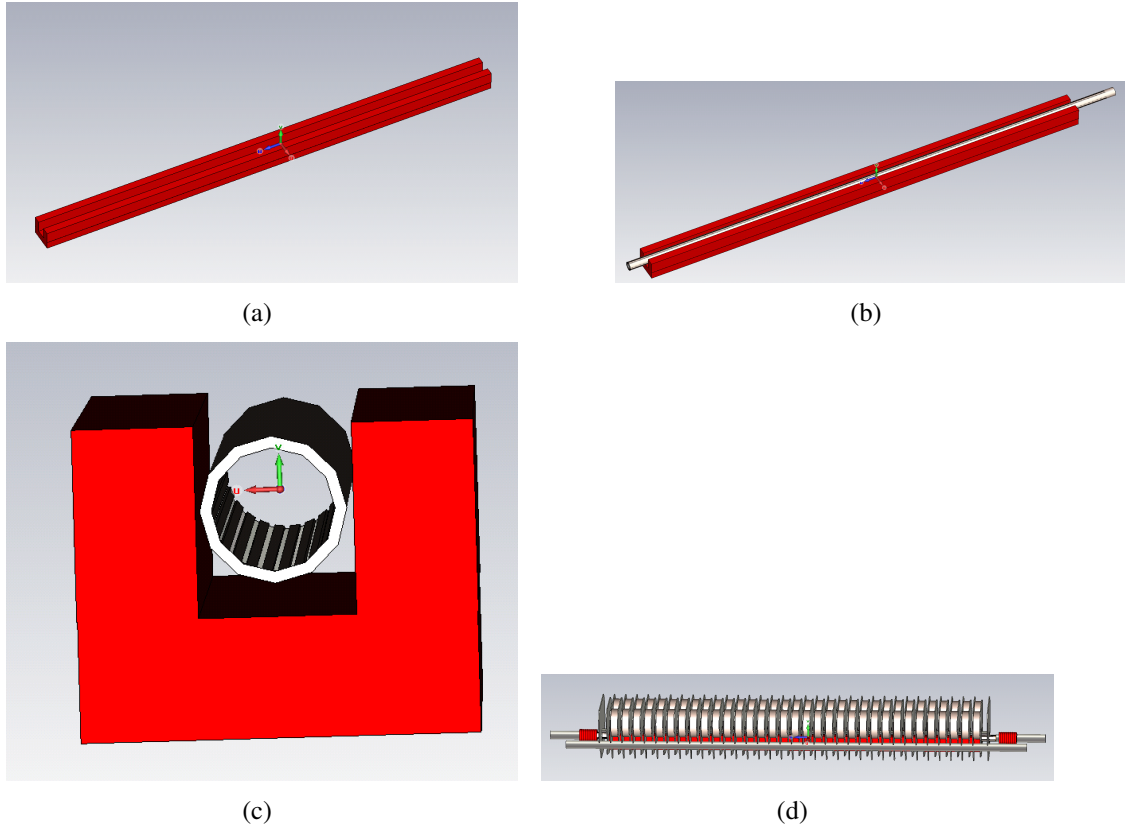
Figure 8.17: The geometries simulated for the various components in the LHC-MKI. These are ferrite only 8.17(a), ferrite and the ceramic beam screen 8.17(b), ferrite with the beam screen containing 24 screen conductors 8.17(c) and finally the complete MKI magnet 8.17(d).

with frequency due to the inductive component of the impedance) even with the presence of screen conductors.

Concerning the role of the beam screen layout there are two areas to examine - the effect of different quantities of screening of the beam by having more or less screen conductors (in this case removing those directed towards the HV busbar as is likely due to concerns of electrical breakdown) and of the effect of different dimensions of the screen at the capacitively coupled end of the beam screen.
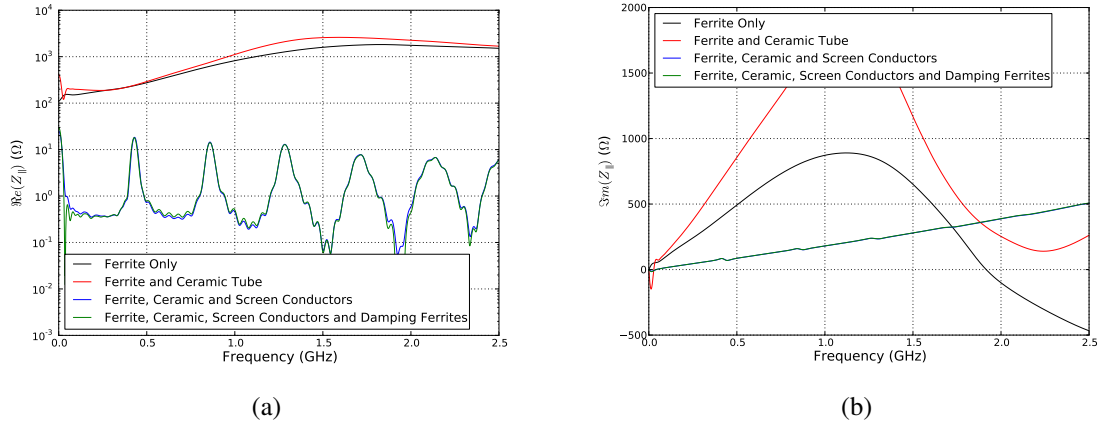
Figure 8.18: The 8.18(a) real component and the 8.18(b) imaginary components of the LHC MKI kicker magnet impedances for different quantities of components in the magnet.

8.5.2 How Screening Changes with the Number of Screen Conductors

For the changes on the number of screen conductors two variations are carried out - The first is to examine the case of removing several screen conductors in the beam screen towards the HV busbar (shown in Fig. 8.5.2). This direction is chosen as these screen conductors experience the highest induced voltage during the firing of the kicker magnet, and additionally it was initially thought that on this side the HV busbar would provide some screening of the beam from the ferrite yoke. The second variation is to remove a selection of screen conductors towards the HV busbar (shown in Fig. **??**), in this case to examine whether it is possible to acquire some shielding through using some screen conductors and benefitting from removing some screen conductors to remove the rate of electrical breakdown.

The longitudinal impedance for these configurations is shown in Fig. 8.5.2. It can be seen that for both components of the impedance that more screen conductors reduces the magnitude of the impedance at all frequencies - this can simply be understood as improving the screening of the beam from the ferrite with additional screen conductors. This can particularly be seen in the increase in the number of screen conductors from 15 to

152
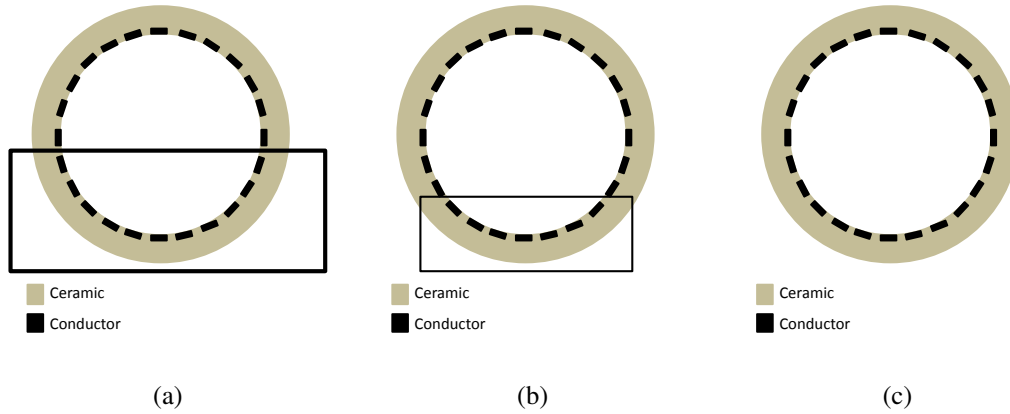
Figure 8.19: Beam screens with different numbers of screen conductors removed from the design quantity of 24. Models of 15 8.19(a), 19 8.19(b) and 24 8.19(c) screen conductors are considered for the impedance simulations. Conductors surrounded by the boxes are removed in this case.

19 to 24 conductors in total - The screening is improved dramatically in each subsequent case.

In addition it can be seen that it is preferable to distribute the screen conductors such that the maximum arc of the beam screen without screen conductors is minimised. This can clearly be seen by comparing the case of 19 screen conductors where all conductors are clustered together (as was done for the replacement MKI8d) and for 19 screen conductors, where 4 are equally distributed towards the HV busbar. Again this advantage is bourne out in the power lost in the structure. This is however not beneficial without consideration of the induced electric field during kicker firing, as the induced voltage on a given screen conductor is still the same, and thus tracking along the beam screen to the external metallization is not changed by this layout. It can thus be seen that the beam screen design itself must be optmised with regards to the induced screen conductor voltage before more can be added to the ceramic tube to improve screening.

8.5.3 Dependence of the Impedance on the Beam Screen Dimensions

It can be seen that with 24 screen conductors placed in the beam screen that the resulting impedance is dominated by the configuration of the beam screen. To investigate how changes to certain parameters (specifically the length of the overlap between the screen
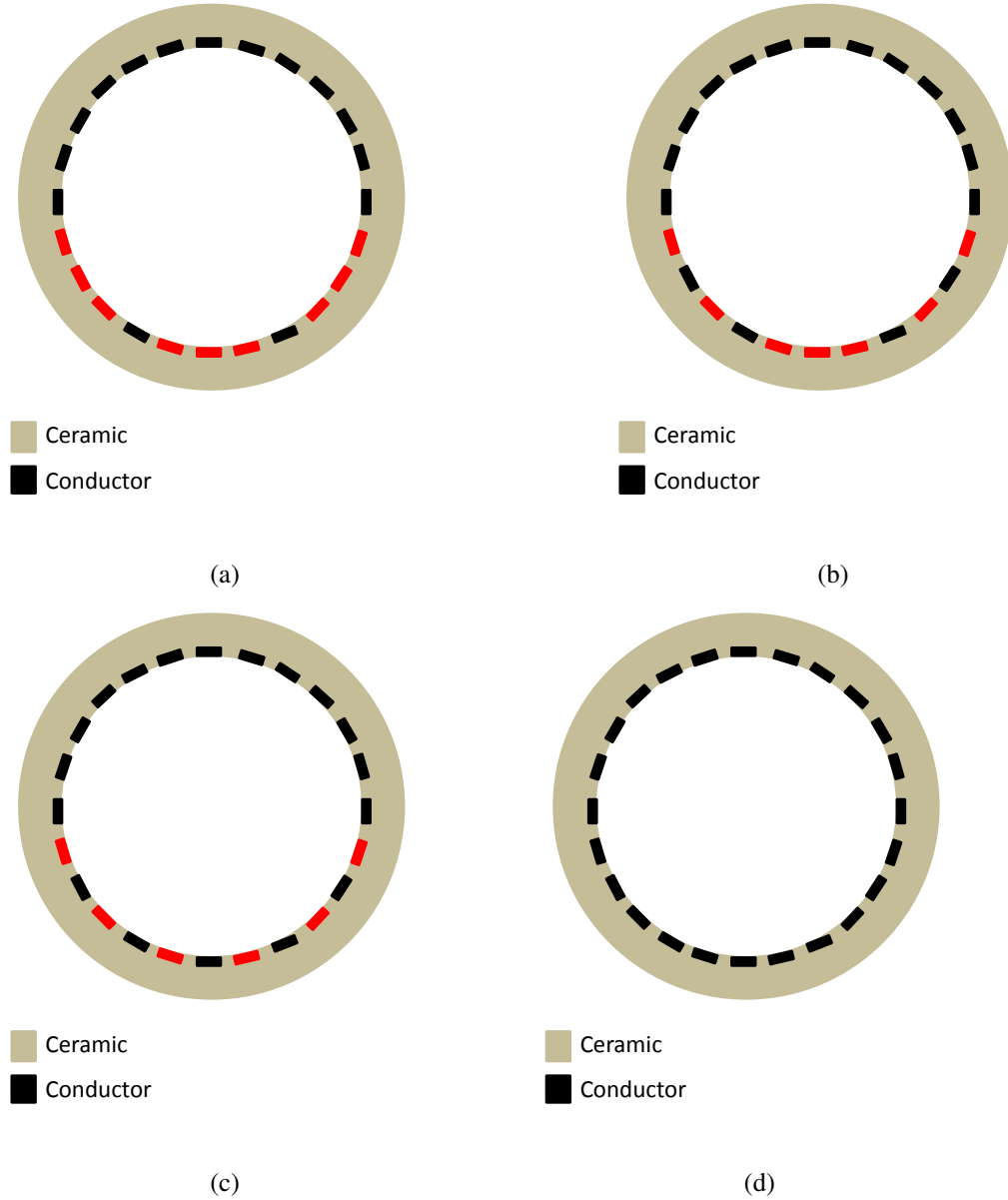
Figure 8.20: Beam screens with different numbers of screen conductors removed from the design quantity of 24. Models of 17 8.20(a), 19 8.20(b), 20 8.20(c) and 24 8.20(d) screen conductors are considered for the impedance simulations. Conductors that are coloured red are the removed in each case.

(a)   (b)
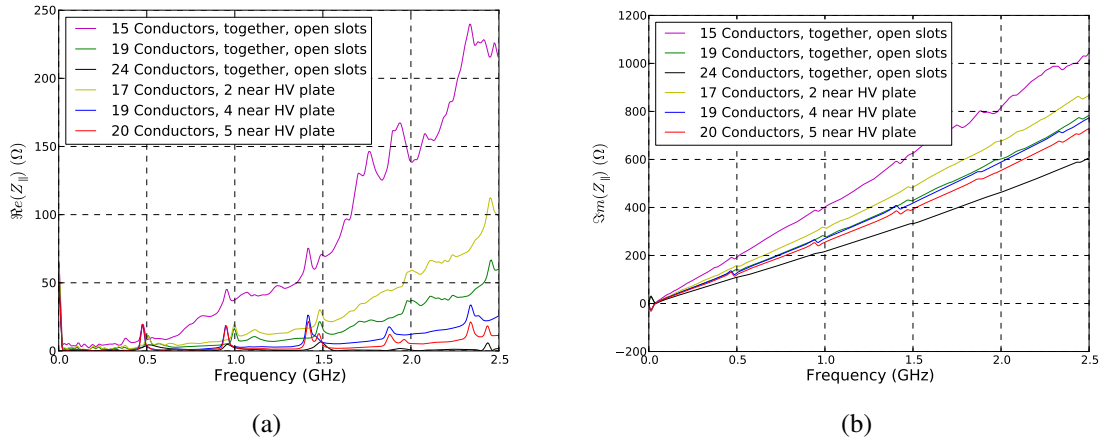
Figure 8.21: The longitudinal impedance of the MKIs with different numbers of screen conductors included in the beam screen. Shown is the real component 8.21(a) and the imaginary component 8.21(b) of the longitudinal impedance.

(a)(b)

Figure 8.22: 8.22(a) The cut down simulation model used for simulations of the MKI beam screen with 24 screen conductors and 8.22(b) an illustrated diagram of the capacitively coupled end of the beam screen.

conductors and the external metallization and the thickness of the ceramic beam screen) a cut down model of the kicker magnet is used, considering just the capactively coupled end of the kicker magnet (shown in Fig. 8.22(a)). This is done to allow a larger mesh density in this important (from the electrical and impedance point of view) region of the kicker magnet. In models of the full kicker magnet the mesh density is severely limited due to the large mesh generated in the entire magnet volume which subsequently may make the mesh very limited in near beam areas (for example in the ceramic tube between the screen conductors and the external metallization. A comparison is shown in Fig. 8.5.3). An illustrated diagram of the capacitively coupled end is given in Fig. 8.22(b) to clarify the components referred to in this section.

First we shall consider the effect the impedance of the change in the length of overlap of the capacitively coupled sections. To do this we consider the shortened end section, and change the length of the external metallization to change the length of the overlap (the length of the screen conductors used is keep fixed to avoid changing any potential

(a)(b)

Figure 8.23: A comparison of the mesh that may be generated in CST Particle Studio using both the full model 8.23(a) and the cutdown model 8.23(b). Blue squares reresent a meshing failure which inserts perfect electrical conductor into the model. The simulation time for the first is on the order a day, for the second 30 minutes.

resonances due to the screen conductors acting as $\lambda/4$ resonators). Overlaps of between 0.08m and 0.12m at 0.01m intervals are simulated, and the results shown in Fig. 8.24(a). It can be seen that each overlap has a distinct set of resonance frequencies. These source of these resonances can be seen to be the result of the gap between the external metalliza- tion and the screen conductor acting as a $n\lambda/2$ resonator. End effects caused the effective length of the overlap to be extended to some degree, which fitting to the resonance fre- quencies has shown to be ≈ 9mm for all lengths. This gives a resonant frequency f_{res} of

$$f_{res} = \frac{nc}{\sqrt{\epsilon_r}2L_{overlap}} \tag{8.1}$$

where n is an integer, c is the speed of light ϵ_r is the relative permitivitty of the volume material (= 10 for the alumina beam screen) and $L_{overlap}$ is the length of overlap. This can be seen for the first resonances for all the lengths of overlap in Fig. 8.24(b), and up to 2.5GHz for the case of the overlap being 100mm in Fig. 8.5.3. It can be seen that the predicted frequencies match the simulated very well. Work is still under way as to how to determine the peak impedance of each resonance.

Secondly the influence of the thickness of the beam screen is considered. This is a concern as increasing this thickness has two effects - to change the value of the capci- tance at the capacitively coupled end which effects the low frequency impedance, and the increase in the volume of the overlap region due to the increased thickness. The internal diameter of the ceramic tube is kept at 42mm, whilst external diameters of 50, 53 and 56mm are considered, giving tube thicknesses between 8 and 14mm. The resulting real component of the longitudinal impedances is shown in Fig. 8.5.3, where it can be seen that the increasing the pipe thickness has two effects - a slight lowering of the resonant

(a)   (b)
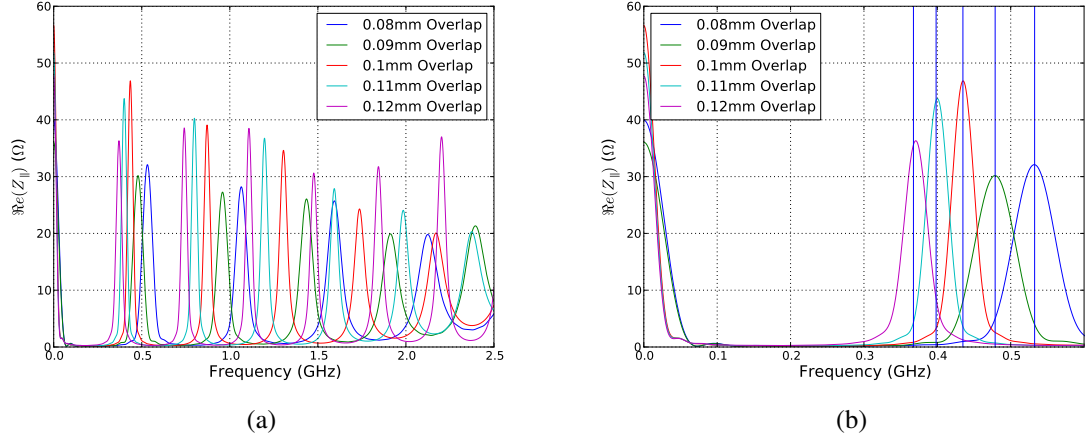
Figure 8.24: 8.24(a) The real component of the longitudinal beam coupling impedance for different lengths of the overlap, and **??** a zoomed in plot of the first resonances of all the overlaps with the calculated resonance frequency for each
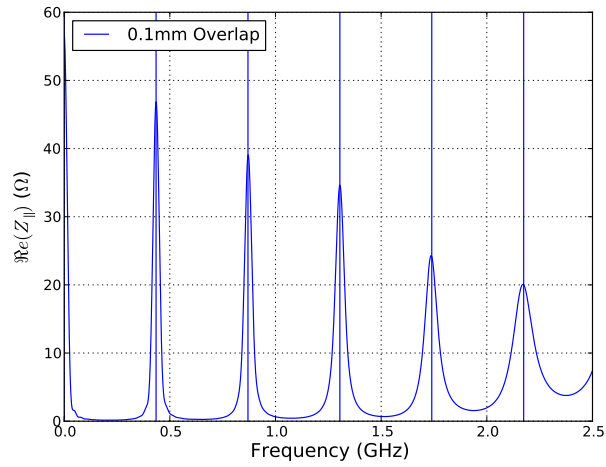
Figure 8.25: The impedance of the beam screen with 24 screen conductors with an overlap $L_{overlap} = 100mm$ and the predicted resonance frequencies from Eqn. **??** shown as blue lines.
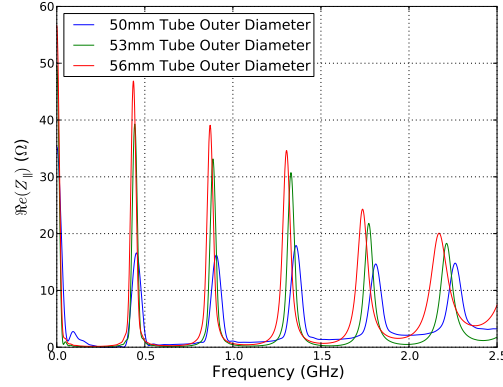
Figure 8.26: The variance of the real beam coupling impedance with the tube thickness. External diameters of 50, 53 and 56mm correspond to tube thicknesses of 8, 11 and 14mm respectively.

Table 8.5: The beam induced heating calculated for a number of beam screen designs with 24 screen conductors of equal length (overlap of 100mm) with different tube thicknesses assuming 50ns bunch spacing LHC conditions (1380 bunches, 1.7×10^{11}ppb with a bunch length of 1ns). It can be seen that the broadband heating component is relatively small for the limited change in the tube thickness, whilst the resonant component can increase drastically due to the increasing peak impedance.

Outer Tube Diameter/Tube Thickness (mm)	$P_{loss,BB}$	$P_{loss,Res}$
50/8	30	4
53/11	26	10
56/14	35	12

frequency, but also a significant increase of the peak impedance of the resonance, by almost a factor 2 from a tube 8mm thick to one 14mm thick. The difference that this makes to the expected heating of the MKI can be seen in Tab. 8.5.3, where it can be seen that the change in the power loss due to the increased thickness could be expected to be small assuming a broadband heating scenario, but increases significantly if we assume a beam harmonic falls upon the resonant frequency.

8.6 New Beam Screen Designs

Using the knowledge acquired from examining the beam coupling impedance dependence on the layout of the beam screen from the previous section, and additionally the electrical field simulations of the induced voltages on the screen conductors during magnet firing and number of alternative beam screen designs have been proposed. The driving points in these designs has been to reduce the power loss into the MKI (in this case to reduce the temperatures reached by the ferrite yoke) and to reduce the induced voltage in the screen conductors during magnet firing to eliminate electrical breakdown/discharge between the screen conductors and along the end the surface of the beam screen to a ground plane.

The proposed designs are described below:

- 24 screen conductors of alternating length, as shown in Fig. 8.6. The alternating length screen conductors layout has been demonstrated to reduce the induced voltage on the shorter length screen conductors, thus being beneficial to the electrical breakdown rate.

- 24 screen conductors tapered in length, as shown in Fig. 8.6. The tapering of the screen conductors has previously been shown to help reduce the induced potential in designs with 15 screen conductors, and should be kept as a proven, if not optimal option for 24 screen conductors.

- 24 screen conductors some with an alternating length and then tapered towards the HV busbar, as shown in Fig. 8.6. This intended to use the reduction of induced voltage due to the tapering, whilst keeping a relatively high capacitance at the capacitively coupled end so as to not induce additional worse resonances here.

- 24 screen conductors in enclosed slots in the ceramic beam screen, as shown in Fig. 8.6. The intention of this design is to increase the necessary induced voltage on the screen conductors before breakdown occurs due to surface tracking no longer being a possible breakdown path.

- An alternative screen conductor layout, in which some are conductively connected to ground on both ends and all other capacitively coupled, as shown in Fig. 8.6. This design is intended to reduce the induced voltage on the screen conductors by having all the screen conductors be connected to one another at the capacitively coupled end thus receiving the same induced voltage. To counter possible eddy currents during firing reducing the field rise time the majority of the screen conductors are capacitively coupled at both ends of the magnet, with two conductors conencted to ground at the downstream end of the magnet.

- 24 screen conductors with part of the metallization replaced by a external metal cylinder, as shown in Fig. 8.6. This design is intended to reduce the electric field gradients at the capacitively coupled end by removing the distance between the screen conductors and the ground plane by replacing the metallization on the external surface of the ceramic beam screen with a metal cylinder some millimetres off the surface. Electric field simulations had shown that the high permittivity of the ceramic was in effect pushing the ground plane into the ceramic cylinder, reducing the effective spacing between the screen conductors and the metallization, whereas this physical air gap should reduce this effect.

- 24 screen conductors of a mixture of alternating and tapered lengths with part of the metallization replaced with an external metal cylinder, as shown in Fig. 8.6. This was intended to improve on the above design by using the combined alternating and tapered design to further reduce the induced voltages on the screen conductors. Due to difficulty of manufacturing the step out of the beam screen is continued beyond the ends of the screen conductors. **This is the proposed final design for implementation in the replacement MKIs for installation during long shutdown 1**.

In this analysis we shall focus on the resulting power loss from interaction of the beam with the real component of the longitudinal beam impedance as this is the present primary limitation from the MKIs. The real component of the longitudinal beam coupling impedance is shown in Fig. 8.34(a) along with comparisons to the existing MKIs in the

160
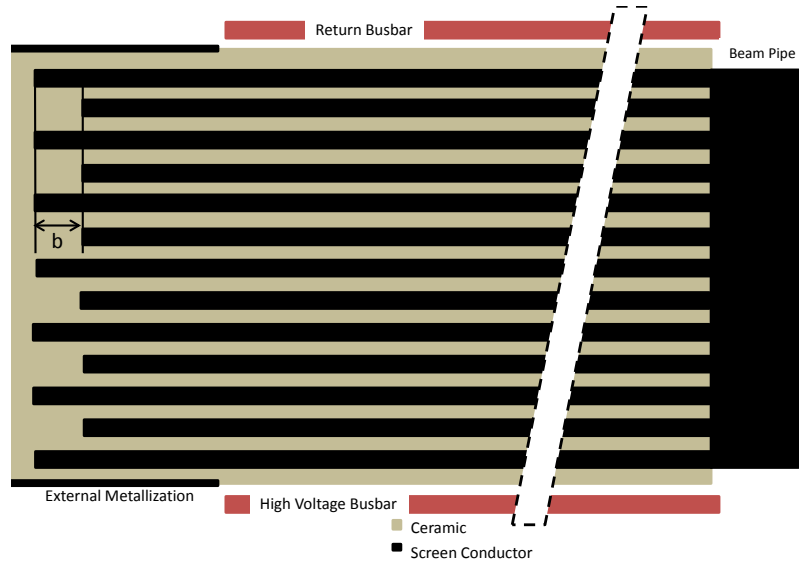
Figure 8.27: A MKI beam screen design with alternating lengths of screen conductors - seperated by a length b.
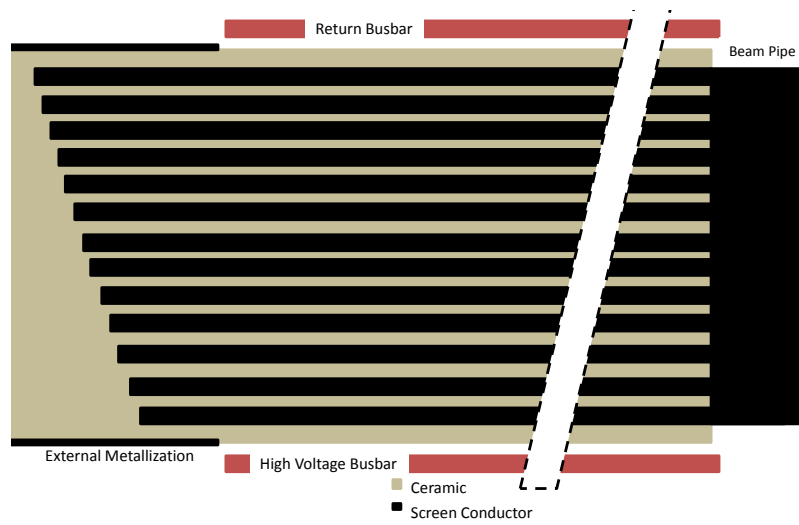
Figure 8.28: A MKI beam screen design with tapered lengths of screen conductors. The taper may be altered to acquire the desired combination of impedance and induced voltage on the screen conductors.
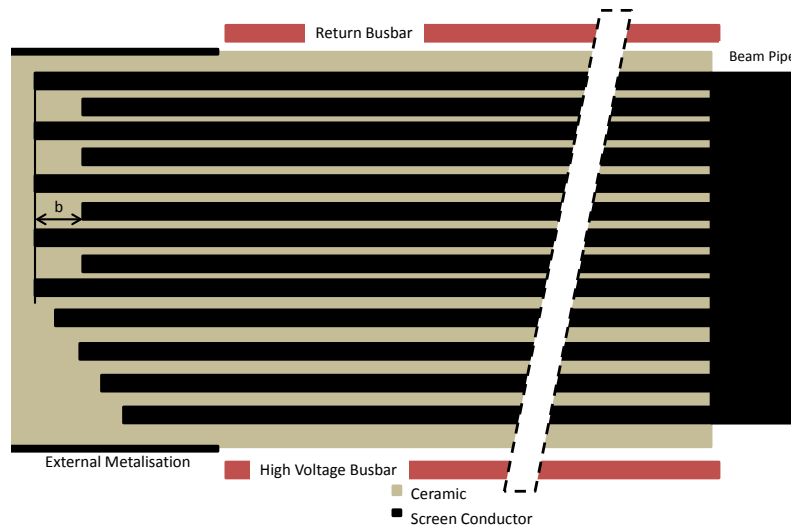
Figure 8.29: A MKI beam screen design with a combination of tapered and alternating screen conductors. The degree of alternating and tapering may change dependent of the desired impedance and induced voltage on the screen conductors.
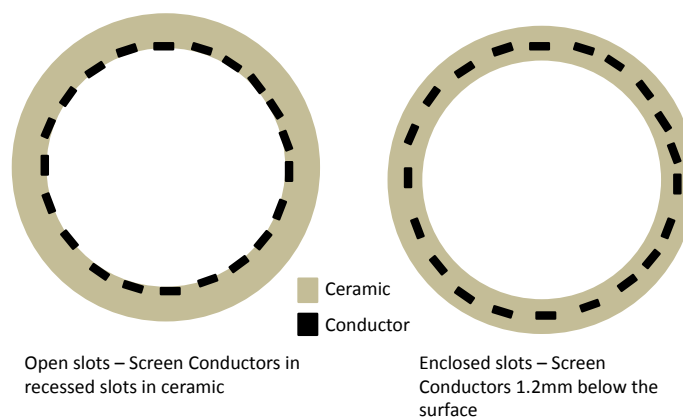
Figure 8.30: A MKI beam screen design with enclosed slots (shown in comparison to the usual beam screen design with open slots) for the screen conductors.
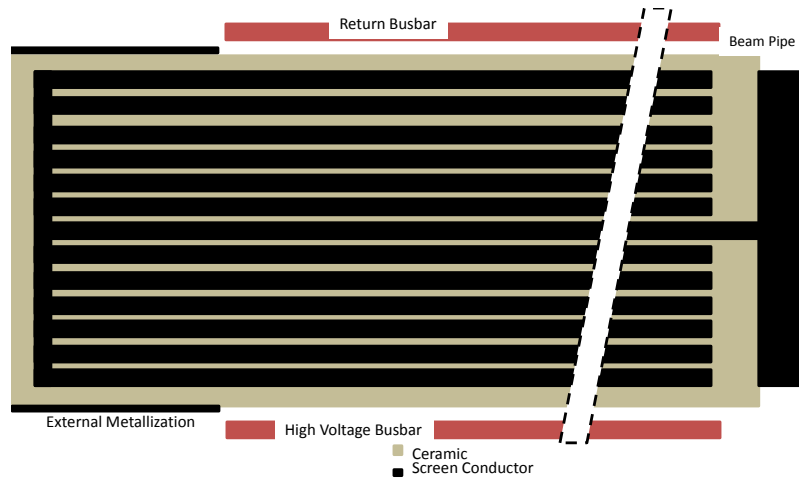
Figure 8.31: A MKI beam screen design using an alternative screen conductor layout in which 2 (cross section shown here) conductors are connected to ground at the downstream end of the screen, and all conductors are welded together are the capacitiviely coupled end.
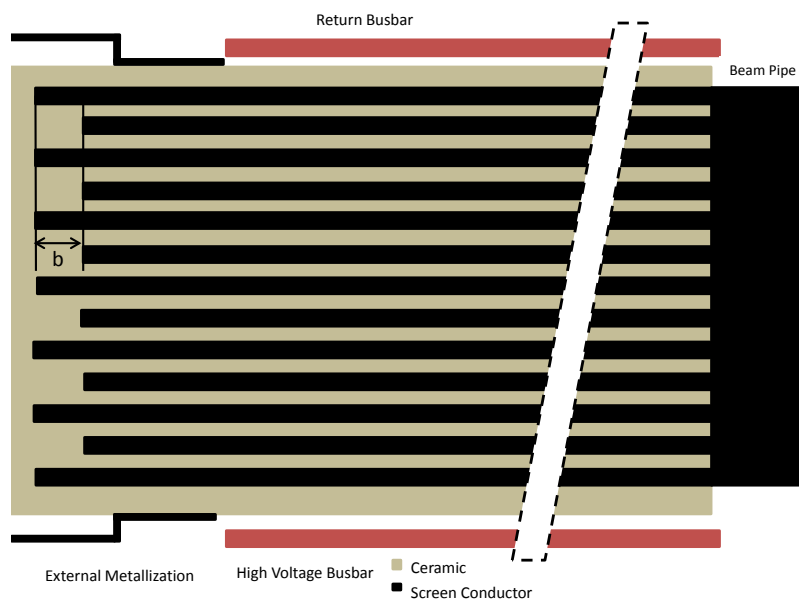
Figure 8.32: A MKI beam screen design implementing a replacement of some of the external metallization with a metallic cylinder so as to pull the ground plane closest to the screen conductors away.
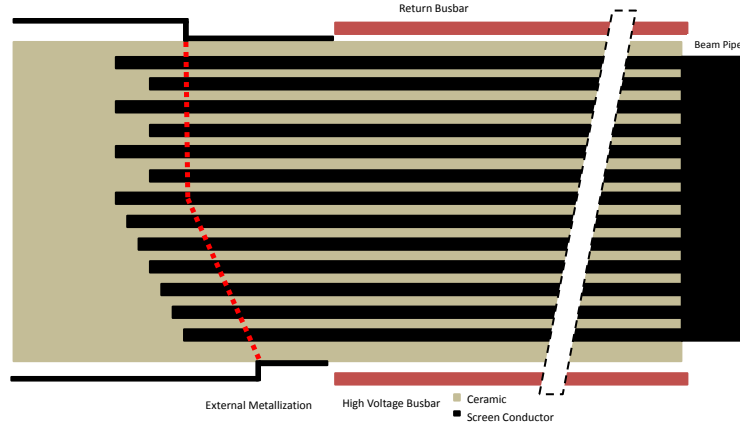
Figure 8.33: The proposed final MKI design. A combination of alternating and tapered screeb conductors is used, along with a step out of the external metallization. The outline of the step out is shown by the red-dashed line.

LHC with 15 and 19 screen conductors. A restricted selection of the results (combination layout from Fig. 8.6, the alternative design from Fig. 8.6 and the final design Fig. 8.6) logarithmic (i the y-axis) plot is shown in Fig. 8.34(b) for further clarity.

The estimated heating for both 25ns and 50ns bunch spacing operation in the LHC are shown in Tab. 8.6 for 1ns bunch length, and the variation in power loss with the bunch length for 25ns and 50ns bunch spacing shown in Fig. 8.6. It can be seen that the power loss can be very strongly reduced for very short bunch lengths (as has been proposed for HL-LHC operation without crab cavities [cite]) by increasing the bunch length, but for nominal bunch lengths (τ_b =1ns) it can be seen that there is not much benefit in increasing the bunch length.

8.7 Upgrade Plans for Long Shutdown 1 and Beyond

During long shutdown 1 (LS1) it has been decided to first carry out measurements of the beam impedance and electrical breakdowns observed of the proposed new beam screen design, and subsequently construct 8 new kicker magets implementing the new screen design and the additional proposed changes to the inside of the vacuum tank to reduce
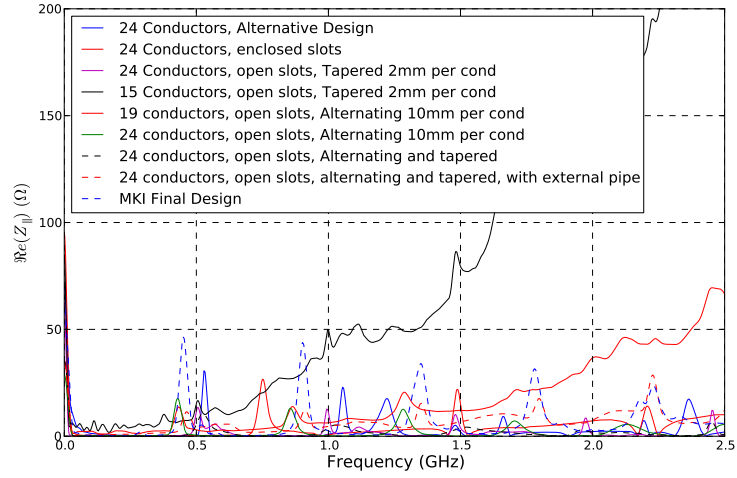
(a)
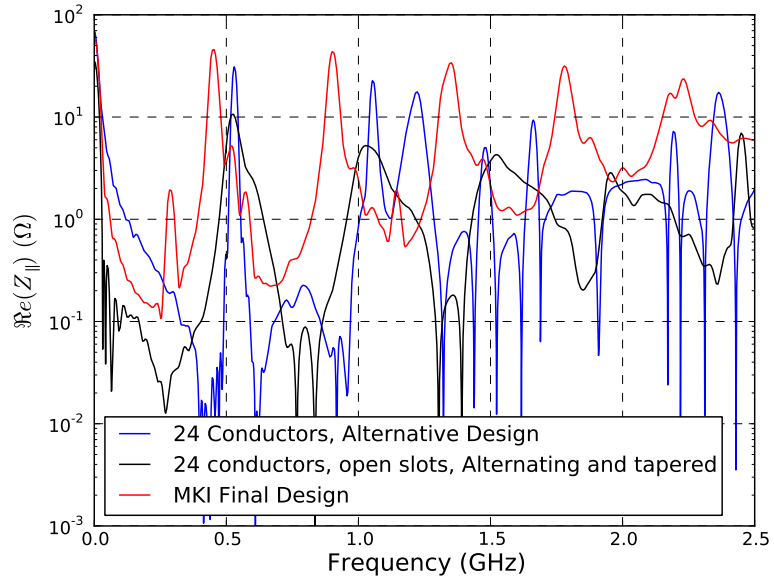
(b)

Figure 8.34: The real component of the beam coupling impedance for a number of the proposed beam screen designs compared to the existing designs (15 screen conductors tapered and 19 screen conductors alternating in length) 8.34(a). A selected collection of favourable (from the impedance and the electric field point of view) are shown in 8.34(b) with a log scale on the Y axis so the resonance structure can be more clearly seen.

Table 8.6: The power loss expected due to beam-wakefield interactions in the MKIs for a number of proposed beam screen designs. Estimates are given for 50ns and 25ns bunch spacing in the LHC (1380 bunches, 1.7×10^{11} particles per bunch for 50ns, 2808 bunches, 1.15×10^{11} particles per bunch for 25ns) assuming a $\cos^2$ bunch distribution.

Screen Design	$P_{loss,50ns}$ (W), $t_b = 1$ns	$P_{loss,25ns}$ (W), $t_b = 1$ns
24 Conductors, Alternating Length	36	28
24 Conductors, Tapered Length	$P_{loss,50ns}$ (W), $t_b = 1$ns	$P_{loss,25ns}$ (W), $t_b = 1$ns
24 Conductors, Alternating and Tapered	$P_{loss,50ns}$ (W), $t_b = 1$ns	$P_{loss,25ns}$ (W), $t_b = 1$ns
24 Screen Conductors, Enclosed Conductors	$P_{loss,50ns}$ (W), $t_b = 1$ns	$P_{loss,25ns}$ (W), $t_b = 1$ns
24 Conductors, Alternate Design	$P_{loss,50ns}$ (W), $t_b = 1$ns	$P_{loss,25ns}$ (W), $t_b = 1$ns
24 Conductors, Step out	37	28
24 Conductors, Final Design	37	28
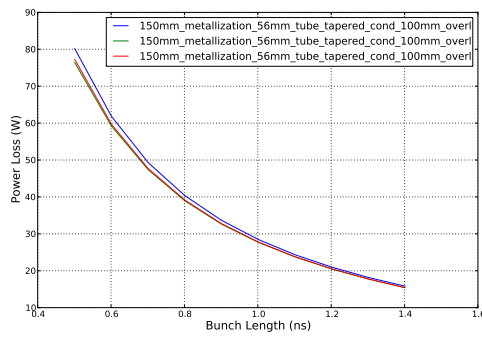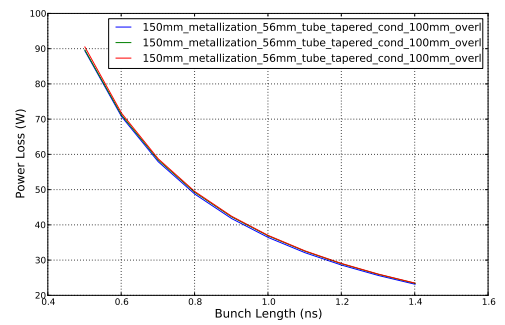
Figure 8.35: The variation of the predicted beam induced power loss with bunch length for a number of screen designs. The variation for 25ns 8.35(a) and 50ns 8.35(b) machine settings.

Figure 8.36: The maximum steady-state temperature reached by the ferrite yoke in the MKI depending on the power load on the ferrite yoke as calculated using a 2D cross section of the MKI. Provided by M. Garlasche et al [cite].

the temperatures reached in the ferrite yoke. Thermal simulations have indicated that the proposed screen designs will be capable of reducing the maximum temperature reached in the ferrite yoke below the curie temperature for the nominal operating conditions for the LHC, and for a number of proposed HL-LHC operating conditions also (see Fig. 8.7). In addition electric field simulations have strongly indicated that the induced electric potential on the screen conductors will not be sufficient to induce electrical breakdowns beyond an unsafe operating point.

Further monitoring of the MKIs will be necessary as the stored current in the LHC is increased due to possible further sources of heating within the magnets, however with the work done on the understanding of the beam impedance, the heat transfer within the magnet and the electric field during kicker firing has greatly improved the knowledge of possible limitations in the future and the variety of solutions/counter measures that may be taken.

Chapter 9

Conclusions

In this thesis has been presented a number of studies into the impedance reduction techniques employed in two key systems in LHC, the injection kicker magnets and the collimation systems. Problems with these existing methods have been examined, focusing on their shortcomings from an operational standpoint especially the high temperatures experienced due to beam-induced heating, using both computational and bench-top measurements to identify and charcterise the beam-coupling impedance responsible for this. As part of this a new method for measuring the transverse beam impedances of asymmetric structures has been proposed and verified using experimental and computational measurements against both an analytical model and a measured structure. In addition a study of the power loss in ferrite damped cavities with different extents of damping and screening of the ferrite has been presented in order to better understand the heat loads in structures with a complex structure which may limit the effective damping of cavity modes by ferrite.

Subsequently improvements to the existing systems have been proposed, with a certain focus on the expected power load due to beam-induced heating, resulting in a new RF damping system for use in the TCTP collimators, and possibly for further use in the phase 2 secondary collimators and an improved beam screen for use in the LHC injection kicker magnets to be constructed and installed during LS1 in 2013/14.

It has become clear during this work that with the increasing high beamcurrents demanded at high energy hadron colliders in addition to the very long fill times that beam-induced heating must seriously be considered as a potential limitation on the integrated luminosity delivered to the experiments due to both high temperatures that may damage equipment, or due to long cool down times necessary between uses. As such knowledge of the existing impedance reduction techniques must be propogated to the accelerator community, and the suitability and correct implementation of them studied thoroghly during the *design* phase of equipment design can not be emphasised enough.

Bibliography

Appendix A

TCTP Eigenmode Simulations - No Ferrite

1.023	500	0.00052	0.3
1.053	725	0.00419	3.0
1.070	609	0.00040	0.2
1.119	462	0.02717	12.6
1.127	658	0.00006	0.0
1.161	432	0.00291	1.3
1.181	436	0.00251	1.1
1.187	1070	0.00422	4.5
1.195	509	0.01165	5.9
1.235	377	0.01146	4.3
1.207	453	0.45465	205.8
1.268	500	0.00201	1.0
1.280	404	0.01590	6.4
1.282	717	0.02778	19.9
1.291	551	0.13380	73.7
1.300	568	0.27971	158.9

f (GHz)	Q	R/Q (Ω)	R_s (Ω)
1.304	434	0.26437	114.7
0.131	233	0.00017	0.0
1.313	390	0.19889	77.5
1.322	297	0.00566	1.7
1.325	282	0.00026	0.1
1.331	602	0.10319	62.1
1.341	188	0.00001	0.0
1.342	197	0.03311	6.5
1.346	111	0.00026	0.0
1.357	421	0.01681	7.1
1.363	516	0.51441	265.5
1.365	514	0.34623	178.1
1.378	772	0.00637	4.9
1.392	519	0.09893	51.4
1.396	553	0.00465	2.6
1.417	696	0.07621	53.0
1.424	679	0.06070	41.2
1.429	521	0.02521	13.1
1.445	567	0.00123	0.7
1.454	926	0.00029	0.3
1.459	572	0.00005	0.0
1.464	990	0.00001	0.0
1.476	1052	0.00006	0.1
1.479	1097	0.00002	0.0
1.487	669	0.00790	5.3
1.495	627	0.01068	6.7
1.504	647	0.00006	0.0

f (GHz)	Q	R/Q (Ω)	R_s (Ω)
1.522	597	0.00917	5.5
1.524	852	0.00020	0.2
1.554	535	0.00107	0.6
1.556	909	0.00044	0.4
1.559	931	0.00044	0.4
1.580	795	0.01642	13.0
1.587	909	0.00133	1.2
1.589	929	0.00101	0.9
1.607	716	0.00000	0.0
1.609	610	0.00448	2.7
1.612	747	0.00000	0.0
1.615	827	0.00062	0.5
1.624	646	0.00004	0.0
1.632	844	0.00000	0.0
1.636	914	0.00016	0.1
1.643	449	0.00006	0.0
1.649	845	0.00012	0.1
1.653	617	0.00347	2.1
1.680	928	0.00110	1.0
1.683	762	0.00027	0.2
1.690	593	0.00321	1.9
1.698	768	0.00002	0.0
1.709	1058	0.00000	0.0
1.711	1046	0.00810	8.5
1.716	829	0.00002	0.0
1.722	997	0.00000	0.0
1.732	953	0.00001	0.0

f (GHz)	Q	R/Q (Ω)	R_s (Ω)
1.734	760	0.00002	0.0
1.743	894	0.00018	0.2
1.744	860	0.00092	0.8
1.748	882	0.00062	0.5
1.759	773	0.00007	0.1
1.767	723	0.00021	0.2
1.780	802	0.00226	1.8
1.785	858	0.00094	0.8
1.789	942	0.00034	0.3
1.795	646	0.00301	1.9
1.800	719	0.00030	0.2
1.801	985	0.00109	1.1
1.816	670	0.00013	0.1
1.825	924	0.00019	0.2
1.829	650	0.00001	0.0
1.832	1061	0.00005	0.1
1.837	351	0.00071	0.2
1.842	367	0.00044	0.2
1.858	641	0.00249	1.6
1.869	961	0.00063	0.6
1.882	1202	0.00046	0.5
1.883	396	0.00121	0.5
1.888	857	0.00371	3.2
1.895	1100	0.00050	0.6
1.897	688	0.00570	3.9
1.903	1039	0.00007	0.1
1.910	710	0.00000	0.0

f (GHz)	Q	R/Q (Ω)	R_s (Ω)
1.920	968	0.00000	0.0
1.930	219	0.05093	11.2
1.932	189	0.09952	18.8
1.944	588	0.03731	21.9
1.948	1048	0.00053	0.6
1.952	1027	0.01573	16.2
1.959	597	0.00651	3.9
1.966	643	0.04869	31.3
1.974	724	0.00005	0.0
1.993	627	0.00039	0.2
0.200	162	0.00090	0.1
0.260	333	0.00051	0.2
0.305	250	0.00152	0.4
0.315	312	0.00002	0.0
0.383	542	0.00091	0.5
0.388	399	0.00088	0.4
0.425	214	0.00152	0.3
0.484	488	0.00308	1.5
0.514	461	0.00199	0.9
0.514	452	0.00188	0.8
0.532	232	0.00192	0.4
0.586	444	0.00004	0.0
0.614	424	0.04269	18.1
0.633	213	0.00168	0.4
0.636	249	0.00180	0.4
0.641	453	0.11620	52.7
0.665	411	0.06443	26.5

f (GHz)	Q	R/Q (Ω)	R_s (Ω)
0.715	357	0.14033	50.1
0.716	362	0.14259	51.7
0.726	292	0.03288	9.6
0.750	365	0.01933	7.1
0.753	515	0.00803	4.1
0.781	344	0.10722	36.9
0.824	661	0.00063	0.4
0.826	306	0.00198	0.6
0.829	665	0.00061	0.4
0.851	342	0.04860	16.6
0.859	478	0.04383	20.9
0.863	628	0.00014	0.1
0.874	433	0.00005	0.0
0.902	509	0.00124	0.6
0.930	406	0.00161	0.7
0.941	460	0.22196	102.1
0.945	318	0.00803	2.6
0.962	536	0.00003	0.0
0.983	360	0.02222	8.0

Appendix B

TCTP Eigenmode Simulations - With Ferrite

f (GHz)	Q	R/Q (Ω)	R_s (Ω)
1.008	7	0.14378	1.0
1.019	78	0.19377	15.2
1.027	100	0.07519	7.5
1.042	21	0.04155	0.9
1.052	306	0.00385	1.2
1.071	116	0.00176	0.2
1.074	111	0.00204	0.2
1.075	147	0.00742	1.1
1.085	92	0.03424	3.1
1.126	215	0.00021	0.0
1.133	31	0.03086	1.0
1.142	60	0.22597	13.5
1.175	67	0.00764	0.5
1.216	31	0.76573	23.6
1.227	62	0.04137	2.6

f (GHz)	Q	R/Q (Ω)	R_s (Ω)
1.240	188	0.15624	29.4
0.130	80	0.00003	0.0
1.300	126	0.23688	29.9
1.314	168	0.00333	0.6
1.371	78	0.47218	36.8
1.404	157	0.04230	6.6
1.476	33	0.00084	0.0
1.501	76	0.00781	0.6
1.507	92	0.00004	0.0
1.545	49	0.00978	0.5
1.550	105	0.01460	1.5
1.578	32	0.00014	0.0
1.613	37	0.00006	0.0
1.636	13	0.00539	0.1
1.675	65	0.00010	0.0
1.679	64	0.00006	0.0
1.715	160	0.00133	0.2
1.723	206	0.00028	0.1
1.734	116	0.00010	0.0
1.770	83	0.00143	0.1
1.782	137	0.00064	0.1
1.792	113	0.00103	0.1
1.796	110	0.00103	0.1
1.806	33	0.00003	0.0
1.840	69	0.00051	0.0
1.844	16	0.00665	0.1
1.862	51	0.00057	0.0

f (GHz)	Q	R/Q (Ω)	R_s (Ω)
1.895	113	0.00397	0.5
1.919	41	0.00341	0.1
1.926	164	0.04103	6.7
1.933	75	0.00397	0.3
1.937	123	0.00103	0.1
1.969	36	0.00131	0.0
1.973	35	0.00130	0.0
2.006	59	0.00241	0.1
0.227	1	0.00377	0.0
0.241	1	0.01920	0.0
0.251	1	0.00910	0.0
0.295	18	0.00354	0.1
0.320	11	0.00180	0.0
0.388	56	0.00293	0.2
0.405	2	0.12558	0.3
0.409	41	0.00228	0.1
0.416	1	0.11308	0.1
0.493	12	0.00335	0.0
0.504	4	0.19510	0.8
0.512	50	0.00053	0.0
0.512	50	0.00044	0.0
0.515	138	0.00727	1.0
0.547	2	0.06283	0.1
0.585	5	0.41263	2.1
0.589	5	0.45154	2.1
0.606	39	0.00195	0.1
0.625	18	0.09450	1.7

f (GHz)	Q	R/Q (Ω)	R_s (Ω)
0.636	223	0.01395	3.1
0.653	5	0.41565	2.1
0.657	2	0.12553	0.2
0.703	42	0.00036	0.0
0.750	29	0.01932	0.6
0.752	140	0.02023	2.8
0.761	5	0.38464	1.9
0.842	113	0.00376	0.4
0.855	90	0.06217	5.6
0.864	6	0.32443	1.9
0.889	2	0.14481	0.4
0.901	50	0.00105	0.1
0.924	83	0.00009	0.0
0.938	61	0.25099	15.4
0.959	14	0.13559	1.9